SULFUR PASSIVATION OF III-V SEMICONDUCTOR NANOWIRES

SULFUR PASSIVATION OF III-V SEMICONDUCTOR NANOWIRES

By

NOOSHIN TAJIK, B.Sc., M.Sc.

A Thesis

Submitted to the School of Graduate Studies

in Partial Fulfilment of the Requirements

for the Degree

Doctor of Philosophy

McMaster University

DOCTOR OF PHILOSOPHY (2013)   McMaster University

(Department of Engineering Physics)   Hamilton, Ontario

TITLE: Sulfur Passivation of III-V Semiconductor
              Nanowires

AUTHOR: Nooshin Tajik, B.Sc. (Sharif University of

              Technology), M.Sc. (Beheshti University)

SUPERVISOR: Dr. Ray R. LaPierre

NUMBER OF PAGES: xx, 132

Abstract

An ammonium polysulfide $(NH_4)_2S_x$ solution was optimized through a series of experiments to be used for surface passivation of III-V nanowires (NWs). The effectiveness of sulfur passivation was investigated by measuring the photoluminescence (PL) from p-InP NWs before and after passivation. The optimized parameters included solvent type, molarity and passivation time. According to the experiments, passivation of NWs in 0.5 M solution diluted in isopropyl alcohol (IPA) for 5 min produced the maximum PL improvement. It was also demonstrated that the whole surface passivation of vertical NWs in ensemble samples caused a 40 times increase in the PL intensity while top surface passivation of individual NWs resulted in a 20 times increase of PL intensity. A model was developed to calculate the PL from single NWs under different surface recombination and surface potential. The model showed that the 40 times increase in the PL is mainly due to the reduction of surface state density from 10^{12} cm^{-2} before passivation to 5×10^{10} cm^{-2} after passivation. The effect of passivation was also investigated from the excitation intensity dependence of the PL. Before passivation a blue shift of around 32 meV was observed on the PL peak position by increasing the excitation intensity, but after passivation no blue shift was observed. This change was attributed to the reduction of surface potential after passivation. The PL intensity from passivated NWs decreased to its initial (pre-

passivation) value over a period of 7 days in ambient air, indicating that the sulfur passivation was unstable in atmosphere.

The I-V characteristics of ensemble n-GaAs NWs were measured before passivation (BP), after contact passivation (ACP) and after whole surface passivation (AWP) of NWs. An increase in the current through the ensemble NWs was observed after both ACP and AWP. Using a metal-semiconductor model, it was shown that the change in the Schottky barrier height of the top contact and resistivity of the NW due to the change in the effective radius of NW after passivation, can explain the current enhancement. For ensemble NWs, the back contact was considered to be mainly affected by n-n+ junction formation between the NWs and substrate, while the top contact was kept as a Schottky barrier. The model showed a reduction of 0.2-0.3 eV for the Schottky barrier of the top contact and an increase of a few nanometers in the radius of NWs.

The effect of sulfur passivation on core-shell p-n junction GaAs NW solar cells has been investigated. Two types of device were investigated consisting of indium tin oxide contact dots or opaque Au finger electrodes. Lateral carrier transport from the NWs to the contact fingers was achieved via a p-doped GaAs surface conduction layer. NWs between the opaque contact fingers had sidewall surfaces exposed for passivation by sulfur. The relative cell efficiency increased by 19% after passivation. The contribution of the thin film grown between NWs to the total cell efficiency was estimated by removing the NWs using a sonication

procedure. Mechanisms of carrier transport and photovoltaic effects are discussed

based on spatially resolved laser scanning measurements.

Preface

The work presented in this thesis has been previously published in three refereed journal articles:

I) N. Tajik, Z. Peng, P. Kuyanov, and R. R. LaPierre, Nanotechnology **22**, 225402 (2011)

II) N. Tajik, C. M. Haapamaki, and R. R. LaPierre, Nanotechnology **23**, 315703 (2012)

III) N. Tajik, A. C. E. Chia, and R. R. LaPierre, Appl. Phys. Lett. **100**, 203122 (2012)

Acknowledgments

Here I want to extend my gratitude to all who assisted me in completion of this research work. Without their valuable contributions, this dissertation would not have been possible.

I devote the first and greatest regards to my supervisor, Dr. Ray LaPierre, for all his economic, scientific and psychic supports during these years. His patience and guidance enabled me to investigate some parts of the interesting world of nanowires and made this thesis possible.

I am highly indebted to my supervisory committee members, Dr. Adrian Kitai and Dr. Rafael Kleiman, for their valuable feedbacks and inspiring ideas.

It is also a great honor for me to thank:

- ❖ Dr. Brad Robinson and Dr. Shahram Tavakoli, for their help in growing all the NW samples and helpful scientific discussions.
- ❖ Dr. Harald Stover who generously allowed me to prepare my solutions in his Lab.
- ❖ Doris Stevanovic and Dr. Zhilin Peng, for their endurance during the training sessions and all along after that. Their great experiences were indeed remedial in dead ends.
- ❖ Dr. Jacek Wojcik for his great technical supports in TAB Lab.
- ❖ Peter Jonassan for saving my laptop's life many times during these years.

"Never mistake knowledge for wisdom. One helps you make a living; the other helps you make a life."

Sandra Carey

Table of Contents

List of Figures

List of Tables

List of Acronyms

1-D	One Dimensional
2-D	Two Dimensional
μ-PL	Micro-Photoluminescence
AES	Auger Electron Spectroscopy
AP	After Passivation
ACP	After Contact Passivation
AWP	After Whole Passivation
BP	Before Passivation
BSE	Back Scattered Electrons
CCD	Charge-Coupled Device
CW	Continuous Wave
DI	Di-Ionized
EBL	Electron Beam Lithography
ET	Everhart Thornley
FET	Field Effect Transistor
FS	Femto Second
FTIR	Fourier Transform Infrared
GS-MBE	Gas-Source Molecular Beam Epitaxy
HF	Hydrofloric Acid
ICP	Inductively Coupled Plasma
IPA	Isopropyl Alcohol

ITO   Indium-Tin-Oxide

LED   Light-Emitting-Diode

LPE   Liquid Phase Epitaxy

MOCVD   Metal Organic Chemical Vapor Deposition

MOS   Metal-Oxide-Semiconductor

MS   Metal-Semiconductor

MSM   Metal-Semiconductor-Metal

NA   Numerical Aperture

NW   Nanowire

ND   Neutral Density

PE   Primary Electron

PES   Photoemission Spectroscopy

PL   Photoluminescence

PV   Photovoltaic

PVD   Physical Vapor Deposition

RIE   Reactive Ion Etching

RTA   Rapid Thermal Annealing

SAS   Self-Assembled Superlattices

SE   Secondary Electron

SEM   Scanning Electron Microscopy

SRH   Shockley-Read-Hall

SR-PES   Synchrotron Radiation Photo Electron Spectroscopy

TE   Thermionic Emission

TFE   Thermionic Field Emission

TRPL   Time-Resolved Photoluminescence

UV   Ultra Violet

UHV   Ultra-High Vacuum

VLS   Vapour-Liquid-Solid

WD   Working Distance

Wz   Wurtzite

XPS   X-ray Photoelectron Spectroscopy

Zb   Zincblende

Chapter 1

Introduction

1.1 The Vapour-Liquid-Solid Growth Mechanism for Nanowire Heterostructures

One-dimensional (1-D) crystal growth mechanisms emerged in the early 1960's when Wagner and Ellis revealed the details of their study on the growth of silicon whiskers [1]. The silicon whiskers were grown in the presence of a gold droplet which acted as a catalyst for the nanowire (NW) growth. Since vapour, liquid and solid phases were involved in the growth mechanism through the source material component, catalyst alloy and precipitated crystal structure, respectively, the growth mechanism became known as vapour-liquid-solid (VLS) growth [2]. Later, the promising physical, chemical and mechanical properties of NWs compared to bulk materials, owing to quantum confinement effects and large surface to volume ratio, were demonstrated. Since NWs can accommodate the induced strain in lattice-mismatched heteroepitaxy, they can be grown on substrates with different lattice constants [3]. On the basis of the novel properties of NWs, the idea of NW-based optoelectronic devices such as

lasers [4], solar cells [5,6], field-effect transistors (FET) [7,8], photodetectors [9,10], sensors [11] and light-emitting diodes (LEDs) [12] were developed. The physical and chemical properties of NWs such as length and diameter, doping type and concentration, growth orientation, structural defects, surface states and facets alignment, are closely related to the growth mechanism and directly affect the functionality of the optoelectronic devices. The VLS growth is a controllable mechanism which can manipulate the above mentioned properties of NWs in a simple way and is widely used in the field of NW research. Fig. 1.1 schematically shows the VLS growth mechanism for NWs. As can be seen, the VLS mechanism includes three main steps: alloying (Fig. 1.1b), precipitation (Fig. 1.1c), and axial growth (Fig. 1.1d).
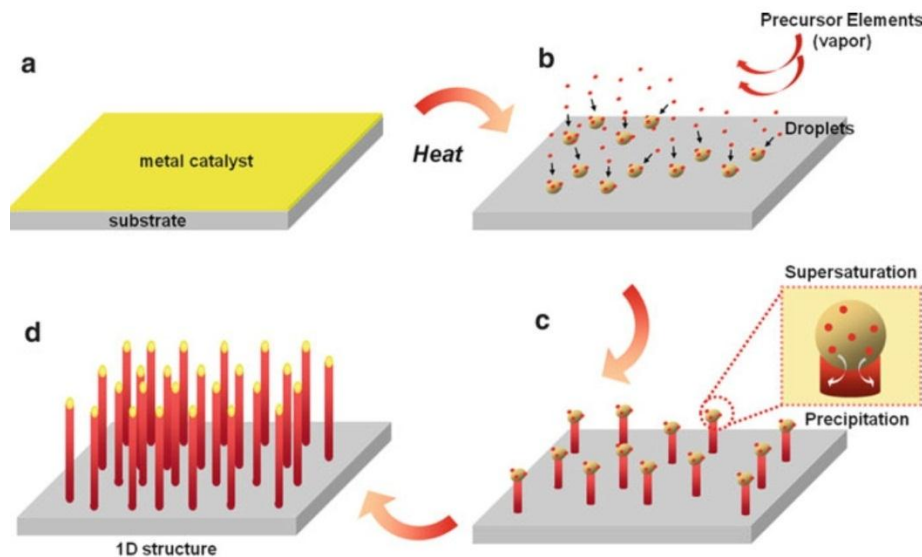
Figure 1.1: NW growth through VLS mechanism. Adapted from [2].

The VLS mechanism requires a metal catalyst for the crystal growth to happen. As shown in Fig. 1.1a, a layer of a metal catalyst with specific thickness is deposited on the substrate by sputtering, thermal or electron beam evaporation. The thickness of the deposited metal depends on the desired diameter for the NW and is usually around a few nanometers. Then, the substrate is annealed at temperature higher than the eutectic point of the metal-semiconductor substrate to form metal droplets on the surface as in Fig. 1.1b. This step can also be performed on the pre-patterned substrate using electron beam lithography (EBL) to control the size and position of the droplets. After droplet formation, the growth of the NWs is initiated by the impingement of the growth species in the vapour phase on the substrate and the metal-alloy droplet. When the liquid alloy becomes supersaturated, the precursors start to precipitate at the interface between the liquid alloy and the substrate (Fig. 1.1c). The length of the NWs depends on the growth duration. By stopping the flux of the vapour components onto the substrate, the growth will be terminated as shown in Fig. 1.1d. The growth direction of the NWs depends on the surface orientation of the substrate and is favorable along the $<111>$ direction. It has been demonstrated that the surface free energy of the liquid-solid interface is minimum in the $<111>$ direction [1, 13]. The NWs grown in this direction have shown higher density of twin stacking faults in comparison to other directions [14].

1.1.1   Metal Catalysts Requirements

Although a metal catalyst is essential for driving the VLS growth of NWs, there have been some issues related to contamination caused by the contact with the semiconductor at high temperatures [15]. In some cases the diffused metal can act as an impurity in the semiconductor and degrade the optical and electrical properties of the NW.

In general, the metal should satisfy some requirements before being used as a catalyst in the VLS mechanism [2]. It should be able to make a solution with the solid semiconductor components at the NW growth temperature. It's solubility in the solid and liquid phase of the host material should be low to reduce the contamination. The catalysts should remain on top of the NWs during the growth, so their vapour pressure over the liquid alloy should be low to prevent evaporation. They should also be inert and not react with the host material.

According to the above mentioned requirements, different metals have been used for the VLS growth of NWs, which are mostly noble and transition metal elements. For example, Au is widely used for the growth of Si and Ge, ZnO and III-V semiconductors such as InP, GaAs, and InAs [16, 17]. Other metals such as Al, Ti, Ni, Fe, and Cu are also used as catalysts [18, 19, 20].

To overcome the limitations produced by catalyst-assisted growth,

self-catalytic VLS mechanisms have been developed in recent years [21, 22, 23]. In this method one of the components forming the NW plays the role of catalytic droplet and drives the VLS growth. For example, in the case of InP, In droplets and in GaAs, Ga droplets work as catalysts [24, 25]. These droplets are formed on a full or patterned layer of SiO_2 deposited on the substrate.

1.1.2 Effect of Growth Parameters on Morphology of the Nanowires

Although the diameter of NWs can be adjusted by the size of the catalyst droplet, the minimum size of the droplet (R_m) and in turn the diameter of the NW is thermodynamically restricted according to the following equation [2]:

$$R_m = \frac{2v_l}{RTln(s)}\sigma_{lv} \tag{1.1}$$

where v_l is the molar volume of the droplet, σ_{lv} is the liquid-vapour surface energy, and s is the degree of supersaturation of the vapour. Eq. 1.1 shows that a higher degree of supersaturation is necessary to achieve smaller droplets.

The growth rate of the NW depends on the NW diameter. According to the Gibbs-Thompson effect, the axial growth of the NWs with larger diameter is faster due to the higher supersaturation of the alloy droplet which is the driving force for the NW growth. The chemical potential of

the precursors in the droplet becomes high as the size of the droplet decreases:

$$\Delta\mu = \frac{2\gamma}{r} \tag{1.2}$$

where $\Delta\mu$ is the chemical potential difference of the precursors in the liquid droplet, γ is the surface energy and r is the radius of the droplet. Higher chemical potential leads to lower solubility of the vapor species in the droplet which makes it difficult to reach supersaturation.

The morphology of the NWs can be adjusted by four main parameters in VLS growth. The size of the catalyst droplet, the growth temperature, the flux ratio of the species (for III-V growth, the V/III flux ratio) and the growth rate. The temperature affects the diameter of the NWs prior to growth and the length of them during the growth. At higher temperature, the droplets can migrate freely on the surface and by coalescing together yield larger droplet size and in turn larger NW diameter. During the growth, higher temperature increases the diffusion of adatoms from the substrate to the tip of the NW and assists the axial growth. There is a temperature beyond which desorption of adatoms from the surface starts. The balance between these two stages should be obtained for optimal growth. Increasing the flux of group V species helps the axial growth of the NW by compensating the desorption of group V adatoms especially at higher temperatures.

1.2   Semiconductor Surface Passivation Methods

The surface of the crystal corresponds to an abrupt change in the periodic pattern of chemical bonds. This interruption leaves some unsaturated chemical bonds which are called dangling bonds. To minimize the surface energy, dangling bonds can change their arrangement (surface reconstruction) and/or get saturated by adsorbing atoms such as oxygen. Both the disruption in the periodicity of the crystal and adsorption of adatoms modify the electronic states at the surface and result in the formation of localized surface states with energy levels (E_s) somewhere in the bandgap or valence band or conduction band. At high density of surface states, charge accumulation and release occur through the E_s levels without altering the Fermi level position. This effect is called Fermi level pinning. Under this condition, a barrier height formed at the surface is independent of the deposited metal work function. For example, GaAs Fermi level pinning due to the wide range of adsorbents is reported to be ~ 0.8 and $\sim 0.5\, eV$ above the valence band for donors and acceptors, respectively, while for InP the pinning is much lower and is ~ 1.2 and $\sim 1\, eV$ for donors and acceptors, respectively [26].

Free carriers in the bulk of doped semiconductors can be trapped in the empty surface states and leave a depleted region inside the bulk with a charge amount equal to the surface charge with opposite sign. Depending on the density of surface states and dopant concentration, the width of the depletion region can vary. In equilibrium, the potential

inside the bulk and outside the depletion region should be constant. To satisfy this condition, the energy bands at the surface start to bend upward or downward for n-doped or p-doped semiconductors, respectively. Band bending suppresses further migration of free carriers from the bulk to the surface. The amounts by which the band bending happens can be obtained by solving Poisson's equation:

$$\nabla^2 \psi = -\frac{\rho}{\varepsilon}$$

(1.3)

where ψ is the potential, ρ is the space charge per unit volume, and ε is the dielectric constant of the semiconductor. The band bending reduces the radiative recombination by spatially separating the carriers and in turn decreases the PL intensity measured from a semiconductor (Fig. 1.2).

The thermal velocity of carriers in the conduction and valence band of a semiconductor is around 10^7 cm/s. At equilibrium, there is a balance between the number of carriers moving in one direction with carriers moving in the opposite direction. So, the total current density due to the thermal motion of carriers is zero [26]. When recombination takes place at the surface of a semiconductor, a net flow of carriers toward the surface is established. The rate of the loss of carriers due to this current is defined by the surface recombination velocity S $\left(\frac{cm}{s}\right)$. For high efficiency devices S should be as low as possible.
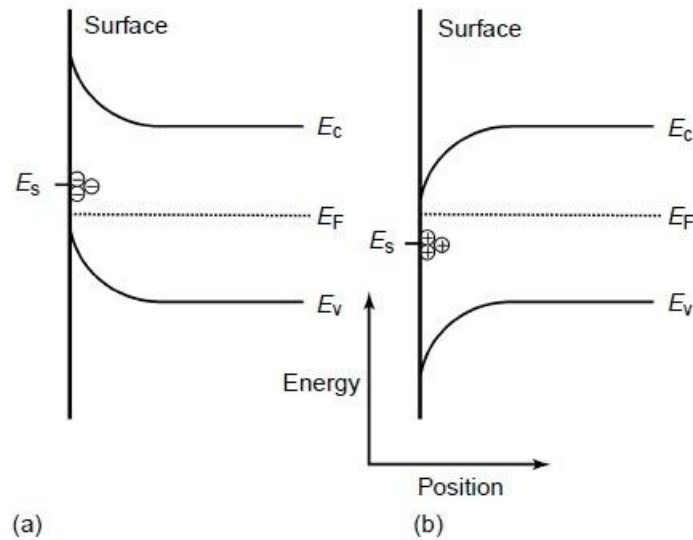
Figure 1.2: Upward (a) and downward (b) band bending due to the electron and hole accumulation in surface energy levels (E_s). Adapted from [27].

III-V semiconductors have been vastly used in optoelectronic devices for many years. It has been shown that the surface of most III-V semiconductors contain a high density of surface states which can degrade the functionality of the devices by trapping the free carriers and by strong Fermi level pinning around the midgap.

In recent years, by developing the idea of micro- and nano-scale devices, the importance of surfaces and interfaces have become more clear. Since the surface quality and device performance are intimately related, various surface treatment methods called passivation have been carried out to lessen the devastating effects of the surfaces and interfaces [28]. Passivation reduces the density of surface states and prevents their later formation, as well as protecting the surface from destructive reactions with

its surrounding which is usually atmosphere [29]. Semiconductor surfaces can be passivated by depositing a thick layer (thickness around tens of nanometers to microns) of insulator such as native oxides or changing the electronic structure of the surface using group V-VII atoms [28]. Unlike SiO_2, which is an ideal passivation layer for Si with a low density of interfacial states, the interface of III-V semiconductors and their native oxides contain many defect sites [30]. Passivation by large bandgap lattice-matched semiconductors such as AlGaAs [31] or InGaP [32] have also been reported.

Chalcogenide passivation (surface treatment by sulfur or selenium) is another passivation method which was mainly developed after 1987 when Sandroff et al. showed enormous enhancement in the gain and PL from a GaAs/AlGaAs heterostructure bipolar transistor by spin coating a layer of an aqueous solution of sodium sulfide ($Na_2S : H_2O$) on the device [31]. Later, Carpenter et al. used both Na_2S and another inorganic sulfide solution of ammonium sulfide $(NH_4)_2S$ to passivate GaAs p-n homojunctions and observed better improvement with a much slower aging after $(NH_4)_2S$ treatment [33]. To increase the effectiveness and stability of sulfur passivation, alkaline solutions instead of aqueous ones was suggested [34]. Solutions containing a solvent with higher permittivity can make stronger covalent bonds and exhibit higher PL intensity. It was also shown that external excitation in the form of heating

the solution under light illumination can facilitate the passivation procedure [35, 36]. Since the sulfur passivation is the subject of the current thesis, the process of passivation will be discussed in more details in the following.

To perform sulfur passivation, a semiconductor should be in contact with the solution containing a certain concentration of sulfide for a limited time. As mentioned before, it is better to place the solution under light illumination at high temperatures $\sim 62\,°C$ to get optimal passivation [28]. As shown in Fig. 1.3, sulfur passivation occurs in three consecutive steps. The removal of native oxide by the solution leaves free bonds at the surface for later bond formation with sulfur (Fig. 1.3a). Electrons from the conduction band of the semiconductor are transferred to the solution to neutralize the hydrogen ions (Fig. 1.3b). Chemical bond formation between sulfur and semiconductor atoms occurs (Fig. 1.3c).

The chemical reaction which takes place during the passivation process can be described by [28]:

$$A^{III}B^{V}+HS^{-}+R\text{-}OH \rightarrow (A^{III})_{x'}S_{y'}+(B^{V})_{x''}S_{y''}+R\text{-}O^{-}+H_2\uparrow \qquad (1.4)$$

where R is either a hydrogen atom for aqueous solutions or an alkyl group for alcohol solutions.

Bessolov et al. [37] proposed a model in terms of electronegativity to explain the formation of chemical bonds between semiconductor atoms and sulfur ions during sulfidizing from solution. According to this model, overlapping between the wave function of sulfur's valence electrons and

orbitals of semiconductor surface atoms occurs in such a way as to bring closer the electronegativity of both, until they become identical. As a result of leveling of the electronegativity values, the electron work function of the semiconductor differs from the starting value φ_0 by an amount $\Delta\varphi$. The characteristic electron work function (φ^c_0) was defined in such a way that if $\varphi_0 > \varphi^c_0$, the semiconductor work function would be lower and if $\varphi_0 < \varphi^c_0$, the work function would be higher after sulfidizing and no change if $\varphi_0 = \varphi^c_0$. φ^c_0 is determined by the effective electronegativity χ^0_i of the sulfur ion in solution which consists of two contributions: the electronic potential of an isolated sulfur ion in solution, and the energy of the electrostatic interaction between the sulfur ion and the semiconductor atoms. The first contribution depends on the solution properties like temperature, concentration, pH, and dielectric constant but the second contribution is affected by both the solution and the properties of the semiconductor. The potential of the electrons of the sulfur ions in solution decreases with temperature while the electrostatic interaction of the sulfur ions with the semiconductor surface atoms increases with temperature.

The effect of sulfur passivation has been greatly studied on III-V thin film devices in recent decades and has been shown to greatly improve the optical and electrical properties of the devices [31, 33, 38, 39]. Characterization of the surface of a semiconductor after $(NH_4)_2S$

chemical treatment is performed by different spectroscopy methods such as X-ray photoelectron spectroscopy (XPS), synchrotron radiation photoelectron spectroscopy (SR-PES), photoemission spectroscopy (PES), Raman scattering, and Auger electron spectroscopy (AES). These methods provide information about the chemical bond formation between the sulfur and semiconductor atoms. It has been shown that the native oxide of InP is mainly composed of In_2O_3 with some $InPO_3$ and $InPO_4$ [40]. Sulfidization removes the native oxide from the surface and encourages sulfur reaction with semiconductor atoms. The passivated surface of InP consists of a thin layer of InS and In_2S_3 with no evidence of P-S bonding which is in agreement with the high solubility of P-S bonds in $(NH_4)_2S_x$ solution [41]. Thus, In-S bond formation is the major part of the passivation process for InP. Han et al. [42] investigated the degradation behavior of sulfur treated InP with XPS and PL measurements at 9K. They explained the oxidation process after $(NH_4)_2S_x$ treatment by two mechanisms. One is formation of In-O which is more stable than In-S and the other is penetration of oxygen through the sulfur overlayer and oxidizing the underlying InP and leaving the In-S layer unoxidized. They claimed that according to their results, the second mechanism is more probable to happen. It was concluded that a thick sulfur overlayer increases the stability of a sulfur-treated surface.

The native oxide of GaAs is a mixture of all possible oxide bonding

for both Ga and As such as As_2O, AsO, As_2O_3, Ga_2O, GaO, and Ga_2O_3 including elemental As [43]. The sulfur passivation results in the complete removal of the oxide layer and formation of As-S and Ga-S bonds [44, 45]. Measurements show that Ga-S bonds are stronger than As-S bonds. It has been observed that the oxidation for a sulfur passivated surface of GaAs is slower than a non-passivated surface [46, 47]. Re-oxidation of a sulfidized GaAs surface varies for different surface orientations. For (100) the oxidation happens very quickly. It is also shown that Ga oxide formation appears more rapidly than As [46].
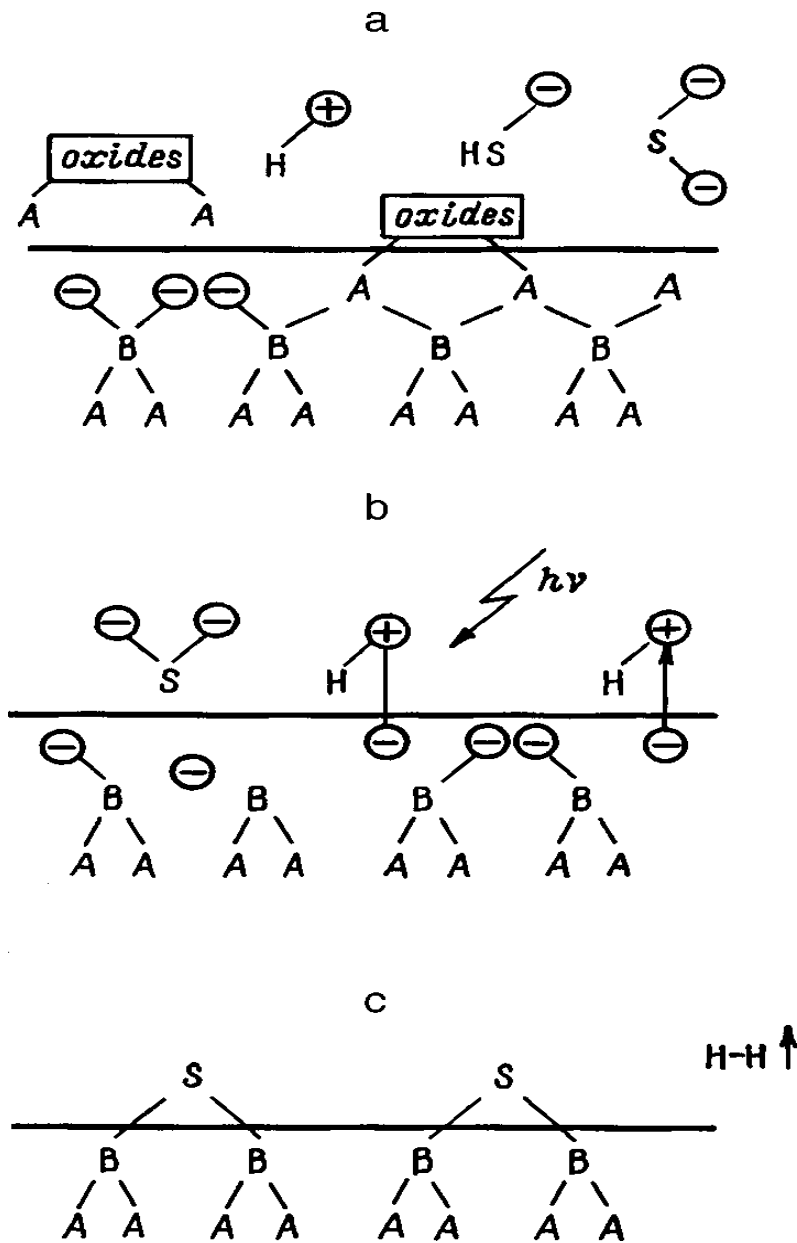
Figure 1.3: Schematic diagram of the process during the sulfur passivating layer formation: (a) etching the native oxide, separating the HS^- ions and breaking the covalent bonds between the III and V atoms. (b) electron transfer from semiconductor to the solution. (c) chemical bond formation between sulfur and semiconductor atoms and release of H_2. Adapted from [28].

The miniaturization of electronic and optoelectronic devices toward the nanoscale has been accompanied by a larger influence of surfaces and interfaces on the device functionalities due to the higher surface to volume ratio. This fact encourages more attention to the surface passivation of NWs. In recent decades, many studies have been focused in the field of NW growth and device manufacturing. Although NW-based devices have been shown to be a potential candidate for future optoelectronic applications, there are many challenges which should be overcome to obtain high efficiency devices. In comparison to surface passivation of planar structures, surface passivation of NWs seems to be more challenging due to the small size and several facets with different orientations [48]. There have been few studies on surface passivation of NWs. The photocurrent measured from single ZnO NWs under ultraviolet (UV) illumination was shown to be two orders of magnitude larger than that under the dark condition and was attributed to the decrease of the depletion width and the reduction of the contact barrier height [49]. ZnO NW-based FET annealed under the flow of H_2/Ar for 20 min, notably increased the peak transconductance from 40 to 448 nS, the field effect mobility from 27 to 302 $cm^2V^{-1}s^{-1}$, and I_{max}/ I_{in} ratio from 1.5 to 10^5 [51]. The observed enhancements were attributed to the reduction of surface trap charges under H_2 flow annealing. The surface of Si NWs, treated by dilute hydrofluoric acid (HF), was investigated using Fourier transform infrared

(FTIR) spectroscopy [51]. It was shown that HF removes the native oxides from the surface of the NWs and leaves the hydrogen-passivated surfaces behind, which showed good stability in air and poor stability in water.

Seo et al. showed that replacing the native oxide on the surface of the Si NWs by a high quality thermally grown SiO_2 resulted in the reduction of the surface charge density by a factor of two to four and increased the effective diameter and the conductance of the NWs [52]. In situ passivation of Si NWs by a thin layer of amorphous Si (a-Si) exhibited a two-fold reduction in the surface recombination velocity from 3×10^5 to 4.5×10^3 cm/s [48].

ZnO NW FETs passivated with a bilayer of SiO_2 /Si_3N_4 exhibited an increase in the on/off ratio from 10^3 to 10^4 and carrier mobility enhancement from 20-80 to 1200-4120 $cm^2V^{-1}s^{-1}$ [53]. These improvements were attributed to the passivation of surface states defects and reduction of chemisorption processes at oxygen vacancy sites. Si NW FETs passivated by SiO_x were demonstrated to have increased transconductance form 45 to 800 nS and average mobility enhancement from 30 to 560 $cm^2V^{-1}s^{-1}$ [54]. The effect of nanoscopic self-assembled superlattices (SAS) [55] on ZnO NW FETs was claimed to be more effective rather than a conventional SiO_2 passivation layer [56]. SAS-based ZnO NW-FETs showed low threshold voltage of -0.4 V, a channel mobility of 196 $cm^2V^{-1}s^{-1}$ and on/off current

ratio 10^4.   InP NWs used as a channel in NW FETs, covered with a monolayer of cobalt phthalocyanine (CoPc), exhibited on/off ratio more than 10^4 [57].

Improvement in electrical and optical properties of GaAs NWs was reported by the growth of a shell material with larger bandgap around the NW as a passivant layer. AlInP [58] was reported to increase the PL from GaAs NWs by 14 times and the current density by two orders of magnitude. According to the model developed, these improvements were credited to the reduction of surface recombination velocity from 1.8×10^4 to 5400 cm/s due to the decrease of surface density of states from 3×10^{12} to 9×10^{11} cm^{-2}. AlGaAs encapsulation of GaAs NWs was presented to decrease the surface recombination velocity around one order of magnitude up to 3×10^3 cm/s [59] and increase in the mobility from 1200 to 2250 cm^{2}V^{-1}s^{-1} [60]. Suyatin et al. reported that sulfur passivation resulted in ohmic contact formation of InAs NWs [61]. Passivation of InAs NWs with 1-octadecanethiol (ODT) is shown to increase the mobility of carriers due to the reduction of surface traps density and formation of In-S bonds at the surface from 2100 to 3200 cm^{2}V^{-1}s^{-1} [62].

Surface passivation of InP in a solution of butanol/HF/trioctylphosph-ine oxide (TOPO), accompanied by encapsulation of NWs with TOPO ligand, resulted in a 10 fold increase in luminescence efficiency [63].

The improvements observed after surface treatment of semiconductors

was mostly attributed to the decrease of density of surface states [31, 64, 65].

To increase the stability of sulfur passivation, reoxidation of the passivated surface is inhibited by encapsulating the surface with an insulator layer [29, 66, 67].

The choice of sulfur passivation for this study was mainly due to the requirement of very thin passivant layer for making NW networks. The passivant layer should allow the carriers to tunnel through the surface of the NWs.

1.3 Photoluminescence as a Tool for Surface and Interface Characterization

PL is a process of light emission from a material under optical excitation. During this process, the absorbed photons with sufficient energies can excite electrons from a ground state to higher excited states. The excited states are not stable and in the process of radiative recombination, the electrons relax back to the ground state which is accompanied by photon emission. Analyzing the emitted light can provide a wide range of information about the photoexcited material. The PL spectrum yields information about transition energies and impurity levels while PL intensity represents the relative rate of radiative and nonradiative recombination, and the quality of surfaces and interfaces [27]. The variation of bandgap in semiconductor alloys, such as $Al_xGa_{1-x}As$ by

changing the compositional parameter x and also in semiconductors with different structures such as zincblende or wurtzite, can be determined by their PL spectrum [68].

Since PL is a nondestructive characterization technique, there is no need for sample preparation. Since PL is generated near the surface of the material, it is an appropriate technique for surface assessment of materials and monitoring of applied surface modifications. PL can be varied by external parameters such as the energy and intensity of the incident light, temperature, applied voltage and surface modifications [27].

The excitation energy of the incident light can be adjusted to target specific depths in the sample. Photons with higher energies are absorbed near the surface and the measured PL is dominated by surface recombination while photons with lower energies can penetrate deeper into the sample and the PL is mostly dominated by bulk recombination [27]. The effect of PL quenching by nonradiative recombination has been used for the measurement of depletion layer thickness formed at surfaces with a high density of states [69].

The existence of different electronic states in the material can be recognized by the absorbed or emitted photons with specific energies. Although absorption is appropriate for overall band structure investigations, PL emission is suitable for detecting low lying states such

as the ones for surfaces and interfaces with discrete states [27].

To obtain a PL spectrum with sharper peaks and smaller bandwidth, the sample should be cooled below room temperature. Lower temperature reduces thermal broadening of the excited energy levels and prevents thermal ionization of impurities [68]. Usually, liquid helium is used for cooling processes.

Both S and surface band bending result in non-radiative recombination and therefore tend to decrease the PL intensity. To separately determine the effect of each on the PL intensity, further investigations such as surface potential measurements are required. S is shown to be proportional to the surface density of states [26]. Although changes in the density of states can affect the band bending, the change in the band bending doesn't necessarily mean that the surface state density is changed [27]. Sometimes the distribution of the electrons at the surface can be perturbed by surface treatments or by absorption of gas molecules. This perturbation can change the band bending by modifying the electric field at the surface without affecting the density of states.

Different surface treatments such as etching, dielectric deposition, oxygen and hydrogen termination, heteroepitaxy, and gas adsorption are evaluated using PL intensity measurements [27]. Any change observed in the measurements is mostly explained on the basis of changes in the density of surface states and/or surface potential.

In addition to continuous wave (CW) excitation for PL measurements, short laser pulses can also be used for electron excitation which is called time-resolved PL (TRPL). After pulsed excitation, the excited carriers start to recombine with a rate which depends on the recombination mechanism. The lifetime of photogenerated carriers can be determined by a TRPL signal. Surface recombination in NWs strongly affects the life time of photogenerated carriers due to the high surface to volume ratio. Since the surface passivation can change the density of surface states and as a result the quality of the NWs surface, TRPL measurement can be used to provide strong evidence for the effectiveness of passivation by measuring the lifetime of photogenerated carriers. This method has been vastly employed on the passivated surfaces and showed enhancement of the carrier lifetime after surface passivation [27].

It was mentioned that steady-state excitation PL cannot resolve the contribution of surface density of states and band bending in the PL intensity variations. But transient PL measurements have been shown to be able to separate these contributions [70]. At sufficiently high injection levels, the effect of band bending diminishes by band flattening effects and all the measured changes in the carriers' lifetime can be attributed to the changes in the surface density of states.

Hence, the PL intensity has been used as a measure of the surface quality [71, 72] and the effectiveness of surface treatments can be evaluated by comparing the PL intensity before and after the treatment.

1.4 I-V Characterization for Nanowires

Surface states can strongly affect the contact quality between the metal and semiconductor [73, 74] and the series resistance [75]. Changes in the density of states by surface treatments can be observed by measuring I-V characteristics. Metals deposited on semiconductors form a barrier at the interface which controls the current conduction. The band diagram of both a metal and n-type semiconductor which are separate is shown in Fig.1.4a, where $e\Phi_m$ is a metal work function, $e\chi_s$ is the electron affinity of the semiconductor, and E_C , E_V , E_F are the conduction band, valence band and Fermi level, respectively. When both materials are brought together, a so called metal-semiconductor (MS) structure is formed (Fig. 1.4b). To establish thermal equilibrium in the new system, the charges, here the electrons, start to transfer from the semiconductor to the metal until the Fermi levels become equal on both sides (Fig. 1.4c). The Fermi level lowering is equal to the difference between the work functions of the metal ($e\Phi_m$) and the electron affinity of the semiconductor ($e\chi_s$) and is called the barrier height ($e\Phi_b$) (Eq.1.5). There is also a depletion layer (W_D) and diffusion potential (V_D) formed at the interface of the metal and semiconductor:

$$e\Phi_b = e\Phi_m - e\chi \qquad\qquad (1.5)$$

The energy-band diagram of the MS structure under different applied bias for both p- and n-type semiconductors is shown in Fig. 1.5. The barrier height for carriers decreases (increases) after applying forward bias (reverse bias) according to the applied voltage.

There are various transport mechanisms for electrons under forward bias across the MS junction [77]. The processes are: 1) thermionic emission, 2) tunneling, 3) recombination in the depletion region, and 3) recombination in the neutral region.
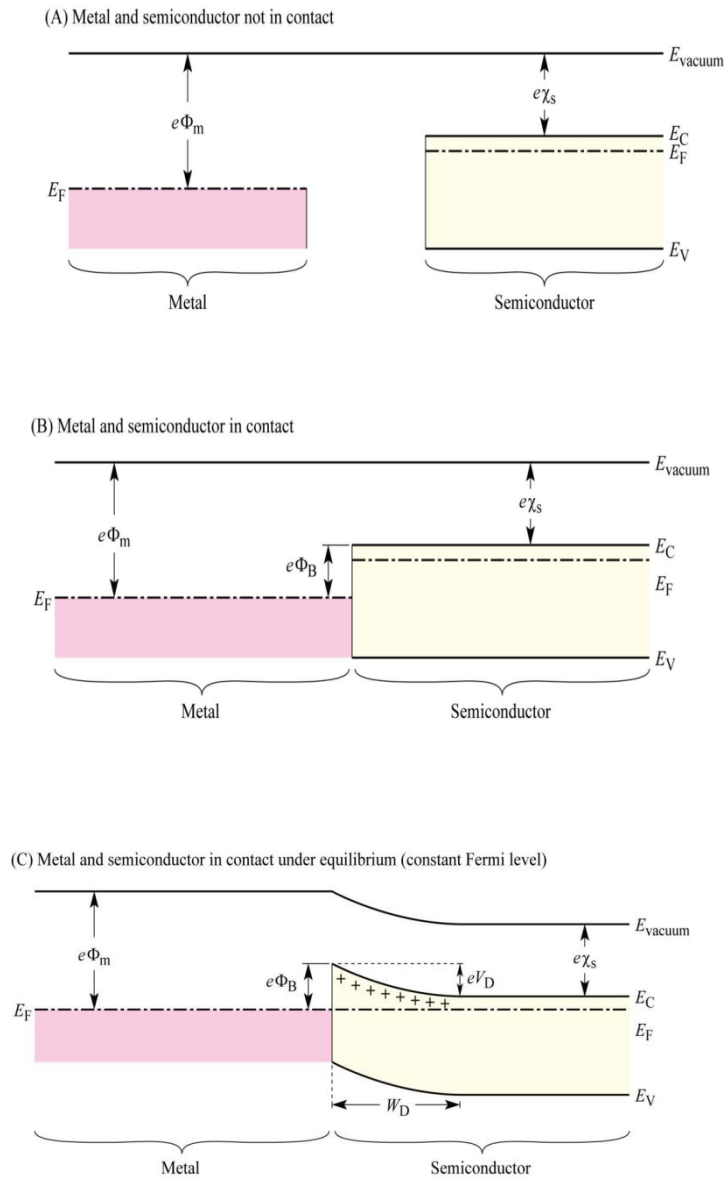
Figure 1.4: Band diagram of a metal-semiconductor structure (a) before contact, (b) after contact, and (c) after contact under equilibrium. Adapted from [76].
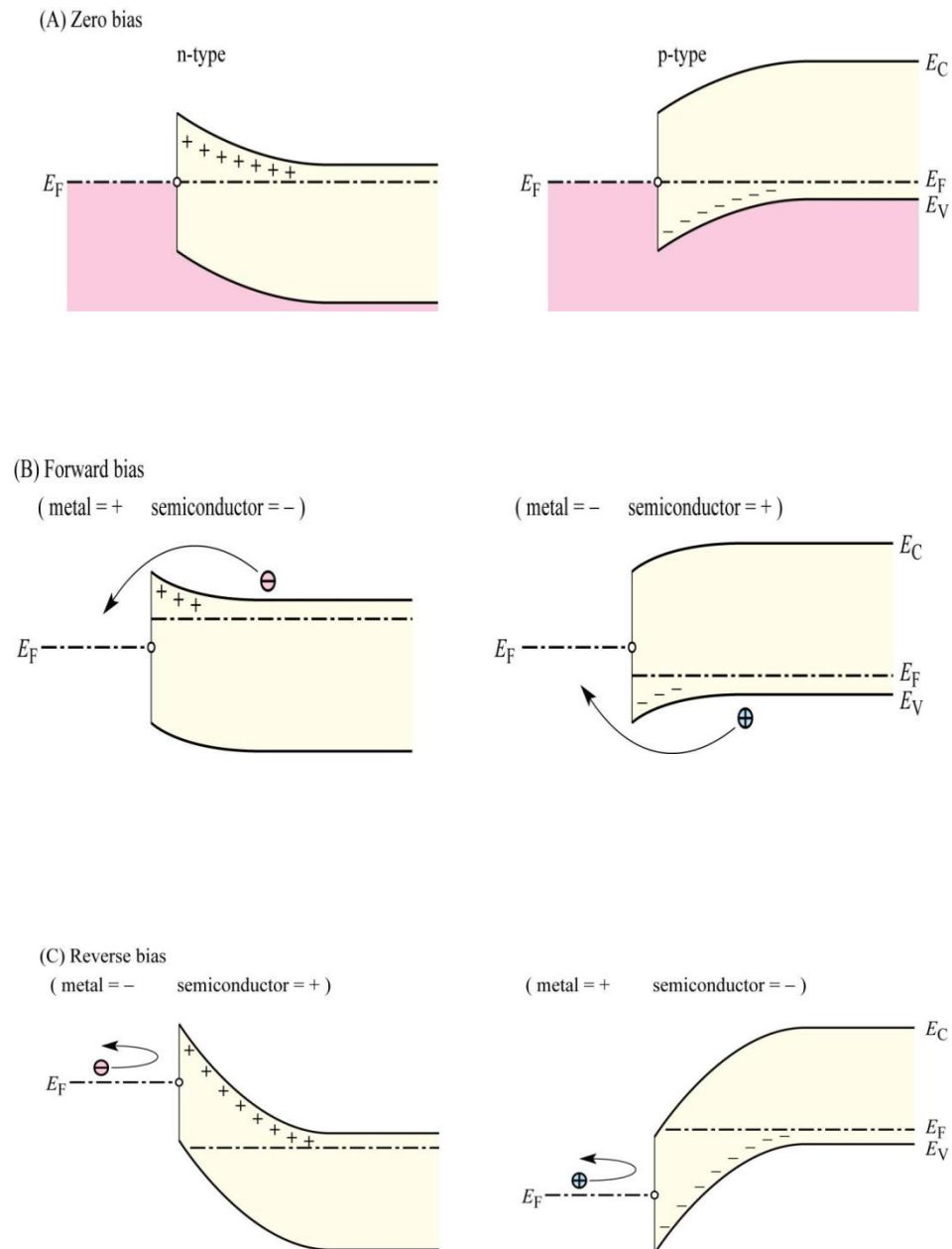
Figure 1.5: Band diagram of metal-semiconductor structure under (a) zero bias, (b) forward bias, and (c) reverse bias. Adapted from [76].

The current transport through the MS structure for high mobility semiconductors like GaAs is normally discussed using thermionic-emission theory. According to this theory, the current density equation of a Schottky barrier is given by [77]:

$$J_{TE} = A^* T^2 exp\left(-\frac{q\varphi_b}{kT}\right)\left\{exp\left(\frac{qV}{kT}\right) - 1\right\}$$ (1.6)

where $A^* = \dfrac{4\pi q m^* k^2}{h^3}$ is the effective Richardson constant and φ_b is the barrier height.

Thermionic emission (TE) theory neglects the tunneling effect through the MS junction. The tunneling current is specifically important in reverse-biased Schottky barriers. According to the thermionic field emission (TFE) theory which includes the tunneling effect, the current density due to TFE from the Schottky barrier under forward bias is given by [77]:

$$J_{TFE} = \frac{A^{**} T \sqrt{\pi E_{00} q(\varphi_b - \zeta - V)}}{k\cosh(E_{00}/kT)}\ exp\left[\frac{q\zeta}{kT} - \frac{q(\varphi_b - \zeta)}{E_0}\right] exp\left(\frac{qV}{E_0}\right)$$ (1.7)

where ζ is the energy difference between the Fermi level and the bottom of the conduction band and A^{**} is the reduced effective Richardson constant. For n-type GaAs, A^{**} is shown to be 4.4 A/cm^2–K^2. Also,

$$E_0 = E_{00} coth\left(\frac{E_{00}}{kT}\right) \tag{1.8}$$

$$E_{00} = \frac{q\hbar}{2}\left[\frac{N_D}{m^*\epsilon_s}\right]^{1/2} \tag{1.9}$$

N_d is the dopant concentration and ϵ_s is the permittivity of the semiconductor.

The current due to TFE under reverse bias is also given by [77]:

$$J_{TFE} = \frac{A^{**}T}{k}\sqrt{\pi E_{00}q\left[V + \frac{\varphi_b}{cosh^2(E_{00}/kT)}\right]}\ exp\left(-\frac{q\varphi_b}{E_0}\right) exp\left(\frac{qV}{\epsilon'}\right) \tag{1.10}$$

$$\epsilon' = \left(\frac{E_{00}}{(E_{00}/kT) - tanh(E_{00}/kT)}\right) \tag{1.11}$$

In order to measure the I-V characteristic of NWs, both sides of the NWs should be in contact with the metal electrodes. The contacts can be either Ohmic and/or Schottky barrier depending on the Fermi level position. A semiconducting NW with two contacts formed on both sides can be modeled as a metal-semiconductor-metal (MSM) structure (Fig. 1.6). Depending on the type of MSM contacts which can be either Ohmic or/and Schottky, thermionic emission theory predicts different I-V characteristics for a MSM structure. If both contacts are Ohmic, the I-V characteristic would be linear. If one contact is ohmic and the other is Schottky, a rectifying I-V is predicted.

As shown in Fig. 1.6, the equivalent circuit of the MSM structure is

two back to back diodes which are in series with the NW resistance. For n-type NW, if a positive voltage is applied on the left contact and a negative on the right contact, the Schottky barrier 1 is forward-biased and Schottky barrier 2 is reverse-biased [78].
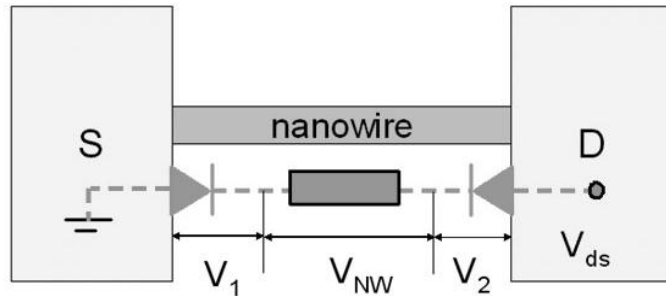
Figure 1.6: Schematic diagram of MSM structure and its equivalent circuit. Adapted from [78].

As shown in Fig. 1.6, if the voltages across contact 1, the NW and contact 2 are V_1, V_{NW} and V_2, respectively, the total voltage across the MSM structure would be:

$$V = V_1 + V_{NW} + V_2 \tag{1.12}$$

The MSM structures are mostly modeled using thermionic emission theory. However, as shown in [78], this approach underestimates the current under reverse bias in NWs. Thus, for Schottky barrier 1 which is forward-biased, the TE current from Eq. 1.6 is used. To include the tunneling effect

in the reverse-biased Schottky barrier 2, the TFE current Eq. 1.10 is used.

If we assume that the undepleted part of the NW is uniform and has a constant resistance R_{NW}, the current density through the NW is simply:

$$J_{NW} = \frac{V_{NW}}{A_{NW} R_{NW}} \qquad (1.13)$$

where A_{NW} is the cross-sectional area and R_{NW} (Eq. 1.14) is the resistance of the NW.

$$R_{NW} = \rho \frac{L_{NW}}{A_{NW}} \qquad (1.14)$$

The I-V curve of the structure shown in Fig. 1.6 can be obtained by solving equations (1.6), (1.10) and (1.13).

1.5 Motivation

In recent decades, electronic and optoelectronic devices which are mostly made of Si have been developed. III-V semiconductors, due to their direct bandgaps, are very interesting for optoelectronic applications. However, the native oxide of these materials creates defects in the bandgap and strongly limits their performance.

In contrast, SiO_2 protects the surface of Si and acts as an ideal passivation layer. The surface effects are less obvious in the performance of devices in the dimensions of microns or higher. The active region of these devices is

large enough compared to their surface, so the overall functionality is less affected by the surface imperfections. In parallel to the downscaling of optoelectronic devices, the surface to volume ratio increases, the active regions get smaller, and the destructive effect of surface defects become more important. Surface passivation was developed to resolve these surface-related drawbacks.

In recent years, there have been numerous efforts for growth and characterization of NWs. Extensive reports have been released to show the potential of NWs for many future applications. But the performance of devices still has a large gap with their bulk counterparts due to the surface effects. The surface study of NWs has been limited to the few papers mentioned previously.

For the current study, the optical and electrical properties of single and ensemble NWs were investigated in more detail. It was found that the surface passivation may assist the performance of NWs. Sulfur passivation has been widely reported to be very effective in improvement of optical and electrical properties of III-V semiconductors, but very few studies have been discussed on the effect of sulfur passivation on NWs and NW-based devices. There are many challenges for sulfur passivation of NWs due to their small size. The sulfur solution was optimized for III-V semiconductors and its effect on the optical and electrical properties on NWs was investigated.

1.6 Thesis Framework

In Chapter 1, the VLS mechanism for the growth of NWs has been introduced. The role of metal catalyst and growth parameters on the growth and morphology of NWs were discussed. The effect of surface defects such as band bending and surface recombination on the optical and electrical properties of semiconductors especially InP and GaAs thin films and NWs to lessen the destructive impacts were presented. Sulfur passivation, as a main goal of the current study, was discussed in more detail.

In Chapter 2, the working principle of the experimental tools and techniques employed for the NW growth and characterization is briefly explained. In the growth section, the definition and necessity of epitaxial growth as well as the different epitaxial growth techniques are introduced. The advantages of GS-MBE are compared to other growth techniques. The general idea of NW growth by GS-MBE is explained. The characterization part contains two sections: optical characterization and electron microscopy. The constituent elements of a μ-PL setup used for optical characterization are introduced and their operation is clarified. The significance of electron microscopy in characterization of materials is represented and a general overview of its function is schematized.

In Chapter 3, the optimization process of sulfur passivation for p-InP

NWs is demonstrated primarily by optical characterization. A theoretical model is developed to explain the observed modifications. The information reported in this Chapter is published in [79].

In Chapter 4, I-V characteristics of GaAs NWs is compared in three steps of sulfur passivation: before passivation, after just contact area passivation and after the whole NW passivation. Modeling is performed to determine the potential reasons for the measured I-V characteristics. The information reported in this Chapter was published in [67].

In Chapter 5, the effect of sulfur passivation on the efficiency of core-shell GaAs NW solar cells is shown. A comparison between Au and ITO contacts as well as the contribution of thin film growth between the NWs is discussed. The information reported in this Chapter was published in [80].

In Chapter 6, the results obtained during our studies is summarized and future potential work is mentioned.

Chapter 2

Experimental Methods

In this Chapter, the working principles of the experimental tools and techniques employed for NW growth and characterization is briefly explained. Gas-source molecular beam epitaxy (GS-MBE), micro-photoluminescence (μ-PL) and scanning electron microscopy (SEM) are discussed.

2.1 Gas Source Molecular Beam Epitaxy

For most technological applications, a growth technique for high crystal quality is desirable with precise control on thickness, composition and morphology. When the deposited atoms are arranged upon the substrate surface with the same orientation as the underlying crystalline substrate, the resulting layer is called an epitaxial (epi) layer and the process of growth is known as epitaxy. Epitaxy stems from the Greek words 'epi' and 'taxis' which mean 'upon' and 'arranged', respectively. This growth method was first developed in 1951 by G. Teal and H. Christensen at Bell Labs. Epitaxy is capable of growing highly crystalline layers with low defect density, controlled dopant concentration, interface abruptness and high surface flatness and repeatability. There are two main types of epitaxy: homoepitaxy and heteroepitaxy. If the overlayer has the same

composition and structure as the substrate, the process is called homoepitaxy; otherwise it is described as heteroepitaxy.

Depending on the physical state of the material (ie. liquid or vapor) used for epitaxial layer formation, different techniques for epitaxial growth have been developed such as liquid phase epitaxy (LPE), physical vapor deposition (PVD), metal organic chemical vapor deposition (MOCVD) and molecular beam epitaxy (MBE) [81]. The growth techniques are chosen to satisfy the desired requirements. For example, LPE and MOCVD are desirable if high yield and low cost is needed. The low growth temperature and growth rate make MBE convenient for high quality epitaxial surfaces and interfaces and superior control on the abruptness of the junctions and doping profile. MBE has been widely used for growing III-V semiconductor structures since the 1970s. In solid-source MBE, III-V semiconductor structures are all formed by species evaporated from the heating of solid sources in effusion cells. The evaporated atoms pass through an ultra-high vacuum (UHV) environment of the growth chamber after emerging from the cells, and get condensed on the heated substrate. The UHV conditions increases the mean free path of the molecular or atomic beams in such a way that there is no collision between atoms or molecules before they impinge on the wafer surface. After arriving at the surface, the atoms diffuse on the substrate and react to form a single crystal structure. In GS-MBE, group V species are supplied from gas crackers as dimers, while the group III elements are generated from solid source effusion cells as monomers.

A schematic diagram of a typical MBE system is shown in Fig. 2.1. Before loading the wafer inside the growth chamber, it is passed through a

load-lock chamber and then degassed in a preparation chamber.
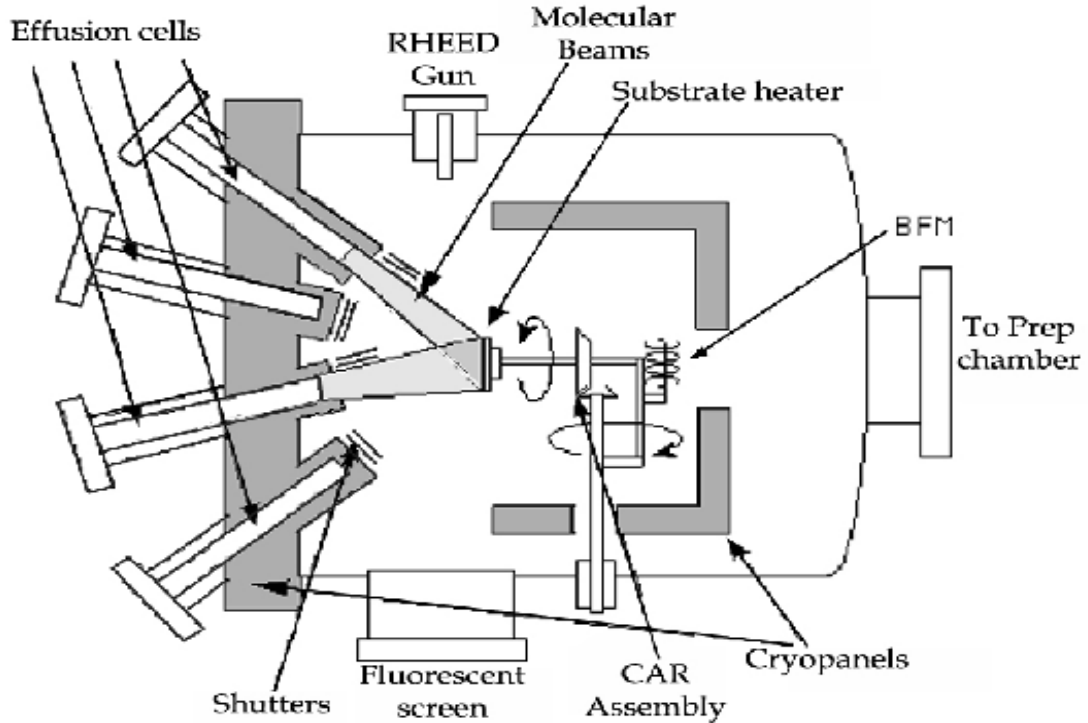
Figure 2.1: A schematic diagram of a MBE growth chamber. Adapted from [81].

The main surface chamber wall and crucibles are surrounded by liquid N_2 cryopanels to prevent re-evaporation of impurities and thermally isolate the different effusion cells. The effusion cells are located at the bottom part of the growth chamber in front of the sample holder and at an angle of 35° relative to the surface normal. The effusion cells are made of temperature resistant materials, usually pyrolytic boron nitride, to endure temperatures up to $1300\,^{\circ}C$. The flux of the species from the

effusion cells is controlled by the temperature of the material sources inside the cells, measured by a thermocouple and mechanically controlled shutters located on top of the cells.

The substrate is located on the manipulator which is able to rotate continuously. There is a thermocouple which measures the substrate temperature and also an infrared pyrometer which measures the surface temperature.

All the NW growths reported in this study has been performed by GS-MBE. The growths are conducted on a pie piece obtained from cleaving a 3 inch wafer and placed in a pie-shaped holder. After degassing in the preparation chamber, it was transferred to the growth chamber, located on the manipulator and was rotated during the growth. An inductively-coupled H_2 plasma (ICP) was applied on the substrate after it reached the growth temperature. The ICP removes the native oxide on top of the wafer and helps the formation of the Au nano-particles from the previously deposited thin gold layer. To begin the growth and depending on the desired structure, group III and dopant effusion cell shutters are opened. After the growth is completed, the flux from the group III sources are blocked by the shutters and the sample is cooled under the flow of group V dimers. The group V source is also turned off when the substrate temperature reaches less than 350 °C.

After growth is completed, the sample is unloaded from the MBE and is held in plastic sample holders for later analyses.

2.2 Optical Characterization

Since PL is mostly generated near the surface of semiconductors, PL spectroscopy has been widely used for surface analysis. The surface quality of the NWs, which is the goal of this study, has been investigated by measuring the PL intensity before and after sulfur passivation. Investigation of the optical properties of single nanostructures such as single NWs cannot be performed by using a normal PL method due to the lack of spatial resolution. Applying some changes on an ordinary PL set-up made it possible to find the position of single NWs lying on a substrate. The new system is called a micro-photoluminescence (μ-PL) setup. The details of the setup and its constitutive components are explained in the following sections.

2.2.1 The μ-PL system

The experimental set-up of μ-PL spectroscopy which was used for obtaining PL from single NWs is schematized in Fig. 2.2. The excitation beam was provided by a CW He-Ne laser or Ar-ion laser. The incident beam polarization was controlled by a Glan-Thomson linear polarizer and half-wave plate. The beam was focused on the sample with $\times 10$ or $\times 60$ objective lenses. The sample consists of NWs dispersed on a SiO_2/Si substrate. For low temperature measurements, the sample was mounted on the cold finger of a cryostat. The emitted light from single NWs was collected by the same objective lens and focused on the entrance slit of the spectrometer. The collected PL is dispersed by the spectrometer and

detected by a Si photodetector.

The working principals of the optical elements in the µ-PL setup will be discussed in more detail below.
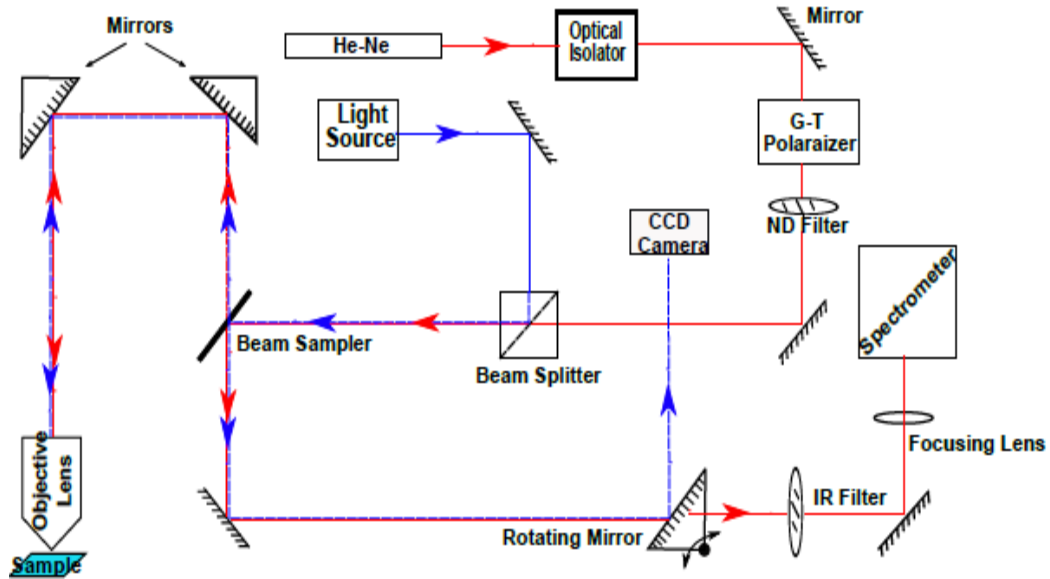
Figure 2.2: µ-photoluminescence setup.

The Lasers

A He-Ne laser with fixed wavelength (632.8 nm) and photon energy (1.96 eV), larger than the band gap of the InP (E_g = 1.37 eV), was used for excitation. The laser power measured at the sample and the beam diameter were 10 µW and 2 µm, respectively. An Ar-ion laser with photon energy of 2.54 eV was used for PL intensity dependent measurements. The laser power was tunable by applying different powers from 2 to 9 mW. The intensity of the laser was also controlled by different neutral density filters.

A neutral density (ND) filter wheel located in front of the laser beam can also be used to reduce the beam intensity. It contains glass disks which depending on the coating show different transparency from 0.015% up to 100%.

Glan-Thompson Linear Polarizer

A Glan-Thompson polarizer consists of two right-angled calcite prisms cemented as shown in Fig. 2.3. The light entering the calcite experiences different refractive indices depending on its polarization. This effect, which is called birefringence, causes the p-polarized light to be totally internally reflected from the cemented interface and the s-polarized light to be transmitted (Fig. 2.3). Thus, the Glan-Thompson prism ensures that the emerging laser light is linearly polarized.

Half-Wave Plate

The half-wave plate rotates the linearly polarized light incident on it at an angle α, relative to a vertical axis, by an angle of 2α (Fig. 2.4). The rotation of polarization is especially necessary for exciting single NWs since the light absorption is maximum for light polarized parallel to the NW length.
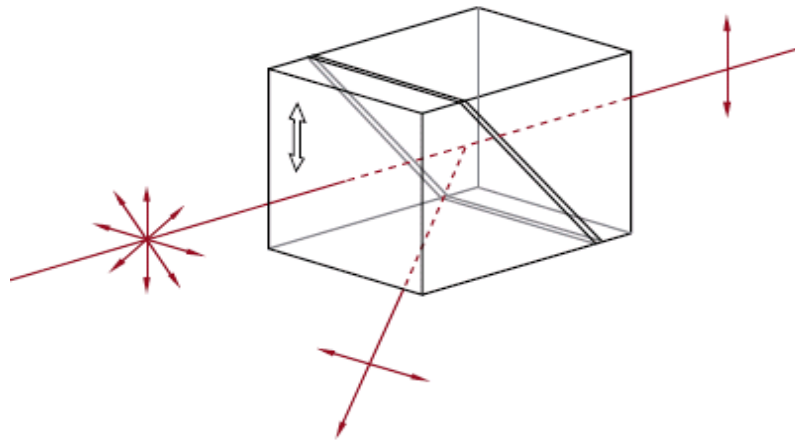
Figure 2.3: Glan-Thompson linear polarizer. Adapted from [82].
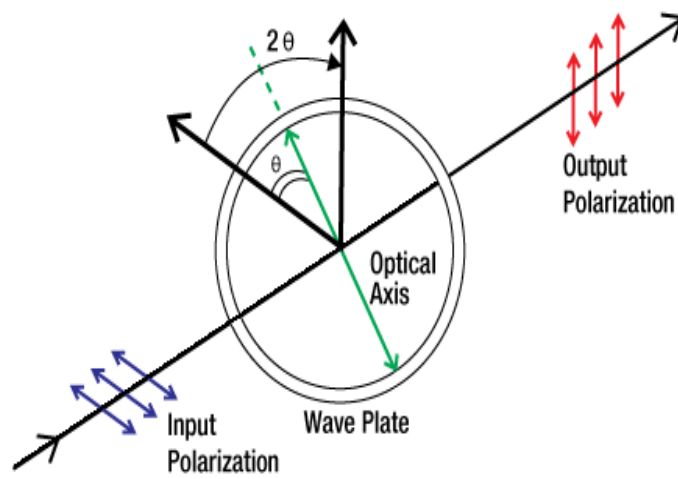
Figure 2.4: Half-wave plate. Adapted from [82].

Beam Splitter

The beam splitter is a cube consisting of two right-angled prisms attached together by their diagonal faces (Fig. 2.5). The interface surface between two prisms is coated with a dielectric layer which reflects 50% of the beam. Antireflection coatings on the entrance and exit faces diminish the back reflections.
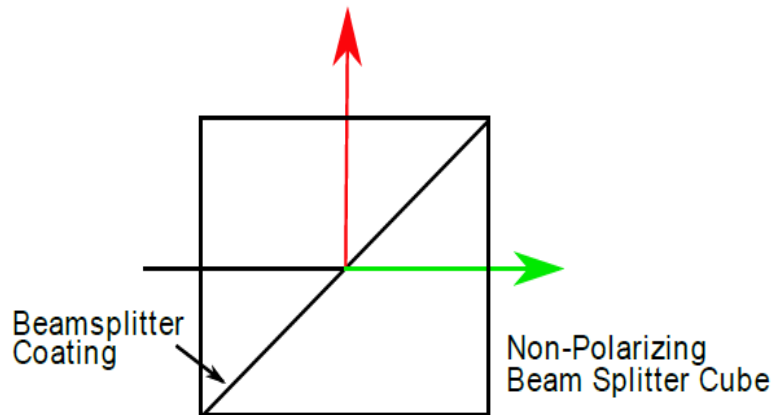
Figure 2.5: Beam Splitter.

Beam Sampler

The beam sampler is fabricated from UV fused silica. It is used to partially reflect the beam, depending on the polarization and incident angle. For $45°$ angle of incidence, 1% of the p-polarized light will be reflected, while 10% of the s-polarized light will be reflected (Fig. 2.6).

Optical Cryostat

Low temperature measurements were conducted in an optical cryostat

shown schematically in Fig. 2.7. The temperature is controlled by a temperature controller and can be varied from 5K to 300K. The cryostat is kept under a vacuum of 10 mTorr [83].
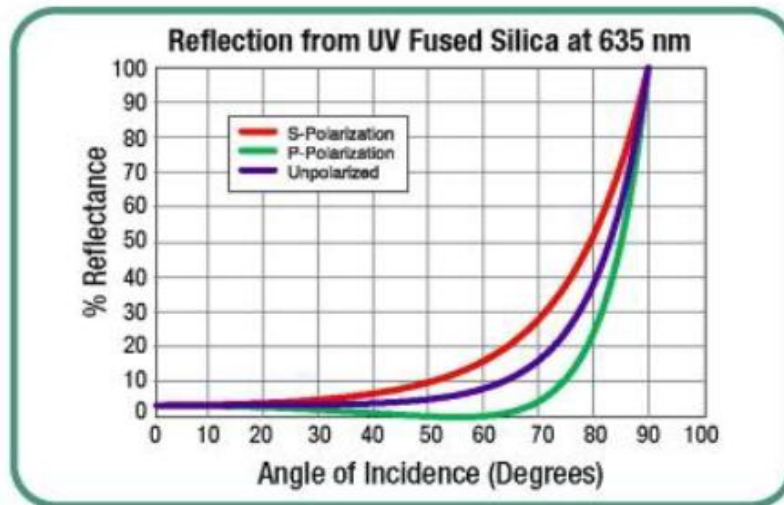
Figure 2.6: Polarization dependence of light reflection from beam sampler. Adapted from [82].
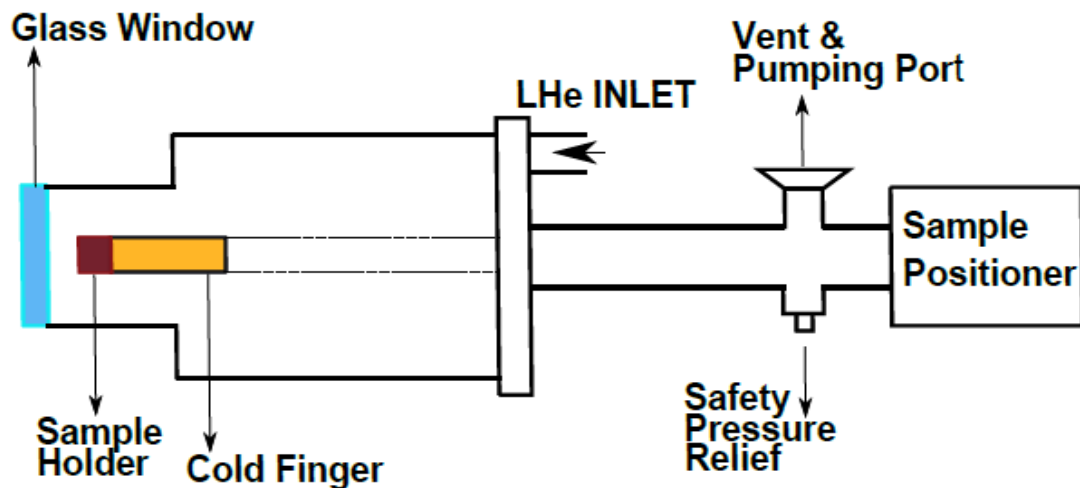
Figure 2.7: Schematic illustration of optical cryostat (Janis).

Spectrometer

The iHR550 spectrometer [84], equipped with a cooled charge coupled device (CCD) detector for the range of 400-1000 nm, has been employed to collect and analyze the PL data from the single InP NWs. Fig. 2.8 illustrates the configuration of slits, mirrors and grating of the iHR550 spectrometer [84].

The desired wavelength range for InP PL measurement is 700-950 nm. The size of entrance slits is adjustable and is chosen to be 18 μm with opening time of 10 s for optimum light capturing and noise level. The toroidal mirrors [85], used in the optical design, minimize the astigmatism associated with conventional spherical mirrors when focusing light from a point source. The curvature is different for horizontal and vertical axes of the mirror. Three gratings are mounted on an automated turret. The diffraction turret rotates the grating for different wavelength selection during the measurements. One grating contains 1200 grooves/mm which makes it convenient for PL measurement over a wide range of wavelength.

CCD Detector

A highly sensitive detector is necessary to detect the low level PL signal emitted from nanostructures such as single NWs. CCD cameras show excellent performance in optical spectroscopy due to their high quantum efficiency for conversion of absorbed photons into electrical signal. A Symphony cryogenic back illuminated CCD camera is used to detect PL intensity versus wavelength of single NWs that have emission in

the range of 800-900 nm. The quantum efficiency of this detector for different wavelengths is shown in Fig. 2.9. The working principle of a CCD camera is briefly described below. A CCD consists of a closely spaced array of metal-oxide-semiconductor (MOS) capacitors which are called pixels [87, 88]. The active region of the CCD is an epitaxial layer of p-silicon (usually boron doped) which is covered by a layer of an insulator (silicon dioxide). The voltage applied on the electrode gates, deposited on top of the silicon dioxide, controls the behavior of the carriers in the Si substrate. A CCD in which photons are incident on the front surface of the device is called a front-illuminated CCD.

If photons with energies higher than the band gap energy of Si (1.1 eV) are incident on a CCD, electron-hole pairs are generated in Si. Since the gates are positively biased compared to the rest of the device, the photoelectrons get trapped in the potential well below the insulator layer in each pixel (Fig. 2.10). The charges stored in each pixel will be transferred from one pixel to another pixel by changing the voltage applied to the gates. Front-illuminated CCDs have low quantum efficiency (QE) due to the attenuation of the incoming light while passing through the gate structures. High performance CCDs with QE near 100% are back-illuminated CCDs. In the latter design, the light attenuation from the gate structures is minimized by placing the gates at the back (Fig. 2.10). The excess Si on the bottom of the device is etched away for better photoelectron generation.

All CCDs operate at low temperature to reduce the dark current which is caused by thermally generated electrons. They are mostly cooled by liquid nitrogen (LN_2) or thermoelectric coolers.

Diffraction Grating

Focusing Mirror

Diffraction Turret

Exit Slit

CCD Camera
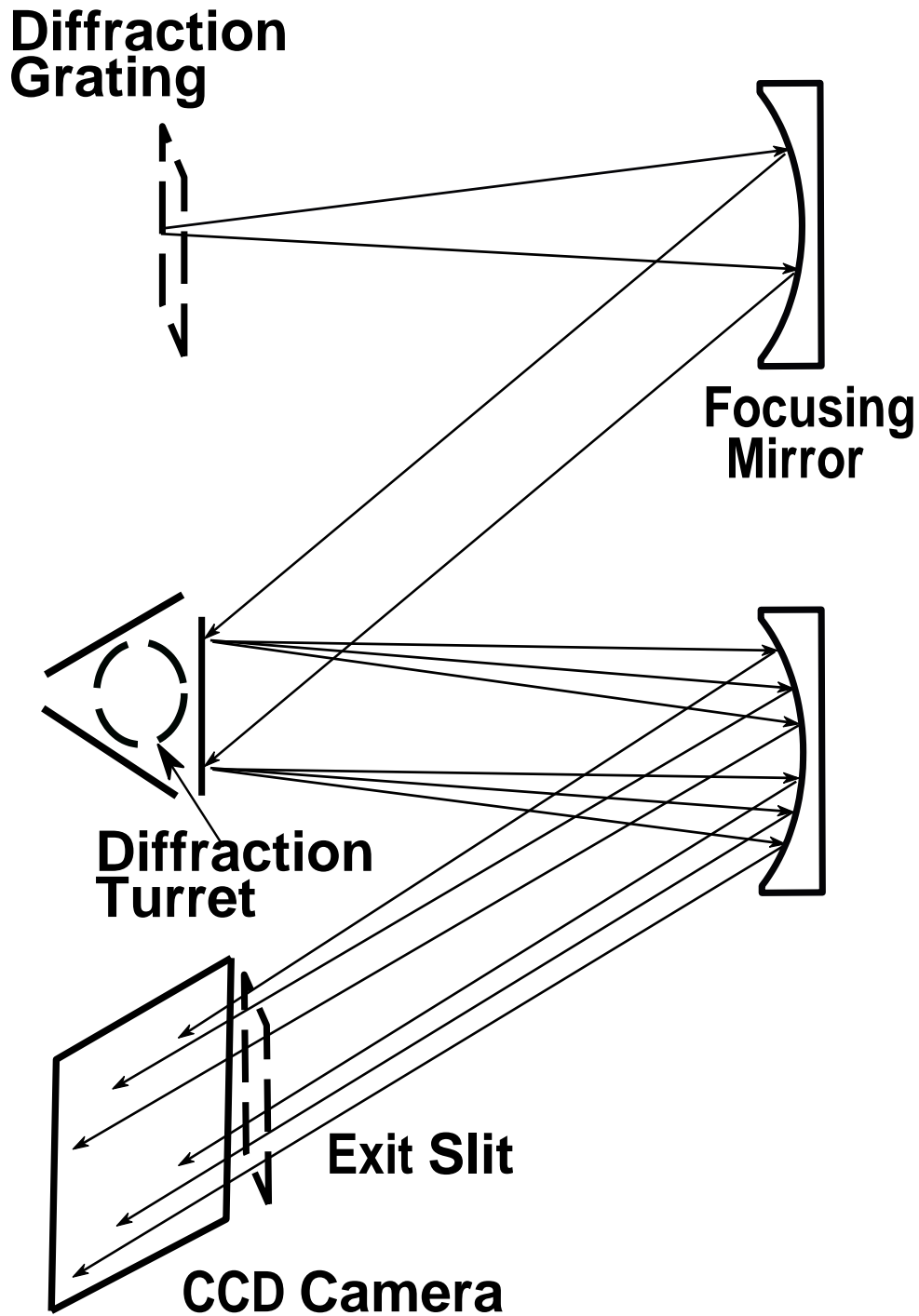
Figure 2.8: Schematic illustration of iHR550 spectrometer using Czeny-Turner configuration.

Typical Spectral Response
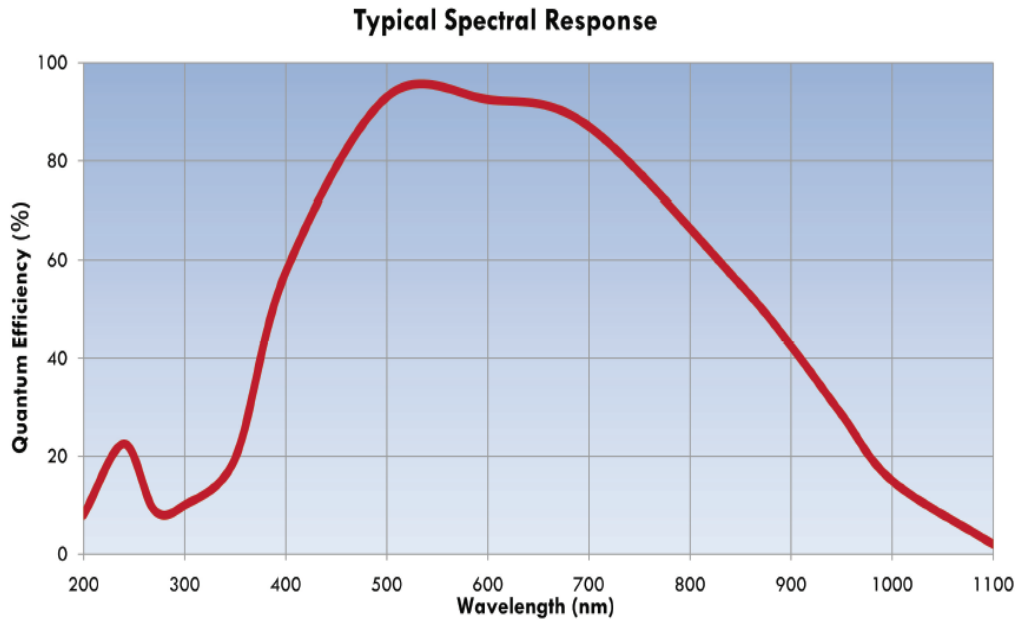
Figure 2 .9: Typical spectral response of the Symphony back illuminated CCD detector. Adapted from [86].
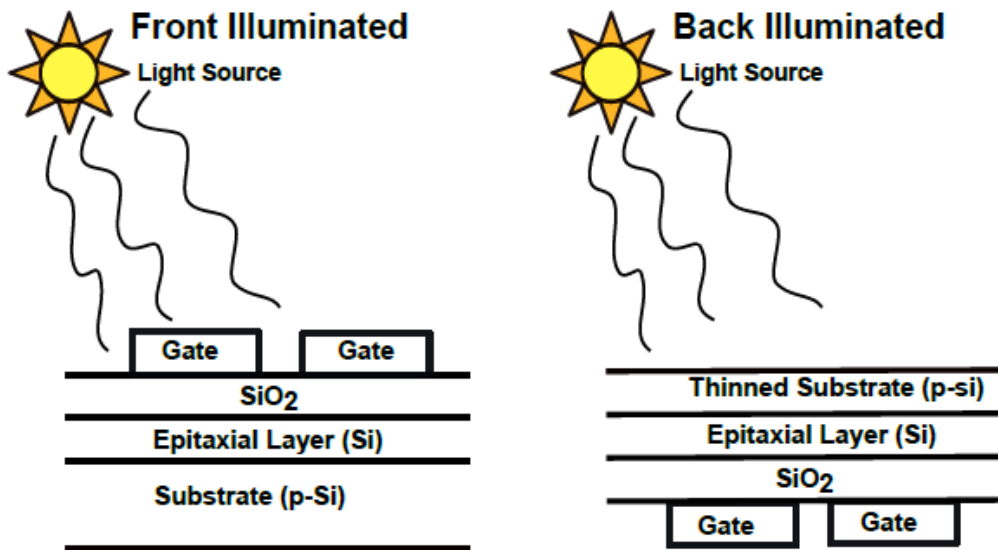
Figure 2.10: A schematic illustration of back illuminated CCD.

2.3 Characterization by Scanning Electron Microscopy

Scanning electron microscopy (SEM) is a powerful instrument for material analysis. High spatial resolution, diversity in imaging modes, straightforward sample preparation and image interpretation as well as high levels of automation bring SEM into the list of popular characterization techniques [89, 90]. SEM has been extensively used in the research of NWs for determination of morphology, orientation, and chemical composition. The reported images and information about the morphology of the NWs in this thesis was yielded using a JEOL JSM-7000F equipped with field-emission gun filament for electron beam generation.

The resolution of optical microscopes is limited by the wavelength of light and reaches a limit of 200 nm which is not appropriate for nanoscale imaging. Electrons have much shorter wavelength than photons and can be deflected by magnetic fields. The de Broglie wavelength of an electron with momentum p is:

$$\lambda = h/p \qquad\qquad (2.1)$$

According to this equation, the wavelength of an electron with energy of 1 keV would be around 1 nm. SEM systems produce electron beams using different electron guns such as tungsten hairpin, lanthanum hexaboride (LaB_6) cathode or field emission depending on the needed reliability, cost, magnification, and brightness. The primary electron (PE) beam should be stable, with small spot size, adjustable energy and small

energy dispersion. High resolution imaging can be achieved by focusing the PE beam using magnetic lenses. The sample surface is scanned by a focused beam in a raster pattern and a large number of signals are produced due to the interaction of the beam and specimen. The interaction volume is controlled by the energy of the PE beam. The PEs can be scattered during the elastic interaction with specimen atoms. The scattered electrons are called backscattered electrons (BSEs) which have energies close to the PEs. Both PEs and BSEs can excite atoms in the sample and generate signals at various depths of the sample as shown in Fig. 2.11. The PE beam energy can be varied in the range of 1-30 keV and is kept low for surface analysis. Inelastic scattering of PEs and/or BSEs can generate secondary electrons (SEs). Signals generated by SEs possess energies less than 50 eV and are very useful for surface topographical analysis. The standard collector for SEs is called Everhart-Thornley (ET) detector. The penetration depth of the PEs increases using high accelerating voltage and causes the loss of detailed surface information. BSEs have energy greater than 50 eV and their generation in a sample depends strongly on the atomic number. The BSE yield is higher for high atomic number elements. Both SEs and BSEs can be used for imaging, but the lateral resolution of SEs (10 nm) is much better than BSEs (1 μm). Increasing the accelerating voltage results in smaller probe diameter, lower lens aberration, and thus higher image resolution. The charging of non-conductive and beam sensitive samples such as NWs increases at higher accelerating voltage. The voltage applied for NW imaging was in the range of 2 to 3 kV. The probe current and aberration decrease by using smaller objective aperture diameter resulting in better

resolution. The convergence angle of the beam also reduces which increases the depth of focus. All the NW images were obtained using an aperture with 50 μm diameter.
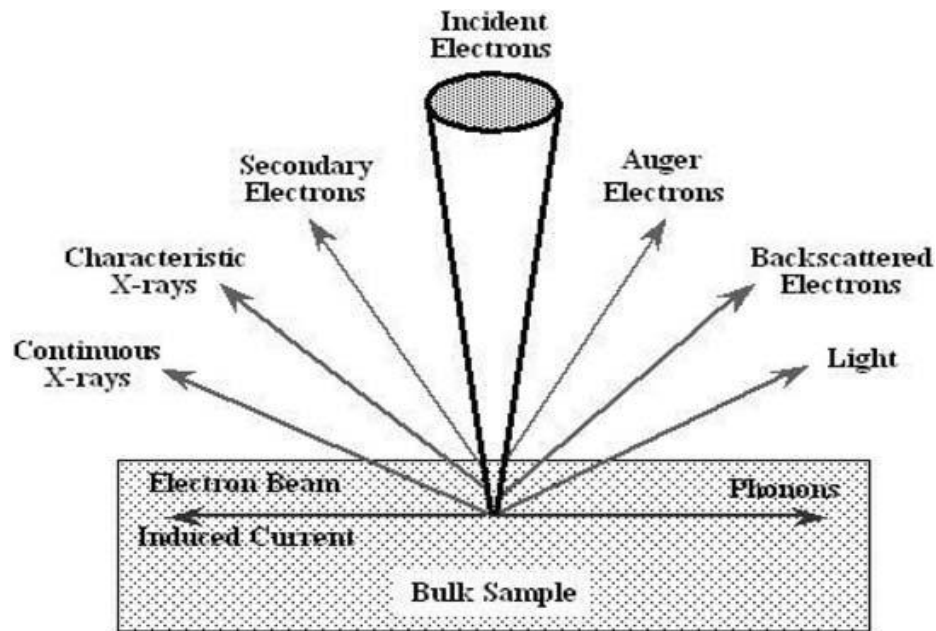
Figure 2.11: Schematic illustration of the signals generated inside a SEM when an electron beam interacts with a sample. Adapted from [89].

The distance between the tip of the objective lens and the surface of the sample is called the working distance (WD). Using short WD causes a reduction in the probe size and lens aberration, while it increases the imaging resolution and decreases the depth of focus. An optimum WD for NW imaging was experimentally found to be between 4 to 6 mm.

Contamination of the sample can stem from the interaction of the PE beam with residual gases and hydrocarbons on the sample surface. In the current study, the contamination is reduced by using the cold finger in

the column of the SEM, decreasing the probe current, and performing the alignment on the areas of the sample away from the imaging area. The specimen preparation is also performed in a manner to minimize the hydrocarbon contamination. The substrate is cleaned with acetone, methanol and running DI water. A fresh solution is always made when sonicating a piece of as-grown sample in methanol. After dispersing the NWs by micro-pipet on the substrate, usually the sample is placed under running DI-water and dried by N_2. To load the specimen into the SEM, the specimen is adhered to an Al-based stub using double sided carbon tape. Flat stubs for planar imaging and angled stubs (45 degree) for cross-sectional imaging were used. To prevent charging effects, there should be a ground path to conduct the charges captured on the sample surface to the Al-stub; otherwise the accumulating charges on the surface cause distortion in the image. A conductive silver paste was used to connect the top surface of the sample to the stub underneath.

Chapter 3

p-InP Nanowire Passivation

3.1 Introduction

The continuous scaling of electronic and optoelectronic devices has been accompanied by an increasing influence of surfaces and interfaces on the device performance. The surfaces of most III-V semiconductors contain a high density of surface states within the band gap causing Fermi level pinning. Fermi level pinning detrimentally affects the performance of semiconductor devices by creating Schottky metal contacts, carrier depletion, and electron-hole recombination at the surface states. In nanostructures such as nanoparticles or NWs, the effect of Fermi level pinning can be more significant due to the inherently large surface area to volume ratio. To reduce the detrimental effects of surface states on the optical and electrical properties of semiconductors, surface passivation can be applied to reduce the density of surface states.

III-V semiconductor NWs are one of the most promising nanostructures for next generation sensors, photovoltaics, photodetectors, and light sources [91]. However, the realization of these devices will require effective surface

passivation. Chemical passivation or the encapsulation of NWs in passivating shells has been successful in reducing the surface trap density [59, 60, 61, 63, 80, 92, 93]. For example, AlGaAs shells have been recently shown to reduce the surface trap density in GaAs NWs [59, 60]. Sulfur passivation is one of the most investigated methods for passivation of III-V semiconductor surfaces, although only a few reports can be found on sulfur passivation of NWs [60, 62, 80, 92, 93]. A review of sulfur passivation of planar surfaces is available in [28]. In the case of planar InP surfaces, sulfur passivation results in removal of the native oxide layer and the formation primarily of In-S bonds which reduces the density of midgap surface states [28]. Sulfur passivation of an InP (100) surface resulted in a two order of magnitude reduction in trap density to $7x10^9$ cm^{-2} [94]. Due to the removal of non-radiative recombination at the surface, the photoluminescence (PL) intensity of an InP (100) surface at 77 K was quadrupled after passivation in an aqueous solution of ammonium sulfide [95].

In the present study, sulfur passivation of individual InP NWs was studied using micro-PL. Similar to the prior studies on planar surfaces, changes in the peak PL intensity were used as a method of investigating and optimizing the sulfur passivation procedure. A simple model is presented to explain the PL improvements in terms of a reduction in surface trap density.

3.2 Experimental Details

InP NWs were grown by the Au-assisted VLS process in a GS-MBE system. S-doped InP (111)B (1-4 × 10^{18} cm^{-3}) wafers were treated by UV-ozone oxidation for 20 minutes to remove any hydrocarbon contamination and to grow a sacrificial oxide. The wafers were then dipped in buffered HF for 30 s and rinsed under flowing deionised water for 10 min. The wafers were dried with N_2 and transferred to an e-beam evaporator where a 1 nm thick Au film was deposited at a rate of 0.1 nm/s as measured by a quartz crystal thickness monitor. The wafers were then transferred to a GS-MBE system (SVT Associates). In the GS-MBE system, In was supplied as monomers from an effusion cell, and phosphorus was supplied as P_2 dimers that are cracked from PH_3 in a gas cracker operating at 950 °C. Prior to growth, the wafers were placed in a pre-deposition chamber where they were degassed for 15 min at 250 °C. After transferring the wafers to the growth chamber, an oxide desorption step was performed where they were heated to 485 °C under inductively coupled hydrogen plasma and P_2 overpressure for 10 min, leading to the formation of Au nanoparticles. The sample was cooled to the growth temperature of 400 °C and NW growth was initiated by opening the In shutter. The V/III flux ratio was 2.8, 2-D equivalent impingement rate of In was 1 µm/hr, and growth duration was 30 min. The NWs were doped p-type with Be from an effusion cell at a nominal level of 5×10^{18} cm^{-3}, as determined by doping calibrations performed on 2-D InP epilayers on (100) InP substrates.

After growth, the NW morphology and density were determined by a JEOL 7000F field emission SEM. The InP NWs were 1.3 – 1.8 μm in length. The NW diameter varied from 60 to 100 nm with a typical value of 70 nm as measured by SEM in Fig. 3.1. The NWs were uniform in diameter with no visible tapering.

The NWs were removed from the growth substrate for room temperature μ-PL investigations by sonication in acetone for 30 s followed by random dispersion onto a silicon substrate covered by thermally grown 300 nm thick silicon dioxide. PL was measured from individual NWs using a ×60 objective with NA 0.70. A He-Ne laser (λ=632.8 nm) was used as the excitation source with irradiance of 320 W/cm^2 and spot size of 2 μm. Spectra were collected by a 0.55m Horiba Jobin Yvon spectrometer and dispersed on to a LN$_2$ cooled Si CCD detector.
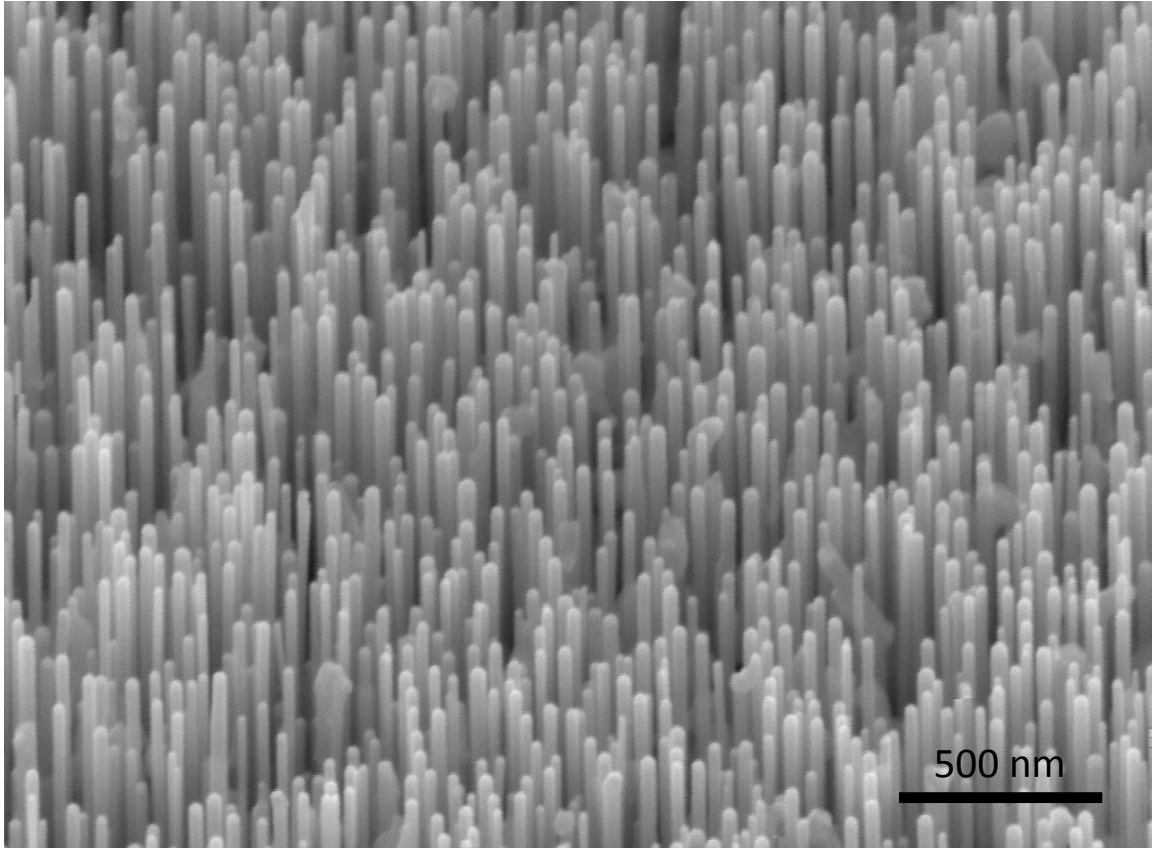
Figure 3.1: SEM image of as-grown InP nanowires.

Single NWs were located using a microscope such that PL could be obtained from identical NWs before and after the passivation procedure described below. The PL intensity was greatest when the incident polarization was aligned parallel to the NW axis as described previously [96]. Therefore, all PL spectra were acquired using the latter polarization arrangement.

Passivation was performed by soaking the NWs dispersed on the Si/SiO$_2$ substrate in 5 ml of ammonium polysulfide solution, $(NH_4)_2S_x$, on a hotplate at 62

˚C. The duration of the passivation was varied from 5 to 60 min. The base chemical used for passivation was 20 wt.% $(NH_4)_2S$ in H_2O obtained from Sigma-Aldrich. This base chemical was modified for the passivation procedure by the addition of elemental sulfur followed by dilution in various solvents as described in the section 3.3. Passivation was performed in an inert N_2 glovebox environment with less than 1 ppm of O_2 and H_2O. The passivation procedure requires illumination [28], which was provided by white light from a 30 W fiber optic illuminator. The PL measurements were performed immediately after passivation, and no change in PL intensity was observed during the measurement period of less than one hour.

3.3   Results and Discussion

The passivation procedure was optimized by measuring changes in peak PL intensity upon passivation as shown, for example, in Fig. 3.2. Due to removal of non-radiative surface recombination, the PL intensity of NWs improved after passivation similar to planar surfaces [95]. In all cases, the peak PL intensity occurred near 1.46 eV (850 nm), which is greater than the bulk bandgap energy expected for zincblende (Zb) InP (1.35 eV). While bulk InP has the Zb crystal structure, investigations of the InP NWs by transmission electron microscopy (not shown) revealed a wurtzite (Wz) crystal structure. The Wz structure is commonly observed in NWs due to their large surface area to volume ratio [97].
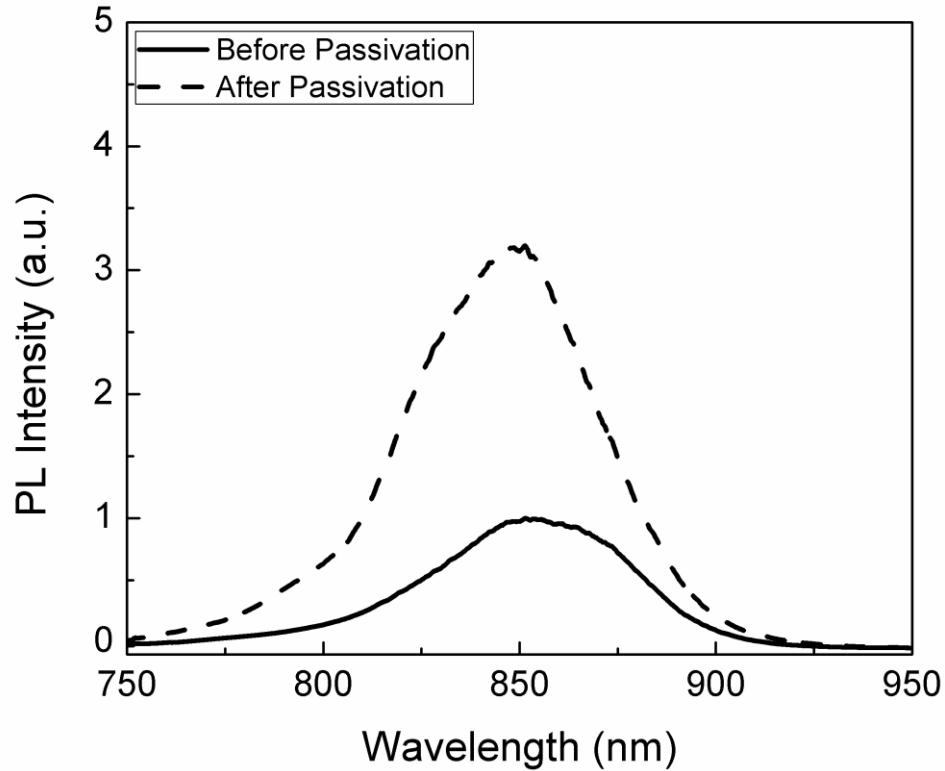
Figure 3.2: Representative room temperature μ-PL spectra (arbitrary units, a.u.) of an InP NW before passivation (solid line) and after passivation (dashed line). NW passivation was performed using 0.25M IPA-diluted solution.

Previous studies have established that the Wz structure of InP NWs results in a bandgap of ~1.45 − 1.5 eV [98-106]. Hence, the relatively large peak PL energy in our InP NWs as compared to bulk InP can be explained as a band-related recombination in Wz. Note that the large diameter of the NWs (60-80 nm) means that quantum confinement effects are not expected to contribute any blue-shift of the NW PL.

Besides the increase in peak PL intensity that occurred upon passivation, a small blue-shift of 32 meV in the room temperature peak PL energy was also observed upon passivation as seen in Fig.3.2. We assume this blue-shift is due to the Franz-Keldysh effect [107, 108] due to a reduction of the built-in surface electric field upon passivation as observed previously in p-InP nanowires [109].

The as-received $(NH_4)_2S_x$ solution was modified by the addition of elemental sulfur to produce 4, 5 and 10M stock solutions. First, the effect of solvent type on the passivation was investigated by dilution of the 5M solution to 0.25M by the addition of a solvent. Three different solvents were investigated: deionized water (DI), methanol, and isopropyl alcohol (IPA). Passivation of the NWs was performed in the 0.25M $(NH_4)_2S_x$ solution for 5 min. Figure 3.3 plots the ratio of the peak PL intensity after passivation compared to that before passivation for each type of solvent. In each case, the average peak PL intensity ratio in Fig. 3.3 was obtained over at least 10 NWs with the error bars representing the standard deviation. For the purposes of the investigations in Fig. 3.3, we used NWs of similar length (~1 μm) and diameter (70 nm) in all cases. The diameter dependence of the PL is presented later.

After treating the NWs in DI solution, the peak PL intensity (Fig. 3.3a) was typically unchanged or slightly reduced compared to that before passivation. Hence, there was no effective surface passivation of the NWs when using DI water as a solvent. Similarly, in methanol-diluted solution, the PL intensity (Fig. 3.3b) improved only slightly and in most cases exhibited no change after

passivation. Finally, passivation with IPA-diluted solution showed an increase in PL intensity (Fig. 3.3c) after passivation for nearly all NWs. Previous studies on planar (100) GaAs surfaces have shown that solvents with a lower dielectric constant can improve the sulfur passivation, and hence the PL intensity, due to charge screening effects [34]. DI water, methanol and IPA have a dielectric constant of 80, 33 and 18, respectively. Thus, the results on InP NWs are consistent with the prior studies on GaAs substrates, and IPA was chosen as the solvent for all further studies.

Next, the effect of elemental sulfur concentration on the NW passivation was examined by dilution of the previously prepared stock solutions to 0.4, 0.5 and 1M using IPA as solvent. An improvement in peak PL intensity can be observed in Fig. 3.3 upon increasing the sulfur concentration from 0.25M to 0.4M and 0.5M (Fig. 3.3c, d and e, respectively), followed by a decline at 1M (Fig. 3.3f). The decline in PL intensity for concentrations above 0.5M is attributed to etching of the NW surface as discussed below.
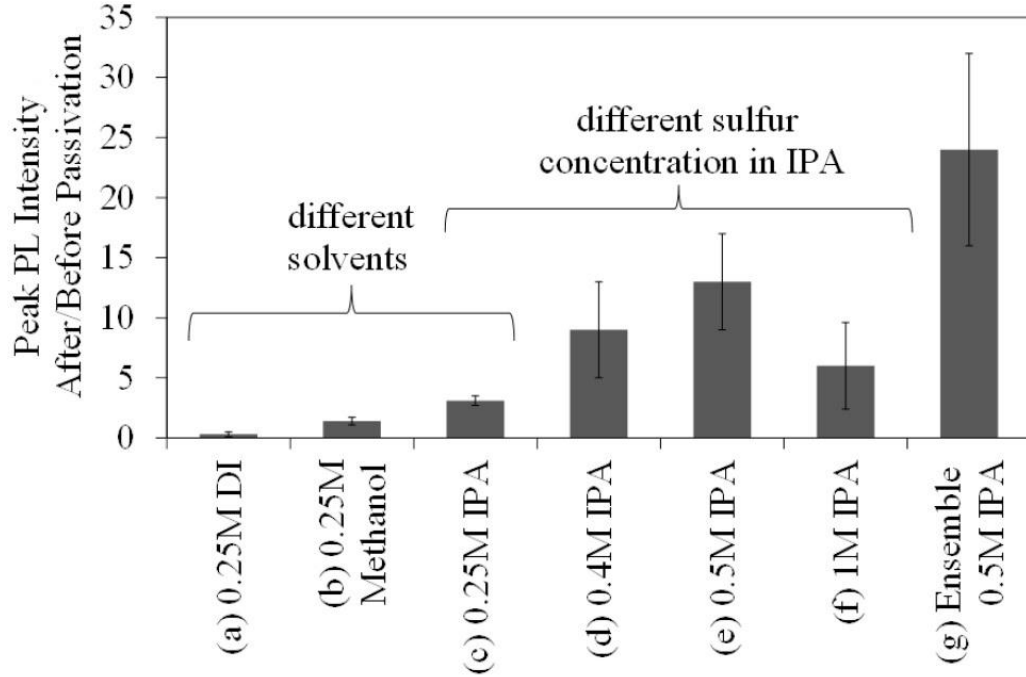
Figure 3.3: Ratio of peak PL intensity after passivation to that before passivation for different passivation methods: 0.25M sulfur concentration diluted in (a) DI water, (b) methanol, or (c) IPA; IPA solvent with different S concentrations of (c) 0.25M, (d) 0.4M, (e) 0.5M, or (f) 1M; (g) passivation of vertically oriented, as-grown, ensemble NWs in 0.5M IPA-diluted solution. NWs in (a-f) were passivated in a horizontal orientation after transferal to a host substrate. Error bars indicate the standard deviation. The NW diameter was 70 nm in all cases.

The $(NH_4)_2S_x$ solution etches the InP native oxide and allows covalent bonding of sulfur to P and (predominantly) In surface atoms for passivation of surface states. However, the $(NH_4)_2S_x$ solution also etches the InP material for long passivation durations. This etching was verified by observing individual NWs before and after passivation using SEM. In this experiment, passivation was performed using the IPA-diluted 0.5M $(NH_4)_2S_x$ solution.

As shown in Fig. 3.4, the surface of NWs became visibly rougher with increasing duration in the passivation solution. The etching of the NW surface was just visible for etch durations as small as 5 min (Fig. 3.4a) in the 0.5M IPA solution. Nanowires etched between 15 and 60 minutes were completely etched, leaving only some InP "residue" on the host substrate. Naturally, the decreased volume of the etched NW will result in a decline of the PL intensity. In addition, the increased roughness of the NW surface due to etching may increase the surface state density and/or reduce the ability of sulfur to passivate the surface, thus reducing the PL intensity ratio.

(a)   (b)   (c)   (d)   (e)   (f)
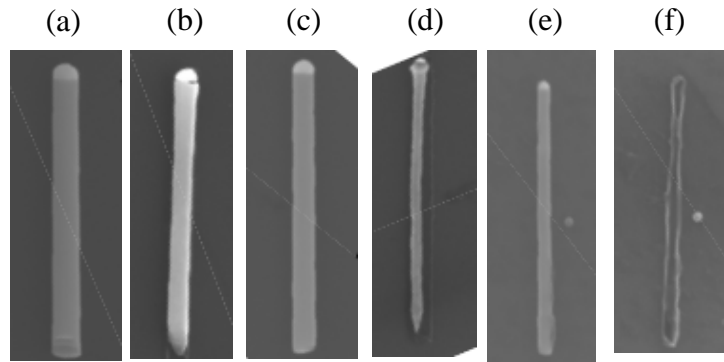
Figure 3.4: SEM image of p-InP NWs on host substrate before passivation (a, c, e) and after passivation (b, d, f) using IPA-diluted 0.5M solution. Duration of the passivation was (b) 5 min, (d) 15 min, or (f) 60 min. The identical NW was imaged in the pairs (a, b), (c, d) and (e, f). In (f), only an InP "residue" remained on the host substrate.

As a final investigation, we examined an alternative passivation procedure in which the vertically oriented NWs of the as-grown sample were first passivated using the IPA-diluted 0.5M solution before transferal to a host substrate. After

passivation, the NWs were transferred to the host SiO_2/Si substrate for PL measurements, and compared to similar measurements of unpassivated NWs. Using this method, the PL intensity of the passivated NWs increased by up to a factor of 40 (average of 24; see Fig. 3.3g) as compared to unpassivated NWs. The latter improvement was nearly twice that achieved previously in Fig. 3.3d when the passivation procedure was implemented on the post-transferred, horizontally oriented NWs. The passivation procedure may have been less effective for the horizontal NWs due to hindrance of the sulfur bonding to the region of the NW in direct contact with the SiO_2/Si substrate, as well as a lack of direct light illumination on the rear side of the NW which is needed for effective passivation.

The stability of the sulfur passivation was investigated by measuring the PL intensity from an individual NW (of 93 nm diameter) immediately after passivation and after a specified duration of exposure to ambient air. No changes in PL intensity were observed during the PL acquisition. As shown in Fig. 3.5, the PL intensity decayed to its initial pre-passivation value after 7 days in ambient, indicating that the sulfur passivation is not stable against oxidation in air. Similar stability was previously measured for GaAs nanowires [80]. However, the stability of the sulfur passivation can be improved by encapsulation in polymer or dielectrics [67, 110, 111].
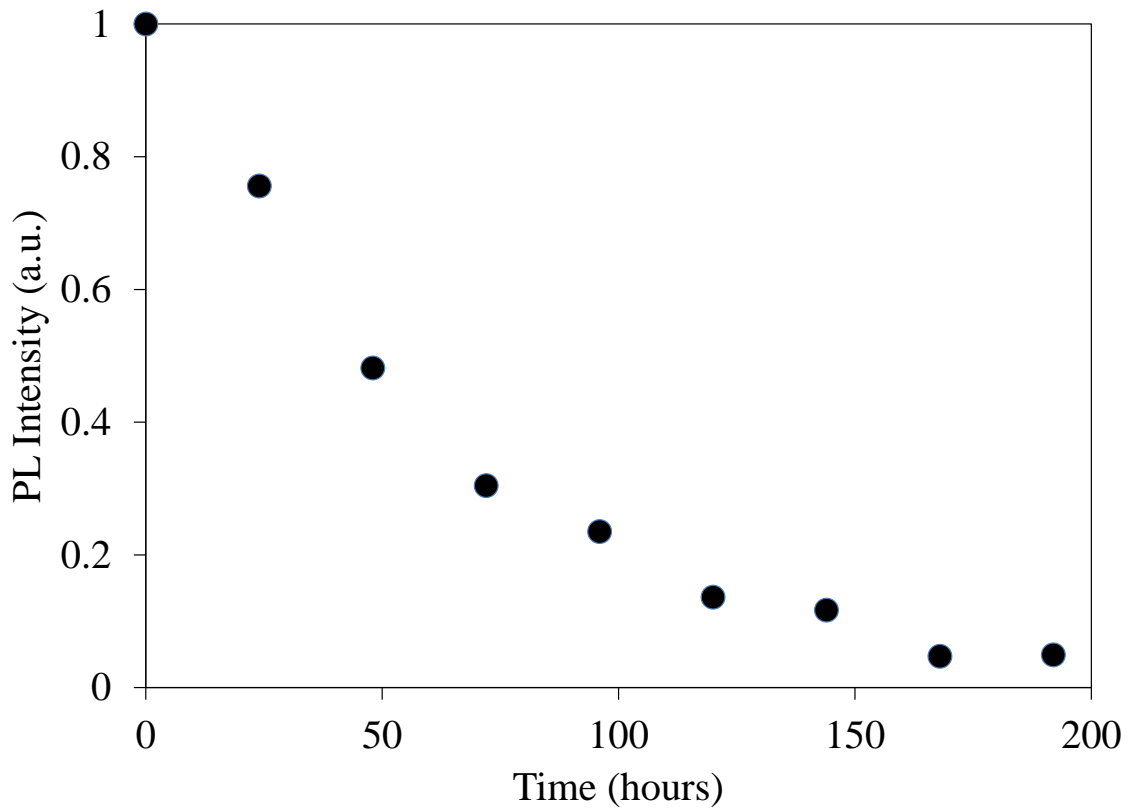
Figure 3.5: PL intensity from an individual nanowire after specified time in ambient air. The PL intensity at each time was normalized to the PL intensity obtained immediately after passivation (at t=0).

3.4 Photoluminescence Dependence on Excitation Polarization, Excitation Intensity and Nanowire Diameter

3.4.1 Polarization Dependence

Optical absorption and emission in semiconductor NWs strongly depend on the polarization of the exciting light. This anisotropy is attributed to the crystal structure, dielectric contrast between NWs and surrounding environment and quantum confinement effects. In the case of the NWs in this study, the exciton Bohr radius of InP NW (9 nm) is much smaller than the diameter of the NWs (70 nm), so the quantization plays no role in the observed polarization effects. If the NW is considered as an isotropic cylinder with diameter (70 nm) much shorter than the wavelength of the incident light (632.8 nm), the polarization effects can be explained by the classical electrodynamic theory. If the incident electric field is parallel to the axis of the NW, the transmitted field remains the same ($E_\parallel = E_{\parallel 0}$), while for the electric field perpendicular to the axis, the transmitted light is reduced by a factor of $2/\{\epsilon + 1\}$, where ϵ is the dielectric constant of the NW cylinder relative to surrounding environment (ϵ_{NW}/ϵ_0) [112, 113]. Since most of the semiconductors have dielectric constant higher than 10, optical measurements performed in air cause a large dielectric contrast. Fig. 3.6 shows the PL intensity dependence on the polarization of the incident light for two perpendicular InP NWs. The electric field of the incident light is parallel to the axis of the NW1 and

perpendicular to the axis of the NW2. The PL intensity is maximum when the polarization of the excitation light is parallel to the NWs axis.
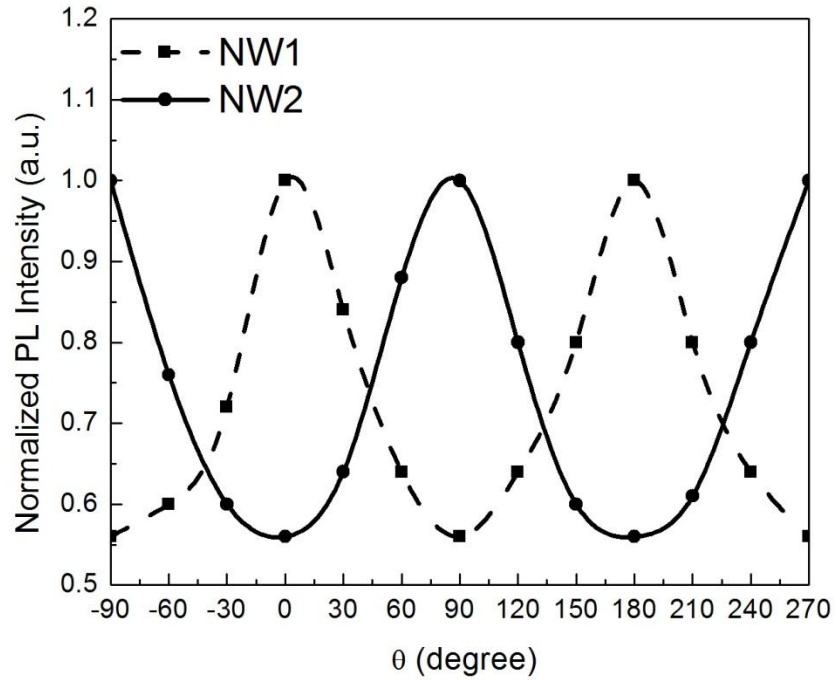
Figure 3.6: Polarization dependence of the PL from two orthogonal NWs.

3.4.2   Excitation Intensity Dependence

The excitation intensity controls the density of photogenerated carries in the NWs. Recombination regimes in the NWs can be affected by the photoexcited carrier density. Non-radiative Shockley-Read-Hall (SRH) recombination is a linear function of carrier density n. At low density of electron-hole concentration,

the non-radiative recombination is dominant. By increasing the excitation intensity, the radiative recombination becomes more important. The PL dependence on the excitation intensity can be used to investigate the effect of surface passivation on the reduction of surface states [114].

Power dependent CW spectra for a single p-InP NW, before and after passivation, are shown in Fig. 3.7a and Fig. 3.7b. Before passivation, there is a blue-shift in the PL peak for higher excitation power. After sulfur passivation, there is no blue-shift in the PL spectra upon changing the excitation power (Fig. 3.7b).

There is also a deviation from linearity in the relationship between PL and excitation intensity before passivation which is shown in Fig. 3.8a and Fig. 3.8b. The low temperature measurements at T=10K is shown to cover a wider range of power intensity. The nonlinearity, which mostly happens at intermediate excitation, is due to the existence of two different recombination regimes in NWs. At low excitation intensity, the density of photogenerated carriers are low and the recombination is mostly non-radiative and dominated by surface states and bulk impurity levels. In NWs, the surface-to-volume ratio is high so the effect of surface states plays an important role. At intermediate excitation intensity, most of the surface states are filled and bulk radiative recombination dominates, so the PL intensity increases rapidly. The linearity observed after passivation can be attributed to the reduction of the surface states after passivation and results in the reduction of non-radiative recombination.
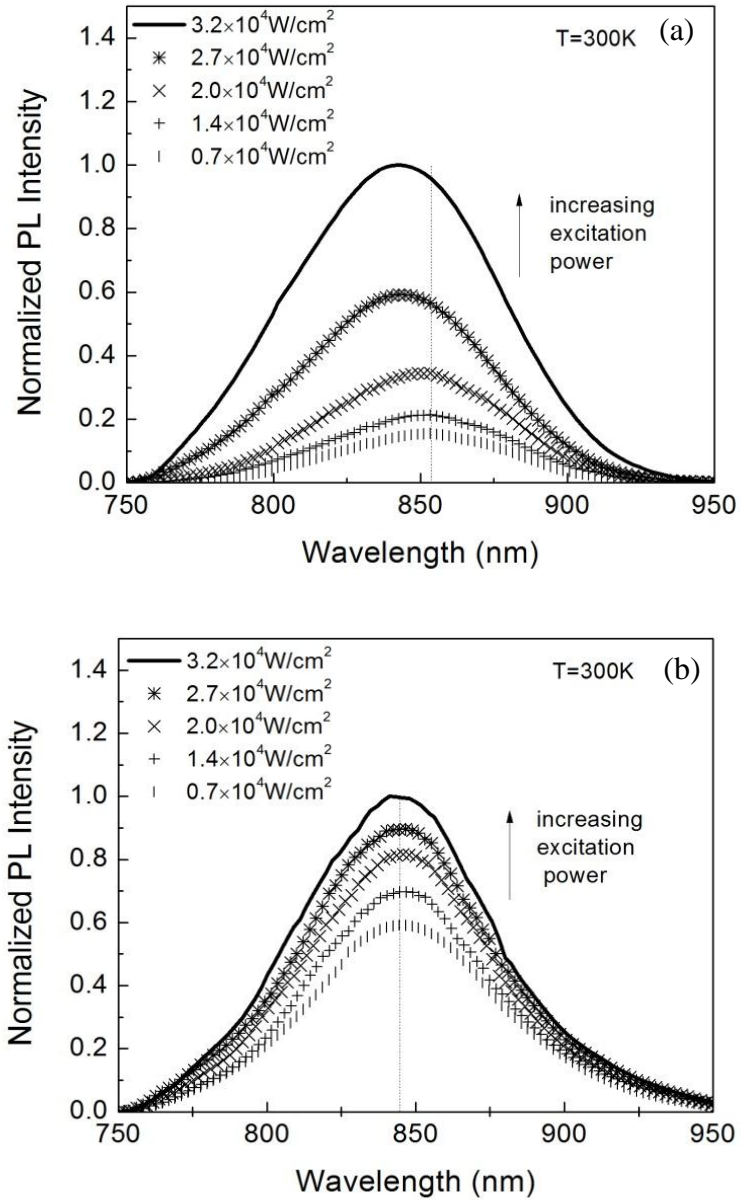
Figure 3.7: PL intensity and peak position dependence on excitation power (a) before passivation, and (b) after passivation in 0.5M $(NH_4)_2S_x$ solution diluted in IPA for 5 min at T = 300 K.
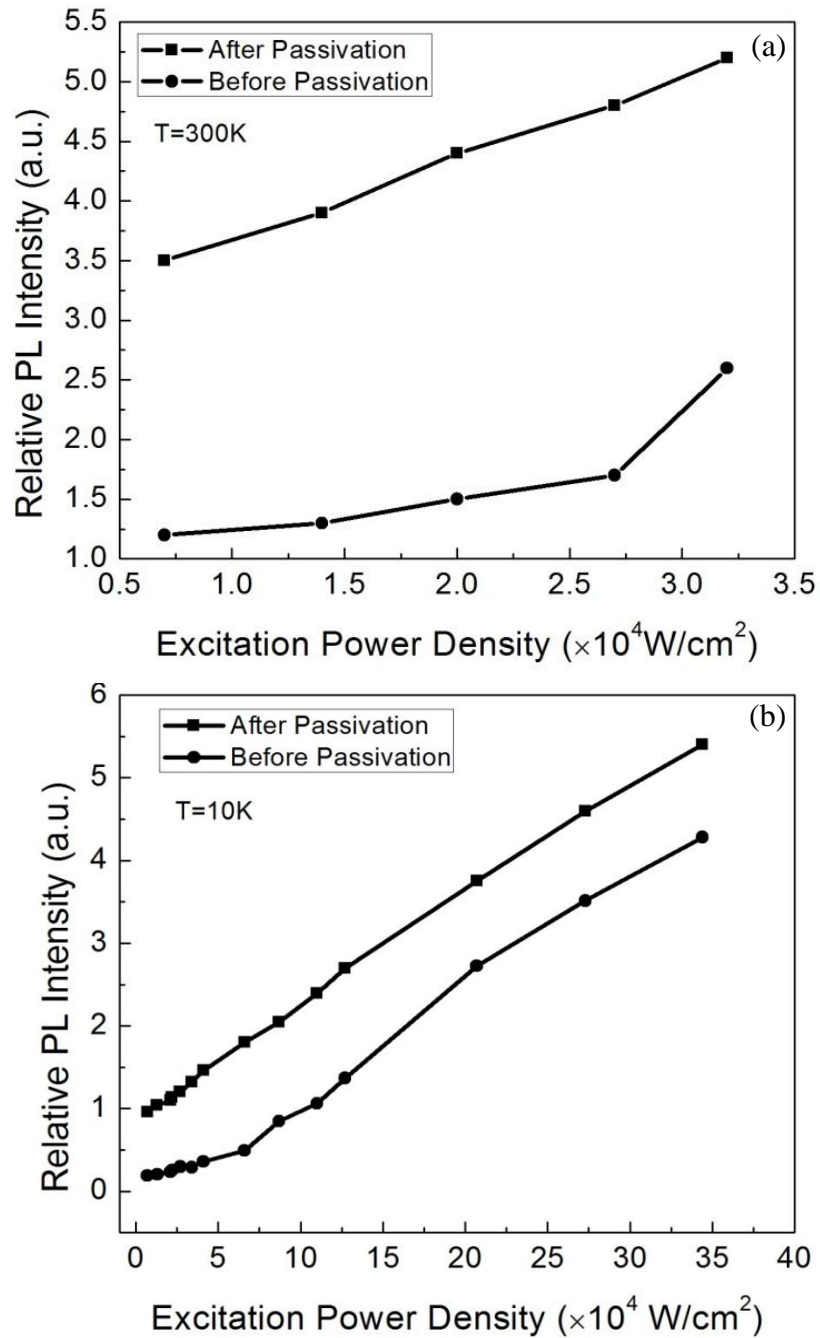
Figure 3.8: Comparison of the linearity between PL intensity and excitation power before and after passivation at a) T=300K, b) T=10K.

The observed blue-shift can be explained by band bending variations under different excitation intensities [109]. The band bending is a result of charge collection on the surface of the NW and causes electrons and holes to be spatially separated. Upon excitation the photogenerated electrons accumulate at the surface and holes at the center of the NW. Therefore the radiative recombination probability is small and the emitted photons have lower energy than the bandgap. By increasing the excitation power, more carriers are generated and thereby flatten the band and the PL energy increases (Fig. 3.9). So before passivation, we observe a blue-shift in the PL spectrum due to the band bending.
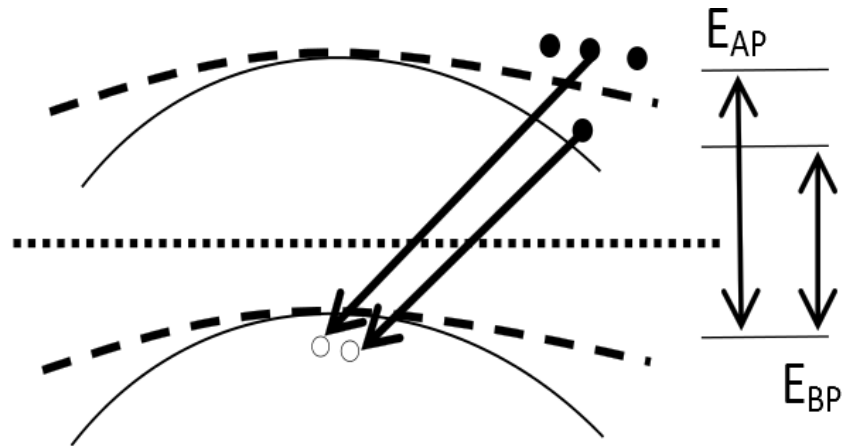
Figure 3.9: Band bending before passivation (solid line) and after passivation (dashed line) in p-InP NW.

3.4.3 Diameter Dependence

The PL intensity dependence of the NWs ranging from 60 to 100 nm before and after passivation has been investigated. The passivation procedure was performed using 0.5M of IPA-diluted solution for 5 min. The diameters and positions of the NWs on the SiO_2/Si substrate were measured by SEM. The measured PL was normalized to the length of the NWs. Fig. 3.10 shows that increasing the diameter of the NWs, improves the PL intensity as expected. For nearly the same density of surface states, the larger diameter NW has larger active region after the reduction of depletion region. The PL increases after passivation could be the result of the reduction in surface state density and/or depletion width of the NWs.
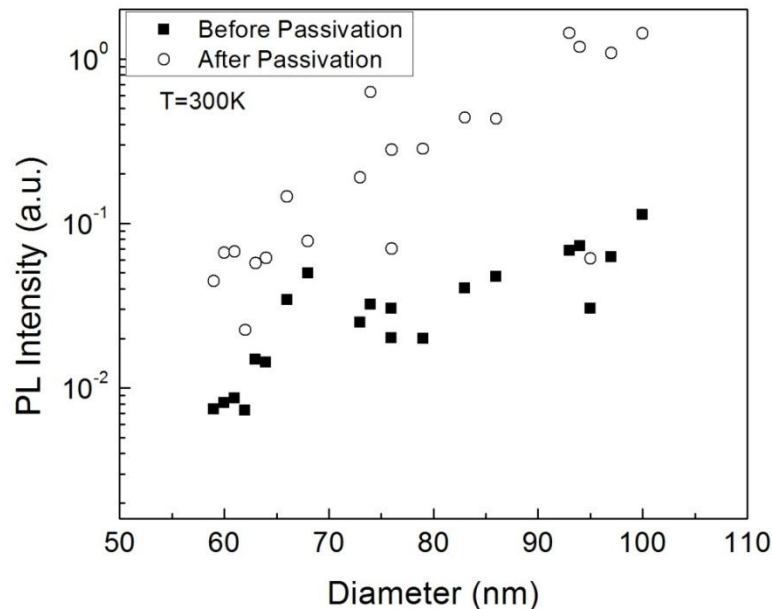
Figure 3.10: PL intensity before (squares) and after (circles) passivation vs. NW diameter.

3.5   Theoretical Calculation of Photoluminescence from Single Nanowire

The relative PL intensity from a single p-doped NW is given by [114]:

$$I_L = K \int_0^{R-w} \frac{\Delta n(r)}{\tau_n} dr \tag{3.1}$$

K is a constant factor which contains quantum efficiency and geometrical factors, R is the NW radius, w is the depletion width, Δn is the minority carrier concentration and τ_n is the lifetime of the minority carriers.

By assuming a NW as a cylinder with radius R and length L, Δn can be derived by numerically solving the three-dimensional, steady-state, small signal continuity Eq. 3.2 in cylindrical coordinates:

$$\nabla^2 (\Delta n) - \frac{\Delta n}{l_n^2} = \frac{(R_e - 1)N\alpha_e}{D_n} e^{-\alpha_e r} \tag{3.2}$$

N is the photon intensity, R_e is the reflectivity of the surface, l_n is the diffusion length of minority carriers, D_n is the diffusion coefficient of minority carriers and α_e is the absorption coefficient.

We assume that PL is only created in the bulk region $0 < r < R - w$ (dashed area in Fig. 3.11), where r is the radial distance from the centre of the NW and the recombination in the depleted area is neglected due to the low carrier concentration.
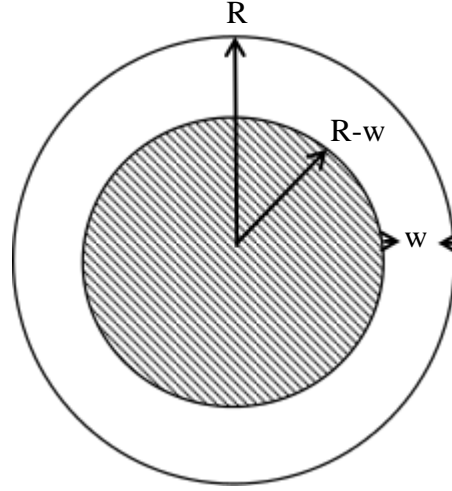
Figure 3.11: Cross section view of the NW. R is
the radius of the NW and w is the depletion width.

A boundary condition is needed for solving Eq. 3.2 to get the minority carrier concentration (Δn). We assume that at the interface between the bulk and field region, i.e. at $r = R - w$, the excess electron flux to the surface changes from diffusion to a field driven flux. The current continuity requirement is [115]:

$$q\, A\, (r = R - w)\, D_n \frac{d(\Delta n)}{dr}\bigg|_{r=R-w}$$

$$= A\,(R = r)\, J_s\,(r = R) - q \int_{R-w}^{R} A(r)[G(r) - R_{rec}(r)]dr$$

(3.3)

where A(r) is the surface area at the radial distance r from the center of the NW, J_s is surface recombination current density and R_{rec} and G are the recombination and generation rates, respectively, in the depleted area. According to the current

continuity requirement, the current passing through all the boundaries should be the same. At low injection conditions it can be assumed that G and R_{rec} are zero in the depleted region. If there is no generation and recombination of carriers in the depletion region, the current leaving the interface at $r = R - w$ should be equal to the current arriving at the surface at r = R, so Eq. 3.3 becomes:

$$q\ A\ (r = R - w)\ D_n \frac{d(\Delta n)}{dr}\bigg|_{r=R-w} = A\ (R = r)\ J_s\ (r = R) \tag{3.4}$$

or

$$A\ (r = R - w) J_{interface}(r = R - w)\ = A\ (R = r)\ J_s\ (r = R) \tag{3.5}$$

(J_s) at the surface of the NW can be defined as:

$$J_s(r = R) = qS\Delta n(r = R) \tag{3.6}$$

where S is the surface recombination velocity and $\Delta n(r = R)$ is the minority carrier concentration at the surface.

The same equation as Eq. 3.6 can be written for the interface at $r = R - w$:

$$J_{interface}(r = R - w) = qS_v\Delta n(r = R - w) \tag{3.7}$$

The quantity S_v is considered as a virtual surface recombination velocity at the interface between the bulk of the NW and depleted area [114]. The electrons, as minority carriers, flow at the boundary of bulk and depleted region at the speed of S_v and get recombined on the surface of the NW by true surface recombination velocity S. The carrier generation and recombination in the space charge region were neglected, so we can assume that the speed at which minority carriers

passing the boundary (S_v) is equal to S. What is usually measured in experiment is not S_v but S, that's why S_v is called virtual surface recombination velocity. Since the generation and recombination of minority carriers are assumed to be negligible in the depleted region, the current leaving the interface would be equal to current at the outer surface. So using Eq. 3.5, 3.6 and 3.7, the minority carrier concentration on the surface can be obtained from the minority carrier concentration at the interface:

$$\Delta n(r = R) = \Delta n(r = R - w)\left(\frac{R - w}{R}\right) \tag{3.8}$$

By replacing equations 3.8 and 3.6 in Eq. 3.4, the final boundary condition equation becomes:

$$q \ D_n \frac{d(\Delta n)}{dr}\Bigg|_{r=R-w} = qS\Delta n(r = R - w)\left(\frac{R - w}{R}\right) \tag{3.9}$$

Eq. 3.9 should be solved simultaneously with Poisson's equation given by:

$$\nabla^2 \phi = \frac{\rho}{\epsilon_s} \tag{3.10}$$

where ϕ is the surface potential, q is the elemental charge, ϵ_s is the permittivity of the semiconductor, and ρ is the charge density in the depletion region. The surface

potential and the electric field should be zero at the interface ($\phi (R - W) = 0$ and $\delta\phi(R - w)/\delta r = 0$).

Eq. 3.2 and 3.10 are solved numerically by assuming a constant reflection of the impinging light on the surface of the NW and neglecting light refraction in the NW. The typical value for InP used for calculations is shown in Table 3.1. The contour map of the PL intensity changes versus surface recombination velocity (S) and surface potential (ϕ) is plotted in Fig. 3.12.

Table. 3.1 Parameters used for simulation of PL intensity from p-InP NW

Physical quantity	Unit	Typical value
Photon flux density (N)	#/s-cm^2	10^{20}
Minority carrier diffusion constant (D_n)	cm^2/s	320
Minority carrier diffusion length (l_n)	cm	8×10^{-3}
Minority carrier life time (τ_n)	s	2×10^{-9}
Surface recombination velocity	cm/s	10^6
Reflectivity (R_e)		0.03
Absorption coefficient at 632.8 nm (α_e)	cm^{-1}	5.56×10^4
NW radius	cm	35×10^{-7}

According to Fig. 3.12, increasing the surface recombination velocity and surface potential results in the PL intensity reduction and the PL goes to zero when they reach up to 10^7 cm/s and 2.22 eV at room temperature, respectively.

If we take the typical values for S to be around 10^6 cm/s and surface potential around 0.5 eV for InP before passivation, a point will be found in the contour map called BP (before passivation). Fig. 3.13 shows that the change in the blue shift for the PL intensity peak after 40 times PL intensity increase, is around 32 meV. This value can be taken as a change in the surface potential on the contour map which happens after passivation. If we start from point BP and move to the left by 32 meV we'll cross a point AP which shows the new PL intensity and surface recombination velocity. By dividing the PL intensity from point AP over point BP, we get 40 which is consistent with the 40 times increase in the PL after passivation. The contour map shows that S reduces from 10^6 cm/s before passivation to 5×10^4 cm/s after passivation. A reduction in depletion width of around 4 nm also occurs.

If we use the assumption that $S = v_{th}\sigma N_t$, where N_t is the density of surface states, $v_{th} \cong 10^7\ cm/s$ is the carrier thermal velocity, and $\sigma = 10^{-13}\ cm^2$ is the capture cross section, then 40 times increase of the PL intensity in Fig. 3.13 implies a reduction of N_t from 10^{12} cm^{-2} to 5×10^{10} cm^{-2}, which corresponds to the surface velocity of 10^6 cm/s and 5×10^4 cm/s, respectively.
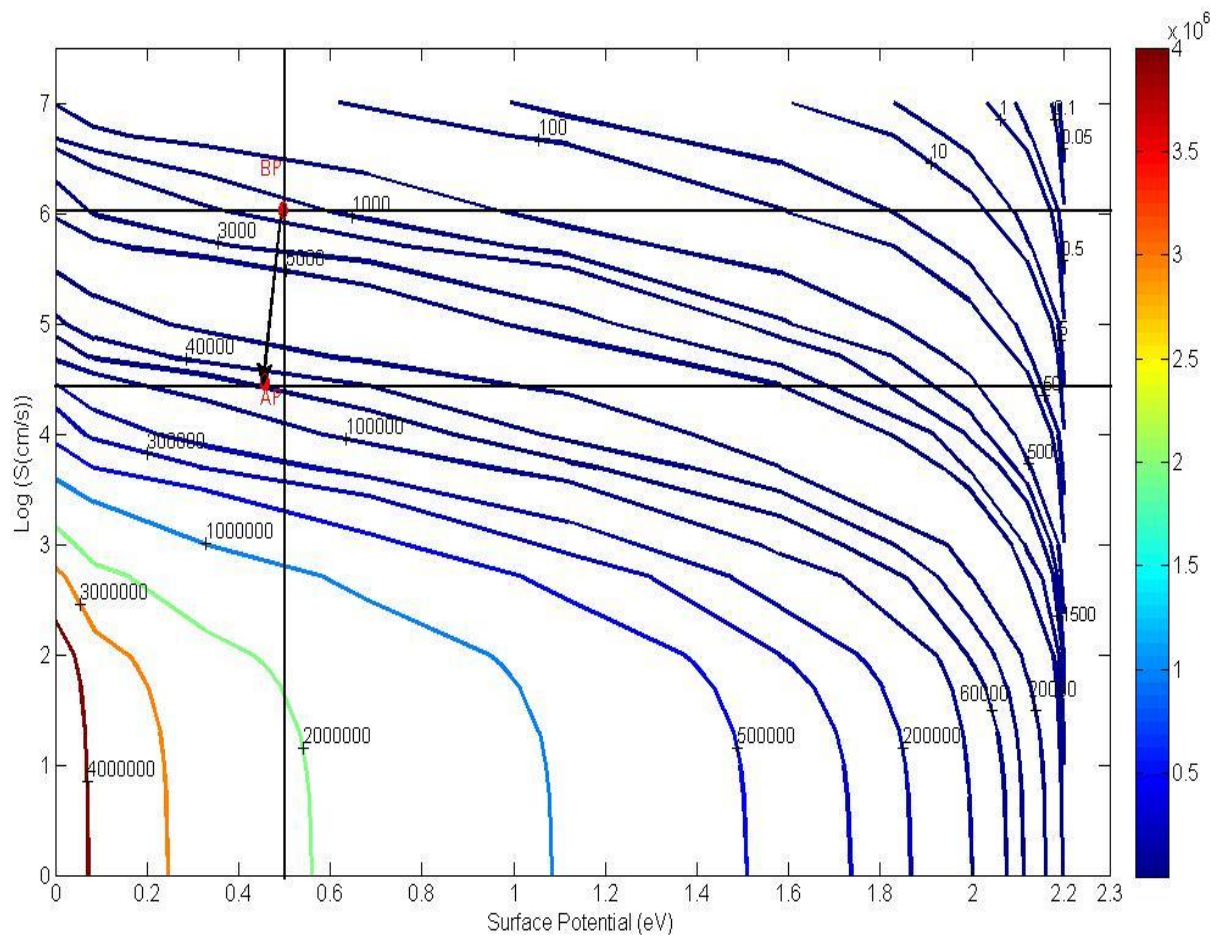
Figure 3.12: Contour map showing the PL intensity change versus log of surface recombination velocity (log(S)) and surface potential (φ). Each curve represents the constant PL intensity with the value labeled on the curve.
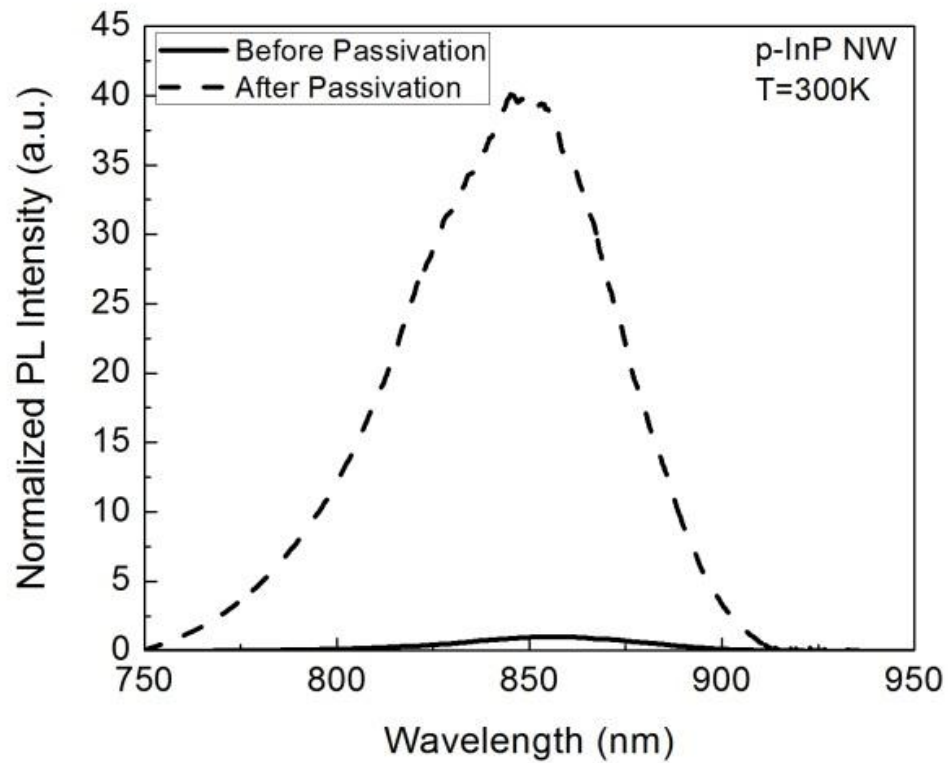
Figure 3.13: PL intensity of p-InP NWs after whole NW
surface passivation in 0.5M $(NH_4)_2S_x$ solution diluted in IPA.

3.6 Conclusions

Ammonium polysulfide solution $(NH_4)_2S_x$ was used to passivate the surface of p-InP NWs thereby improving their PL intensity. The optimization of the solution included adjusting the solvent type, the dilution level, and the passivation time to get the maximum PL intensity from the NWs. It was found that 0.5M solution diluted in IPA is optimum for passivation time around 5 min. The passivation was performed on both horizontal NWs dispersed from a sonicated sample onto the SiO_2/Si substrate and vertical NWs on an as-grown sample. The maximum PL increase was around 20 and 40 times obtained for horizontal and vertical NWs, respectively. The intensity dependence of the PL peak position was also investigated. The blue shift in the PL peak position before passivation was attributed to the high density of surface states decreasing after passivation. It can be concluded that the sulfur passivation reduces the surface state concentration. A PL model demonstrated the increase in PL intensity upon passivation as due to a reduction in surface trap density by two orders of magnitude from 10^{12} to 10^{10} cm^{-2}, corresponding to a change in surface recombination velocity from 10^6 to 10^4 cm/s. The passivation procedure and model described here can be used in further investigations to improve the performance of NW-based optoelectronic devices.

Chapter 4

Electrical Properties of GaAs NWs after Sulfur Passivation

4.1 Introduction

Contact quality is very influential in electron transport measurements through NWs and is mostly affected by surface states [116]. Sulfur passivation is shown to effectively reduce the surface barrier height of InP and GaAs [64, 117]. The effect of sulfur passivation on the electrical properties of individual InAs NWs was reported in Ref. [61] where the formation of ohmic contacts and increase of conductance was observed. PL increase upon passivation can be attributed to a decrease in depletion width around NWs and a reduction in surface recombination velocity and/or surface density of states. The improvement in electrical characteristics is attributed to the reduction in Schottky barrier height at the contacts and a decrease in NW resistance due to the decrease in depletion area [118].

4.2 Experimental Details

n-GaAs NWs were synthesized in a GS-MBE system. The NW growth was initiated by opening the Ga effusion cell shutter. Arsenic (As) was supplied as As_2 dimers from a gas cracker operating at $950\,^{\circ}C$. The growth temperature, V/III flux ratio, 2-D growth rate and growth duration were set to $600\,^{\circ}C$, 2.3, 0.5 µm/h, and 30 min, respectively. Te from a GaTe effusion cell was used for n-type doping with concentrations of about 10^{18} cm^{-3}. The morphology of NWs was inspected using a JEOL JSM-7000F field emission SEM. According to SEM analysis, the length and diameter of the NWs were 1.2-2 µm and 50-60 nm, respectively. The effect of passivation was investigated by measuring the I-V curves on ensemble NWs using a Keithley 2400 source meter. The measurements were performed on the sample before passivation (process 1), after contact area passivation (process 2), and after whole NW passivation (process 3). SU8 was used for contact planarization and as a spacer layer between the top contact and the substrate. Process 1 (Fig. 4.1a) involved dispensing SU8 on a piece of as-grown sample using a syringe, where it was allowed to rest for 2 min to permeate the space between the NWs. Spin-coating was then initiated with a low speed of 500 rpm for 5 s and with acceleration of 300 rpm/s. Spinning continued at 3000 rpm for 60 s. Soft baking was performed on the sample at $90\,^{\circ}C$ for 4 min on a hotplate. After that, the sample was hard baked at $200\,^{\circ}C$ for 5 min. SU8 was removed from the tip of the NWs by reactive ion etching (RIE) for 3 min with an O_2 flow rate of 28 sccm, a power of 100 W, and chamber pressure of 350 mTorr (Fig. 4.2). The top

contact was formed by depositing 500 nm Ni, 1000 nm Ge, and 2000 nm Au, through a shadow mask containing dots with diameter of 800 µm, on top of the NWs by electron beam evaporation at room temperature. Each dot contained ~5.7×10^6 NWs. The back contact was formed in the same way as the top contact but with half of the thicknesses and without using the mask.

   Process 2 (Fig. 4.1b) was the same as process 1, except before top contact formation the sample was soaked in 0.5M ammonium polysulfide ((NH_4)$_2S_x$) solution diluted in IPA for 3 min to passivate the contact area. Details of the passivation solution optimization is discussed in Chapter 3. The only difference between process 3 (Fig.4.1c) and process 2 is that the passivation was performed on the whole surface of the NWs rather than just the contact area, by soaking the as-grown sample in passivation solution before spin coating of the SU8.

(a)

(b)

(c)
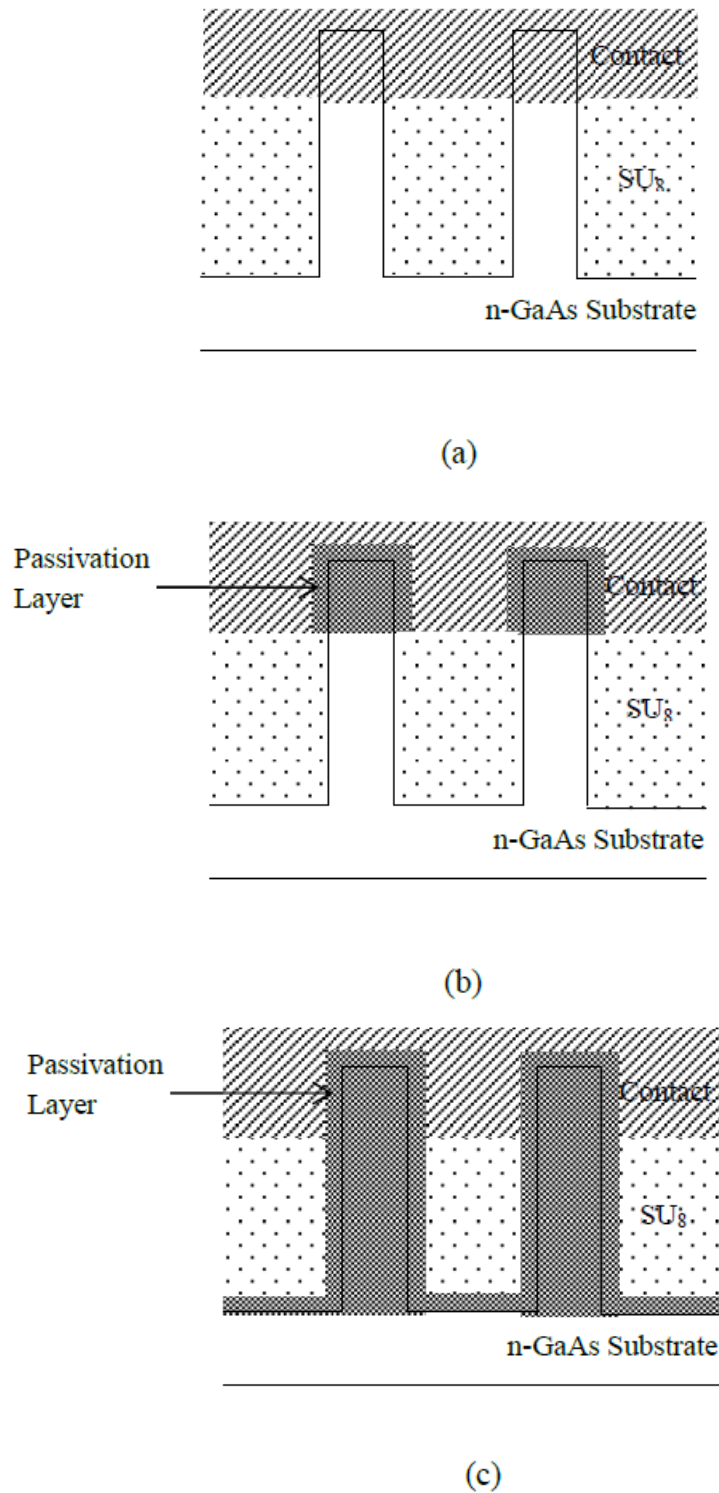
Figure 4.1: Schematic diagram of the processing applied on ensemble n-GaAs NWs to measure the effect of sulfur passivation: (a) process 1, (b) process 2, (c) process 3.
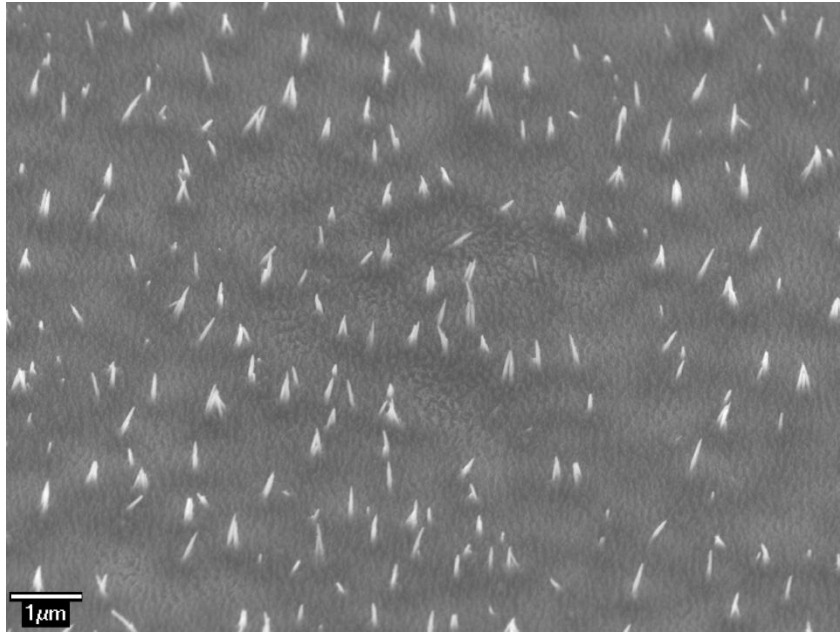
Figure 4.2: Tilted SEM view of sample after removing
SU8 by RIE and before contact deposition.

4.3 Results and Discussion

In this section, first the I-V characteristic of single NWs is modeled and shown

that the current flow through a single NW can be affected by the change in the

barrier height of the Schottky contacts and also the effective radius of the NW.

Later it is discussed that for ensemble NW samples which are experimentally

measured, the back contact is not Schottky barrier and is treated as an n-n+

junction, while the top contact is Schottky and can be modeled using a TFE

model.

A single GaAs NW with two Schottky contacts is treated as an M-S-M structure (Fig. 1.6) as discussed in Chapter 1, and the simulated I-V curve was obtained by solving Eq. (1.6), (1.10), and (1.13):

$$J_{TE} = A^* T^2 exp\left(-\frac{q\varphi_b}{kT}\right)\left\{exp\left(\frac{qV}{kT}\right) - 1\right\} \tag{1.6}$$

$$J_{TFE} = \frac{A^{**}T}{k}\sqrt{\pi E_{00}q\left[V + \frac{\varphi_b}{cosh^2(E_{00}/kT)}\right]}\,exp\left(-\frac{q\varphi_b}{E_0}\right)exp\left(\frac{qV}{\epsilon'}\right) \tag{1.10}$$

where E_0, E_{00} and ϵ' are given in equations (1.8), (1.9) and (1.11), respectively. The current density for the NW is given by Eq. (1.13):

$$J_{NW} = \frac{V_{NW}}{A_{NW}R_{NW}} \tag{1.13}$$

Bulk GaAs parameters were used in the equations as shown in Table 4.1.

The current passing through each component (Schottky barrier 1, NW, and Schottky barrier 2) is the same and is given by:

$$I = A_1 J_1 (V_1, \varphi_{b1}) + V_1/R_{sh}^1 = V_{NW}/R_{NW} = A_2 J_2 (V_2, \varphi_{b2}) + V_2/R_{sh}^2 \tag{4.1}$$

where A_1 and A_2 are contact areas of Schottky barriers 1 and 2, respectively. The cross-sectional area of the NW is taken as the contact area in the modeling. R_{sh}^1 and R_{sh}^2 are the shunt resistance of Schottky barriers 1 and 2 which are on the order of GΩ for this model. J_1 and J_2 are the current density passing through Schottky barrier 1 and 2, respectively. R_{NW} is the resistance of the NW which is given by Eq. (1.14). V_1, V_2, and V_{NW} are the voltages across Schottky barrier 1, 2,

and NW, respectively, and their dependence with applied voltage (V) is given by

Eq. (1.12):

$$V = V_1 + V_{NW} + V_2 \qquad (1.12)$$

Table 4.1   Parameters for bulk GaAs

Parameter	Value	Unit
Resistivity (ρ) (for 10^{18} cm^{-3} dopant concentration)	2×10^{-3}	Ω-cm
Effective mass of electron ($m_e{}^*/m_0$)	0.063	------
Relative permittivity (ϵ_s)	12	------
Richardson constant (A^*)	8.2×10^4	$A\,m^{-2}\,K^{-2}$
Effective Richardson constant (A^{**})	4.4×10^4	$A\,m^{-2}\,K^{-2}$
Holes diffusion constant	10	$cm^2 s^{-1}$
Intrinsic carrier concentration	1.79×10^6	cm^{-3}
Minority carrier lifetime	10^{-8}	s

First, consider a single GaAs NW where a positive voltage is applied on the

right contact 2 (forward-biased) and negative to the left contact 1 (reverse-biased)

as depicted in Fig. 1.5. The result for a single NW with a diameter of 50 nm,

length of 1.2 μm and dopant concentration of 10^{18} cm^{-3} is shown in Fig. 4.3. The

plot is obtained using $\varphi_{b1} = \varphi_{b2} = 0.5\ eV$. According to Fig. 4.3, the current

flowing through a single NW at 1 V is ~ 1 nA.
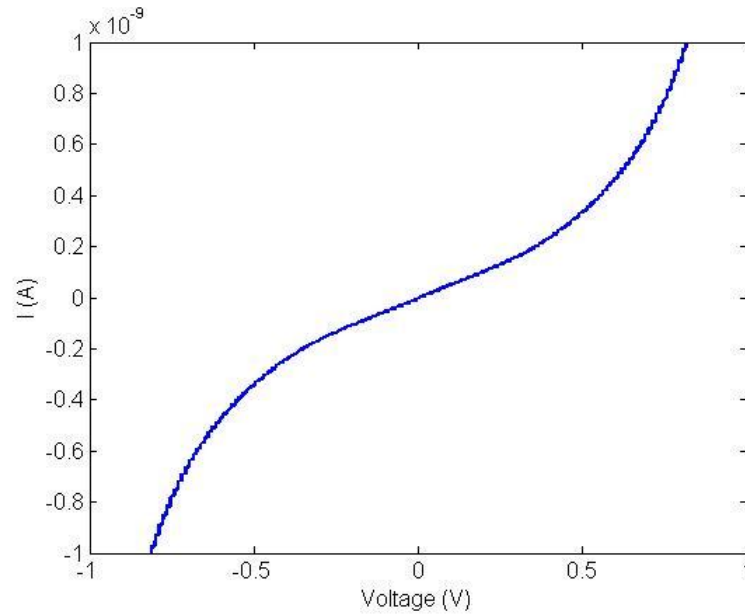
Figure 4.3: Simulated I-V characteristic of a single
GaAs NW using M-S-M structure modeling.
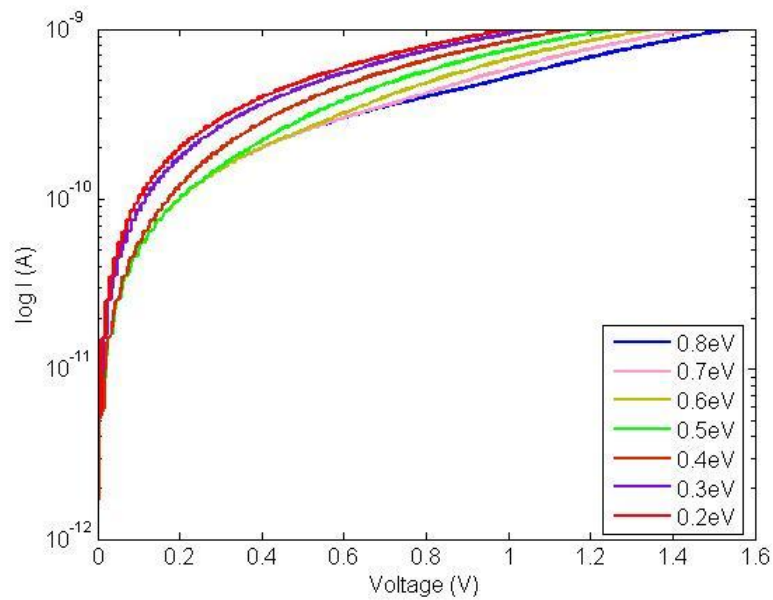
Figure 4.4: Simulated I-V characteristic of a single
GaAs NW for different Schottky barrier heights.
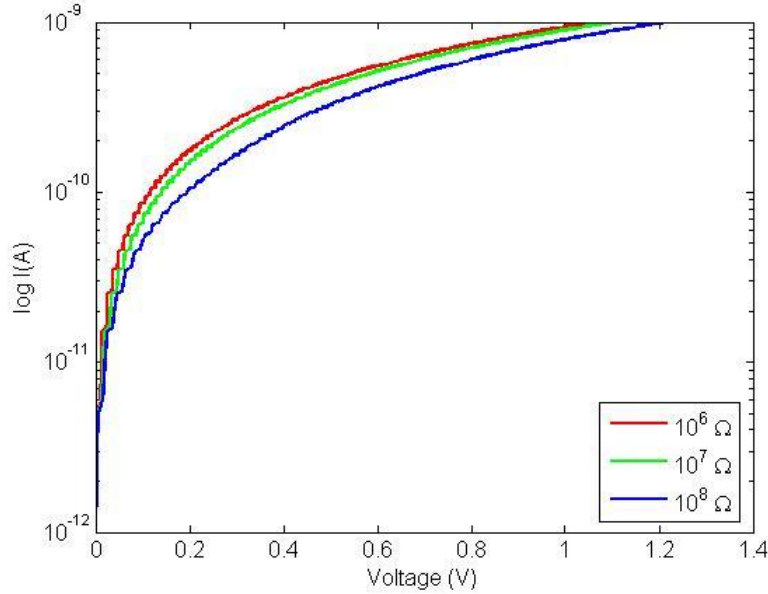
Figure 4.5: Simulated I-V characteristic of a
single GaAs NW for different NW resistance.

The I-V characteristic of a single NW can be significantly affected by the Schottky barrier height. The Schottky barrier of the contact 1 is kept constant at $\varphi_{b1} = 0.5\ eV$ and φ_{b2} is varied from 0.2 eV to 0.8 eV. Fig. 4.4 shows that the current increases by decreasing the Schottky barrier height. The effective diameter of the NW is less than the nominal one due to the depletion effect, which can increase the resistance of the NW and result in a reduction in the current as shown in Fig. 4.5. The barrier heights for this plot are the same as Fig. 4.4 and equal to 0.5 eV for both contacts. According to Eq. (1.13), the current density through the NW depends on NW resistance which also depends on the resistivity and effective diameter of the NW as shown in Eq. (1.14). Passivation can lessen the surface

recombination velocity and depletion width of NWs as discussed in Chapter 3. Thus, the resistance of the NW can be reduced by increasing the effective radius of the NW.

   The I-V characteristic of ensemble NWs is difficult to model due to the diversity of NWs with different diameter, dopant concentration, stacking fault density, and 2-D growth between the NWs. For an ensemble NW model, the current through a single NW for an applied voltage was modeled and multiplied by the number of NWs. The nominal value for the number of NWs was estimated using Fig. 4.2 to be 5.7×10^6 NWs/contact dot. The positive voltage was applied on the top contact (contact 2) and the negative voltage on the back contact (contact 1).

  Unlike single NW modeling, the ensemble NWs modeling cannot be treated as an M-S-M structure. The NWs (doped 10^{18} cm^{-3}) are grown on the substrate with higher dopant concentration ($\geq 2.5 \times 10^{18}$ cm^{-3}). So the back contact (contact 1) consists of a metal deposited on the substrate which is measured and shown to be ohmic, and n-n+ junction. The detail of characteristics of n-n+ junctions which are called low-high junctions can be found in [119-123].

   The current density through the n-n+ junction is given by [119]:

$$J_{nn+} = 2qb\frac{D_p}{L_P}p_n(\exp(qV/2kT) - 1) \qquad (4.2)$$

where D_p and L_p are the hole diffusion constant and diffusion length in the n region (NW).

Since the diffusion length is higher than the length of the NW (L), L_p is

replaced by L. p_n is the hole concentration in n region which can be obtained by:

$$p_n = \frac{n_i^2}{n_n} \tag{4.3}$$

where n_i is the intrinsic carrier concentration of GaAs and $n_n = N_d = 10^{18} cm^{-3}$,

and b is a constant given by:

$$b = \frac{\mu_n}{\mu_p} = \frac{D_n}{D_p} \tag{4.4}$$

Eq. 4.2 is very similar to the diode equation [77], but the minority carrier

concentration in n+ region is neglected. Most of the applied voltage appears

across the n region due to higher resistivity, while almost no voltage drop is

measured across the n+ region [121].

Fig. 4.6 shows the measured current through the NW before passivation (BP),

after contact passivation (ACP) and after whole NW passivation (AWP).

Experimental data are the black solid lines and the simulated curves are the

colored lines. The gray lines are the I-V measured for ACP and AWP after 7

months and show the aging of the passivation.

Before passivation, the effective diameter of NWs was taken to be 1 nm with

shunt resistance around 0.9 GΩ. The fitting showed that for the sample before

passivation more than 95% of NWs did not contribute to the I-V characteristic,

while after contact area passivation this number reduced to 70%. This change can

be attributed to the reduction of Schottky barrier height from $0.5\ eV$ before

passivation to $0.2\,eV$ after passivation. The effective radius of NW and shunt resistance after contact area passivation was kept the same as before passivation.

In the last step, the whole NW was passivated, which included the top contact area as well. The barrier height was kept the same as step 2 and the effective NW diameter was changed from 2 nm to 20 nm. The increase of the diameter decreases the resisitivity of the NW or n region. The enhancement of the effective radius of NWs can be caused by the reduction of surface states density and band bending after passivation. The shunt resistance was also reduced to 0.1 GΩ. According to the model, after passivating the whole surface, nearly all NWs contributed to the I-V characteristic.

Although sulfur passivation improves the optical and electrical properties of III-V semiconductor devices, the short time stability is problematic. As shown in Fig. 4.6 (gray dot-dashed lines), the current measured through a passivated device decreased after seven months.

The change predicted in the reduction of Schottky barrier height and resistivity of the NWs by the model can be attributed to the change in the density of surface states, which will be modeled in more detail in future work.
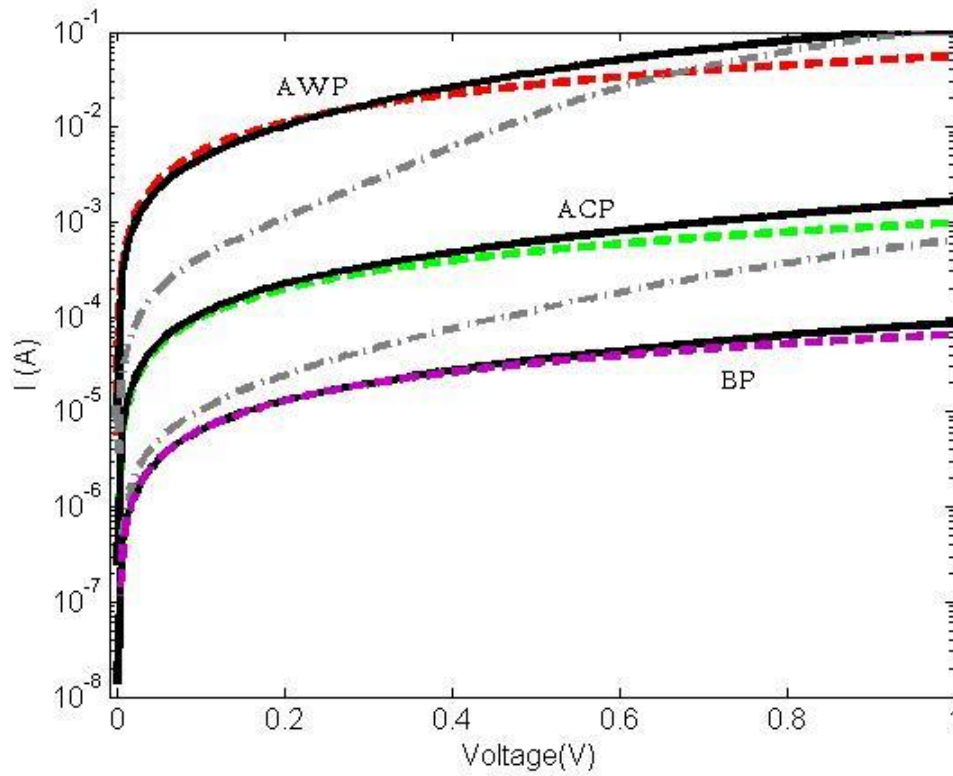
Figure 4.6: I-V characteristic measured (solid black lines) and simulated (dashed lines) for ensemble n-GaAs NWs for different states before passivation (BP), after contact passivation (ACP), and after whole NW passivation (AWP). The I-V measured for AP after seven months is also shown to investigate the stability of the passivation (dot-dashed gray lines).

4.4 Conclusions

The effect of sulfur passivation on the I-V characteristic of ensemble n-GaAs NWs was investigated by measuring the current before passivation (BP), after contact area passivation (ACP) and after whole NW passivation (AWP). It was observed that sulfur passivation increases the current through the NW ensemble for both ACP and AWP. The ensemble NW with top and back contacts was treated as a Schottky top contact and n-n+ structure and modeled through thermionic field emission (TFE) theory. Fitting the simulated results with the measured ones, displayed a reduction of around 0.2 eV in Schottky barrier height and two order of magnitude decrease in resistance of a single NW.

Chapter 5

Sulfur Passivation of GaAs Nanowire Solar Cells

5.1   Introduction

NWs have several potential advantages in comparison to planar structures for photovoltaic (PV) or solar cell devices. NWs have reduced reflectivity over a broader wavelength range as well as a weaker dependence on illumination angle and polarization compared to conventional anti-reflection coatings [124-126]. Coaxial p-n structures enable efficient carrier collection across the NW radius for high photoconversion efficiency [127]. Freedom from lattice-matching requirements due to strain relaxation at the NW sidewall surfaces provides an opportunity to fabricate III-V NWs on inexpensive substrates such as Si [128].

Although the theoretical calculations predict the overall efficiency up to 30% [129] for NW-based solar cells, the reported efficiency of solar cells using NWs as a light harvesting medium is still less than 5% which are mentioned briefly in the following. All the NW solar cells discussed here are grown through VLS growth. Energy conversion efficiency up to 3.4% was measured from 1 sun illuminated single p-i-n coaxial Si NW solar cell [130], while the efficiency of axial p-n Si NW under the same conditions was shown to be 0.5%. The difference

was attributed to the more efficient photogenerated carrier collection in a coaxial structure compared to an axial structure. Radial p-n junction Si NW solar cells on single crystal Si substrate exhibited the efficiency of 1% [131] which after passivation with Al_2O_3 increased to 1.8%.

A solar cell fabricated with n-doped Si NWs grown on p-doped Si wafer by CVD showed 0.1% efficiency [132]. Silicon nanowire-based solar cells on metal foil with efficiency 0.1% was also demonstrated [133]. Photovoltaic behavior was obtained from a single-junction n-Si NW device after electrically heating a small area of the nanowire below the single contact. The observed rectifying behavior was attributed to the formation of a Schottky barrier, a p-n alloy junction, or a combination of these effects. The overall solar energy conversion efficiency of 0.46% was measured [134]. The efficiency 1.65% was achieved from the solar cell structure grown by p-doped GaAs NWs array on n-GaAs(111)B [6]. A radial p-i-n junction GaAs NW solar cell showed the total efficiency of 4.5% [135].

The performance of NW PV devices thus far is limited by factors such as the NW morphology, surface depletion and recombination effects, doping and electrical contact properties [5, 6, 136-139]. Various studies have been reported to optimize the optical and electrical properties of individual NWs by applying surface passivation [61, 63, 140]. In this thesis, we report the use of ammonium polysulfide $(NH_4)_2S_x$ solution to passivate the sidewall surface of GaAs NWs by sulfur bond formation thereby improving solar cell performance. Sulfur passivation is well known to reduce GaAs surface states [141]. As a result,

passivation of NW sidewall surfaces is expected to reduce surface depletion and carrier recombination in NW solar cells, which should increase the open circuit voltage and short circuit current of a NW PV device and increase PV efficiency [118, 142].

Another key issue in NW solar cells is the method of forming contacts to the NWs. In polycrystalline thin film solar cells (e.g., CdTe or CIGS) lateral transport of carriers to finger electrodes occurs via a transparent conducting oxide film (e.g., indium tin oxide (ITO)) as illustrated in Fig 5.1a. Alternatively, in single crystal solar cells (e.g., single crystal Si or III-V cells), lateral transport of carriers to contact fingers can occur directly through a highly doped semiconductor layer as shown in Fig. 5.1b. Both of these contacting schemes have been used analogously in NW solar cells, as shown in Fig. 5.1c and d, although the former method of using ITO is more common. In the specific example of GaAs NW solar cells illustrated in Fig. 5.1e, photogenerated carriers are separated along the NW radius by the core-shell p-n junction with holes conducted to the surrounding ITO top electrode and electrons conducted to the bottom (substrate) electrode. We recently reported the performance of a GaAs NW solar cell with ITO contacts similar to Fig. 5.1c and e [5]. Alternatively, carriers may be conducted by a thin film grown between the NWs, as shown in Fig. 5.1d and f. growth of a thin film between NWs is commonly observed in MBE where material is supplied as adatoms (e.g., Ga, As$_2$ or As$_4$) whose

incorporation is not kinetically limited. Hence, a thin film grows concurrently with the NWs due to vapor-solid deposition on the substrate between the NWs.

In the present paper, we compare the performance of a solar cell fabricated by the alternative contacting methods illustrated in Fig. 5.1e and f. The latter contacting method using contact fingers has certain advantages compared to the scheme using ITO. First, the NWs between contact fingers are exposed directly to illumination without any transmission losses (~10-20%) that are associated with an encapsulating material such as ITO. Furthermore, light trapping effects due to a large refractive index difference at the NW/air interface are not compromised by any encapsulating material. Second, the contact finger method leaves the sidewalls of the NWs between the contact fingers completely exposed to study the effects of surface passivation by sulfur. Third, the avoidance of contact material on the NWs, coupled with surface passivation, avoids deleterious semiconductor/metal interface trap states and associated NW depletion. Finally, the absence of an encapsulating material allows the NWs between contact fingers to be removed by a sonication procedure, such that the contribution to the PV effect of the thin film between NWs can be studied.
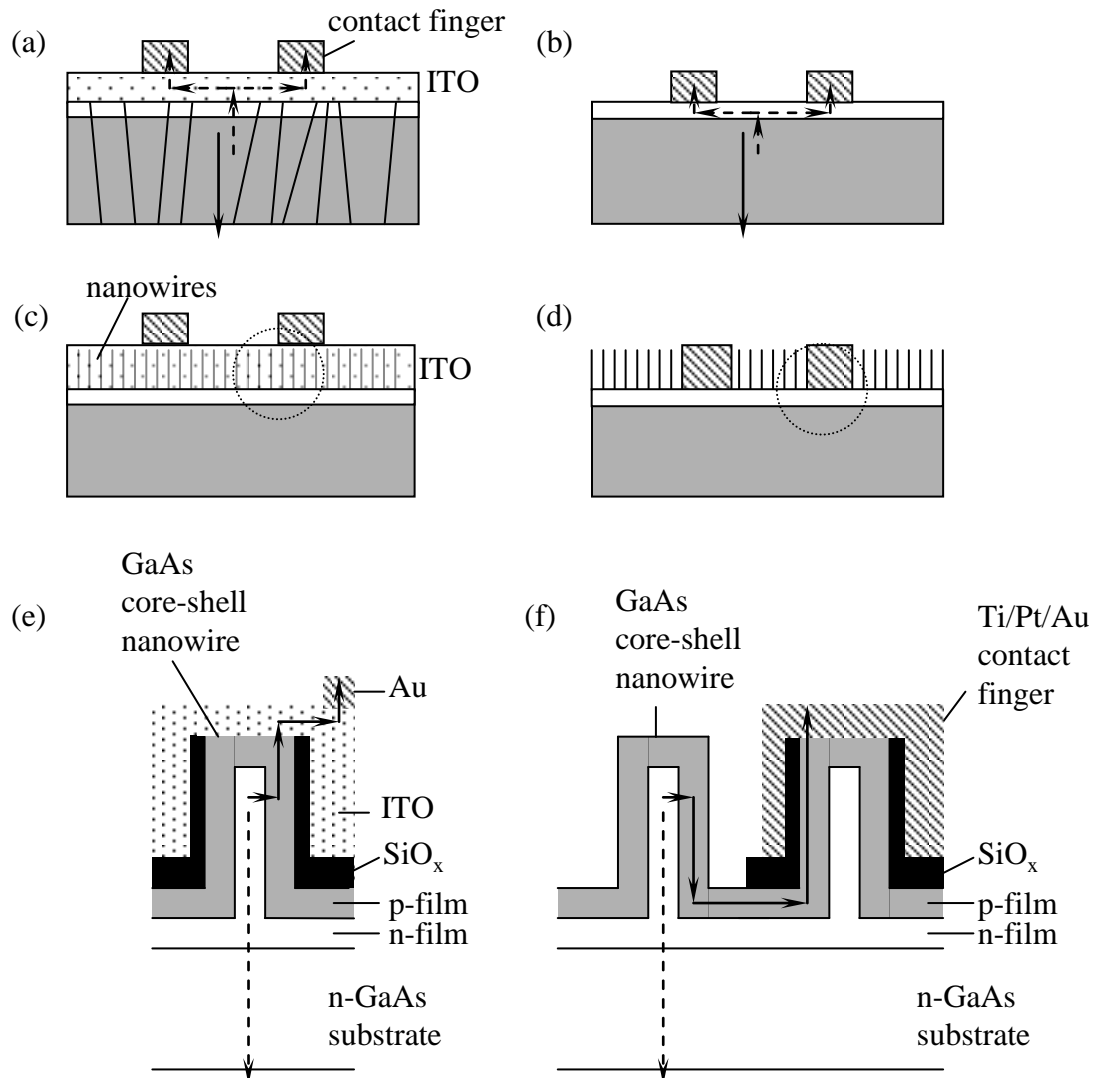
Figure 5.1: Illustration of cross-sectional view of various solar cell contacting methods. Solid and dashed lines indicate transport of opposite carrier types (i.e., holes or electrons). Shading indicates regions of opposite doping type compared to the unshaded regions (i.e., p-type and n-type). Illustrations are not to scale. (a) Au contact fingers on transparent conducting oxide (e.g., ITO) as used, for example, in polycrystalline thin film solar cells. Vertical lines indicate polycrystalline grain boundaries. (b) Contact fingers applied directly to semiconductor as used, for example, in single crystal Si or III-V solar cells. (c) Au fingers on ITO covering the NWs, emulating (a). (d) Contact fingers covering some NWs, emulating (b). (e, f) Enlarged view of circled regions in (c) and (d), respectively, showing carrier transport for the specific case of GaAs p-n core-shell NW solar cells.

5.2   Experimental Details

GaAs core-shell NWs were grown on an n-GaAs (111)B substrate (n~5x10^{18} cm^{-3}) via the VLS method in a GS-MBE system using Au as a seed particle. The GaAs (111)B substrate was first cleaned by a 20 min UV ozone treatment to remove hydrocarbons and other contamination, followed by a 30 s buffered HF treatment to remove native oxide, and finally rinsed in deionized water for 10 min. After cleaning, 1 nm of Au was deposited at room temperature by electron beam evaporation. Prior to NW growth, the substrate surface was degassed at 300 ˚C for 15 min under ultrahigh vacuum in a MBE preparation chamber. After *in situ* inductively coupled hydrogen plasma treatment under As$_2$ flux at 550 ˚C for 10 min, the Au film dispersed into uniformly distributed nanoparticles on the substrate surface. In the GS-MBE system, Ga was supplied from a solid elemental effusion cell and As$_2$ was supplied from a hydride gas cracker operating at 950 ˚C. The growth temperature, V/III flux ratio and 2D growth rate were set to 565 ˚C, 2.3, and 1μm·h^{-1}, respectively. The NW growth was initiated by opening the Ga effusion cell shutter. Core-shell p-n structured NWs were formed by appropriate switching of the p- and n-type dopants during growth. Te from a GaTe effusion cell was used for n-type doping and a Be effusion cell was used for p-type doping with concentrations of about 4×10^{18} cm^{-3} and 5×10^{18} cm^{-3}, respectively. After growing the Te-doped core for 7.5 min, the GaTe effusion cell shutter was closed and the Be effusion cell shutter was opened for 17.5 min of p-doped shell growth.

Previous studies have established that radial core-shell p-n structures will form under the present growth conditions [5]. The morphology of NWs was surveyed using a JEOL JSM-7000F field emission SEM.

 For device fabrication, the top electrode was isolated to the tip of the NWs to prevent Schottky barrier depletion of the thin NWs due to the metal/semiconductor interface. To isolate the contact to the tip of the NW, a 10 nm layer of SiO_x as illustrated in Fig. 5.1e,f was deposited on the NWs by plasma enhanced chemical vapor deposition. Before contact deposition, a two-step photolithography process was performed. First, Shipley S1808 photoresist was deposited on the sample and rested for 10 min to ensure penetration into the space between NWs. Next, the photoresist was spin-cast at 4000 rpm for 30 s. The photoresist from the tip of the NWs was removed by 2 min of oxygen reactive ion etching. The exposed oxide at the tip of the NWs was subsequently removed by etching in buffered HF for 20 s, followed by soaking in acetone for 10 min to remove the remaining photoresist which worked as an etch mask.

  In the second step, the area for contact formation was defined by a lift-off procedure. The sample was covered with Shipley S1827 photoresist and allowed to rest for 10 min. Spin-casting was done at 4000 rpm for 20 s. After mask exposure, the photoresist was developed by MF319 developer and dried with N_2. The opaque contacts defined by the mask was comprised of 79 interdigitated finger electrodes, shown in Fig. 5.2, each with length of 1928 μm, width of 8 μm, and spacing between fingers of 8 μm. The contact fingers were formed by

depositing a 2-D equivalent thickness of 250 nm Ti, 500 nm Pt, and 400 nm Au

on top of the NWs by electron beam evaporation at room temperature. Note that

these thicknesses corresponded to less than 100 nm of deposited thickness on the

NWs due to the large surface area of the NWs relative to a planar surface. The

back contact was formed by depositing 25 nm Ni, 50 nm Ge and 120 nm of Au by

e- beam evaporation. After contact deposition, HF etching removed the SiO_x from

the surface of the NWs located between the contact fingers to permit later

passivation of the NW sidewalls by sulfur. Before passivation, the sample was

annealed at 400 ˚C for 30 s for ohmic contact formation. The sample was bonded

from the back contact to a piece of copper using Ag epoxy for current-voltage (I-

V) measurements.

  Cell I-V characteristics were obtained by contacting the interdigitated finger

electrodes on top of the NWs and the substrate electrode. I-V characteristics were

measured by a Keithley 2400 source meter. The energy conversion efficiency was

measured by illuminating the device using a Newport 96000 solar simulator under

1 Sun or under slight concentration of 2.6 Suns (=260 mW/cm^2, which was the

maximum intensity available from the solar simulator). Current density was

obtained by dividing the measured current by the finger electrode contact area of

0.0122 cm^2. Solar cell performance was assessed by the standard metrics of open

circuit voltage (V_{oc}), short circuit current (I_{sc}) or current density (J_{sc}), fill factor

(FF) and efficiency (η).

Photocurrent measurements were also obtained by illuminating the device using a He-Ne laser (632.8 nm) focused by a ×10 objective lens resulting in a laser spot diameter of ~5 μm and power of ~70 μW at the sample position. The position of the laser spot on the sample surface was measured directly with a CCD camera. The laser spot was scanned across the contact fingers to obtain spatially-resolved photocurrent measurements. Photocurrent measurements were performed before and after sulfur passivation of the NW sidewalls to assess changes in device performance.

The NWs exposed between the contact fingers were sulfur passivated using a solution of 5 M ammonium polysulfide $(NH_4)_2S_x$ diluted by a factor of 10 in isopropanol alcohol. The passivation was performed by soaking the sample in the passivation solution for 5 min under light from a 30 Watt optical fiber lamp at 62 ˚C. After passivation, the device was rinsed in methanol and dried with N_2. The device was heated for 2 s on a hotplate at 200 ˚C to remove the elemental sulfur left on the sample. All passivation procedures were performed in a glove box under N_2 ambient to prevent the re-oxidation of the GaAs surface during the passivation procedure.

Sulfur passivation was assessed on single NWs using room temperature μ-PL. Single NWs were dispersed on oxidized silicon substrates with surface oxide layers of approximately 350 nm thickness. Single NWs were located by CCD imaging, while μ-PL excitation and collection were performed through a microscope objective with numerical aperture of 0.7, providing a spot diameter of

about 1 μm. The excitation was provided by a HeNe laser at wavelength of 632.8 nm with incident light polarized parallel to the NW. PL was resolved by a 75 cm grating spectrometer, and detected by a liquid nitrogen cooled Si CCD camera.

The performance of the finger electrode device was compared to a similar device comprised of 800 μm diameter ITO contact dots. Device fabrication procedures for the ITO dot were similar to that above and as described in detail elsewhere [5].

5.3   Results and Discussion

SEM of the NWs in Fig. 5.2 revealed a maximum NW length of about 3 μm and average diameter of about 50 nm. The NWs exhibited a tapered morphology due to vapour-solid radial growth which occurs simultaneously with the Au-assisted axial growth resulting in core-shell p-n junction NWs as described previously [5].

Fig. 5.3 shows the illuminated I-V characteristics of the NW solar cell with finger electrodes. The solar cell before passivation exhibited V_{oc}=0.14 V, I_{sc}=0.36 mA, FF=0.265 and η=1.09% under 1 Sun illumination (see cell type (1) in Table 1). Under a slight concentration of 2.6 Suns, the solar cell exhibited V_{oc}=0.21 V, I_{sc}=0.94 mA, FF=0.289 and η=1.80% (type (2) in Table 1). When normalized to the illuminated area of 0.0122 cm^2 between finger electrodes, the current measurements at 1 Sun and 2.6 Suns correspond to a current density of 29.5 mA cm^{-2} and 77.0 mAcm^{-2}, respectively. The current (or current density) was

proportional to the illumination as expected. The large change in V_{oc} with concentration can be attributed to the poor fill factor and efficiency in these devices as discussed below.
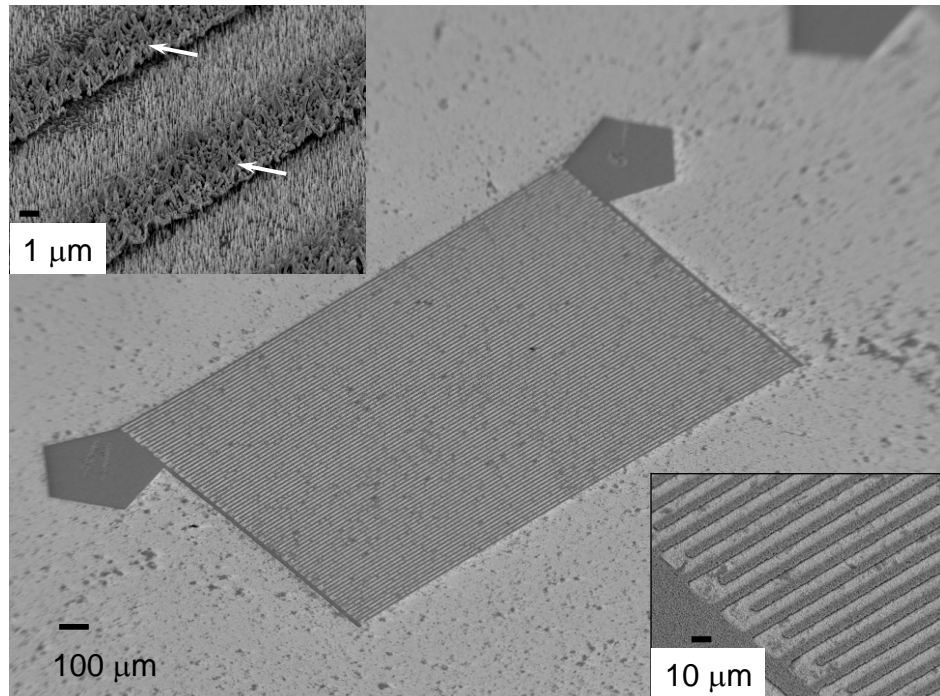
Figure 5.2: Tilted view SEM image of finger contacts on NWs. Dark regions are the contacts. Lower inset shows an enlarged view of contact fingers. Upper inset shows NWs buried under two contact fingers (indicated by arrows) and NWs between the contact fingers.

Table 5.1: Summary of cell measurements

Type of Cell	Illumination (Suns)	V_{oc} (V)	I_{sc} (mA)	FF	η (%)
(1) Finger electrode before passivation	1	0.14	0.36	0.265	1.09
(2) Finger electrode before passivation	2.6	0.21	0.94	0.289	1.80
(3) Finger electrode after passivation	2.6	0.22	1.03	0.30	2.14
(4) Passivated finger electrode after sonication	2.6	0.22	0.31	0.26	0.56
(5) Masked finger electrode (unpassivated)	1	0.04	0.16	0.268	0.14
(6) ITO (unpassivated)	1	0.11	0.18	0.272	1.07
(7) Masked ITO (unpassivated)	1	0.03	0.053	0.276	0.087

The latter results can be compared to a solar cell device fabricated using the same NWs but with 800 µm diameter ITO contact dots that were fabricated in a manner identical to that described previously [5]. In this case, the I-V characteristics (not shown) yielded V_{oc}=0.11 V, I_{sc}=0.18 mA, FF=0.272 and η=1.07% under 1 Sun illumination (type (6) in Table 5.1). Hence, the ITO device efficiency was comparable to that of the finger electrode device. The ITO contact dot with area of 5.02×10^{-3} cm^2 yielded J_{sc}=35.8 mAcm^{-2}. However, the maximum possible current density is 32 mAcm^{-2} at 1 Sun, obtained when all incident photons above the GaAs bandgap are converted to electron-hole pairs; that is, J_{sc} = (q/hc) $\int \lambda I(\lambda)d\lambda$. This indicates that carriers in the present device are being collected over a region larger than that defined by the contact area as will be

discussed further below. In both the ITO and finger electrode devices, a thin film

p-n junction exists between the NWs. This thin film can conduct carriers laterally

to the finger electrodes or ITO dot, such that the collection area is greater than the

contact area. As a result, the actual current density is less than that defined by the

electrode contact area.
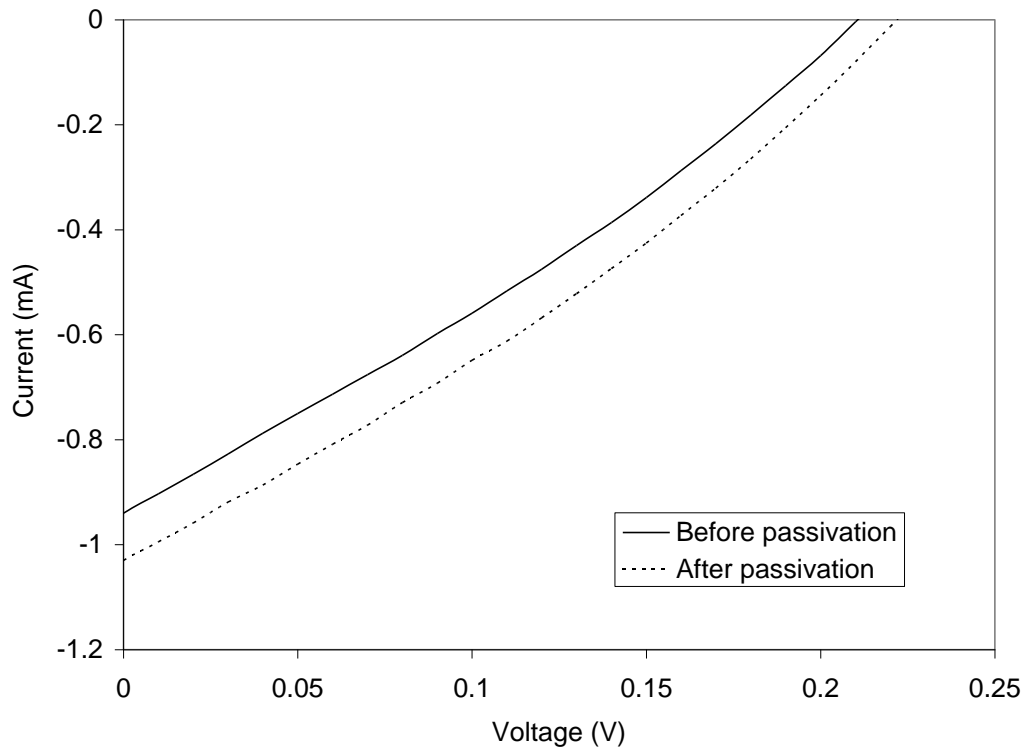
Figure 5.3: Illuminated (2.6 Suns) I-V characteristics of the finger electrode
device before and after sulfur passivation.

   To illustrate that carrier generation and collection occurs from a substantial

region surrounding the finger electrodes or ITO dot, the region surrounding each

contact area was masked with opaque polypropylene material. For example, when

the region surrounding the finger electrode area was masked, the unpassivated cell yielded V_{oc}=0.04 V, I_{sc}=0.16 mA (13.1 mAcm^{-2}), FF=0.268 and η=0.14% under 1 Sun illumination (type (5) in Table 1). Similarly, when the region surrounding the ITO dot was masked, the device (unpassivated) yielded V_{oc}=0.03 V, I_{sc}=0.053 mA (10.6 mAcm^{-2}), FF=0.276 and η=0.087% under 1 Sun illumination (type (7) in Table 5.1). As a result, both devices exhibited worse performance when masked as compared to their unmasked counterparts. The latter results confirmed that significant carrier generation and collection occurred in the regions surrounding the contact area.

  In addition, when the correct contact area is defined, the results show improved performance for the finger electrode device as compared to the ITO device. As will be shown below, this can be explained by the absorption losses associated with the ITO.

  The sheet resistance of the thin film between NWs, which is responsible for lateral conduction, was estimated by measuring the I-V characteristic across the interdigitated contact fingers approximated (ignoring current spreading) by $\rho_\square$= RL/nW where R is the resistance (67Ω) extracted from the linear I-V characteristic measured between interdigitated contact fingers, L is the contact finger length (1928 μm), W is the spacing between contact fingers (8 μm), and n (=79) is the number of contact fingers. The linearity of the I-V measurement (not shown) confirmed that ohmic contacts were formed to the NWs. The value of 204

Ω/□ obtained in this manner can be compared to the nominal sheet resistance estimated by the nominal thickness and doping of the film. The nominal 2-D growth rate of 1 μm·h^{-1} and the growth duration of 17.5 min used for the p-doped shell correspond to a maximum possible film thickness of 291 nm. The nominal sheet resistance of a p-doped GaAs layer with thickness of 291 nm and nominal doping concentration of 5×10^{18} cm^{-3} is 344 Ω/□ [77], which is the same order of magnitude as that measured. This comparison indicates that the thin film between NWs is of reasonable sheet resistance to conduct carriers laterally to the contact region. Further demonstration of lateral carrier transport was provided by laser scanning measurements discussed below.

Room temperature μ-PL was measured on identical NWs before and after sulfur passivation. No detectable μ-PL was obtained prior to sulfur passivation, while measurable μ-PL intensity was obtained after sulfur passivation as shown in Fig. 5.4 for a representative NW. The sulfur passivation improved μ-PL intensity substantially probably by reducing surface states and surface recombination. The peak intensity occurred at 1.421 eV, close to the expected bulk GaAs bandgap energy of 1.424 eV.
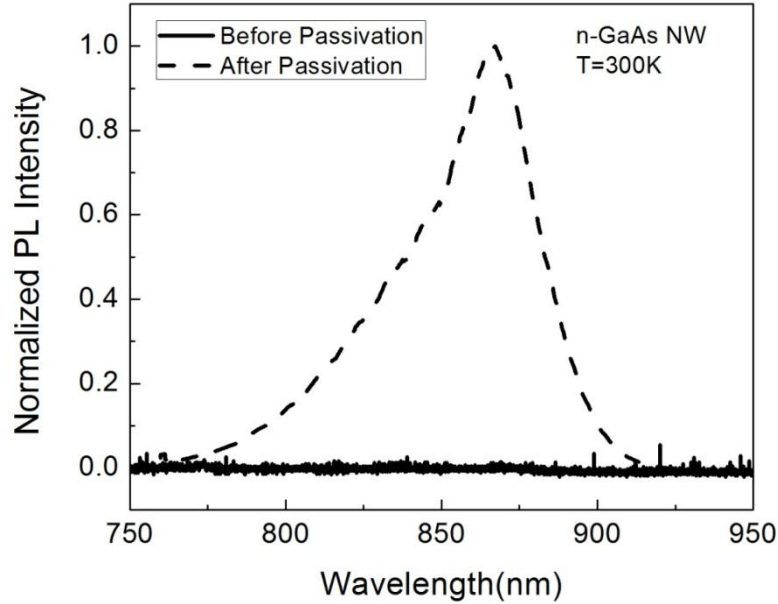
Figure 5.4: Room temperature μ-PL from a single
NW before and after sulfur passivation.

Fig. 5.5 compares the performance of the finger electrode device before and
after sulfur passivation. After passivation, the device gave V_{oc}=0.22 V, I_{sc}=1.03
mA, FF=0.30 and η=2.14% under 2.6 Suns illumination (type (3) in Table 5.1).
Compared to the unpassivated cell, V_{oc}, J_{sc}, FF and η improved with passivation.
The relative improvement in cell efficiency was 19%.

The efficiency of sulfur passivation was also assessed by laser scanning
photocurrent measurements before and after passivation and after removal of the
NWs by a sonication procedure in acetone for 30 s. The resulting photocurrent
measured at zero applied bias (similar to I_{sc}) at various laser beam positions is

shown in Fig. 5.5. The shaded regions in Fig. 5.5 indicate the location of the NWs covered by the contact fingers. The minimum photocurrent before passivation coincided with the position of the contact fingers due to shadow loss from the contacts, while photocurrent was maximum between the contact fingers due to unshadowed NWs. Photocurrent was non-zero at the position of the contact fingers indicating that the contacts were sufficiently thin to allow transmission of the HeNe laser to the underlying NWs. Photocurrent measured between the contacts improved with passivation from 5 to 6 µA, while photocurrent measured under the contact area did not change after passivation since the NWs covered by the contact metal were not exposed to the sulfur passivation.

Next, laser scanning measurements were performed after removal of NWs between the contact fingers by the sonication procedure. After sonication, NWs protected under the contact fingers were left intact while surrounding NWs were removed as verified by SEM measurements (not shown). As observed in Fig. 5.5, photocurrent between the contact fingers decreased appreciably after sonication with a relatively small photocurrent remaining that can be attributed to the remaining thin film p-n junction that grew between the NWs. On the other hand, photocurrent did not change at the contacts since NWs were not removed by sonication in this area due to the protective covering of the contact. Overall, the laser measurements indicated a dominant effect from the NWs between the contact fingers as compared to the thin film or those NWs buried under the contact.
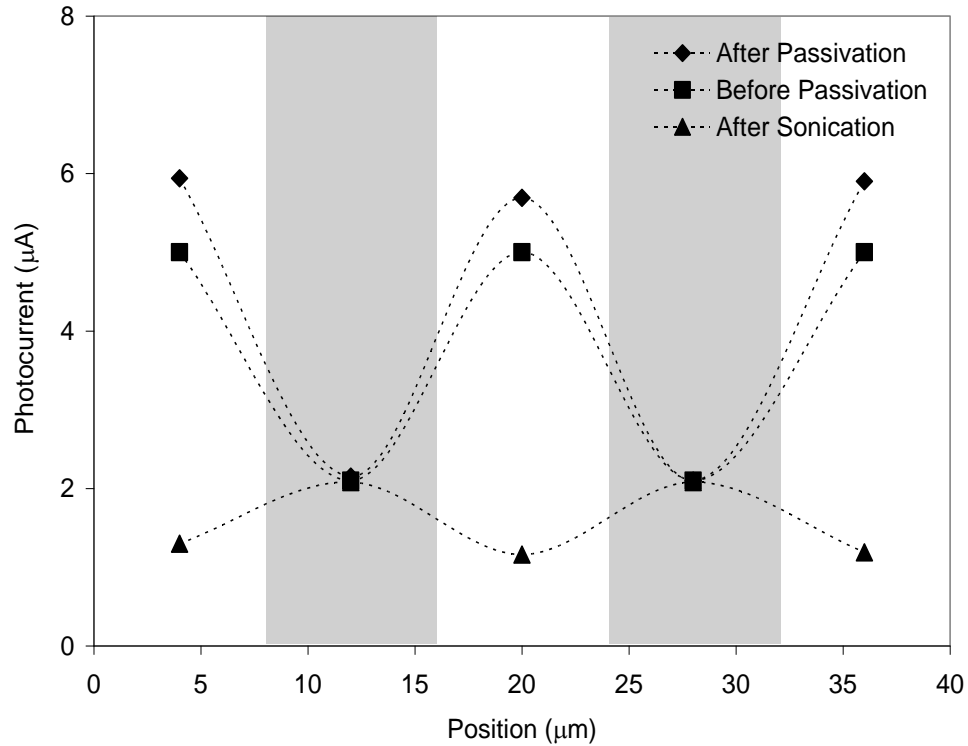
Figure 5.5: Photocurrent measured by HeNe laser scanning on finger electrode device. Shaded regions indicate the location of contact fingers. Data points indicate positions of photocurrent measurement. Dashed lines are guides to the eye.

Laser scanning measurements were also performed for the ITO device. Fig. 5.6 shows the photocurrent measured as the laser was scanned across two contact dots with the probe contacting one ITO dot near the 1100 μm position. Photocurrent increased when the laser was immediately moved off the edge of the ITO contact dot indicating significant absorption losses from the ITO. A measurable current

was obtained in the region between contact dots due to collection of photogenerated carriers along the thin film between NWs. The slope of photocurrent versus position between the two contacts indicate a hole drift-diffusion length of ~300 to 350 μm which is probably limited by the large leakage current in these devices.
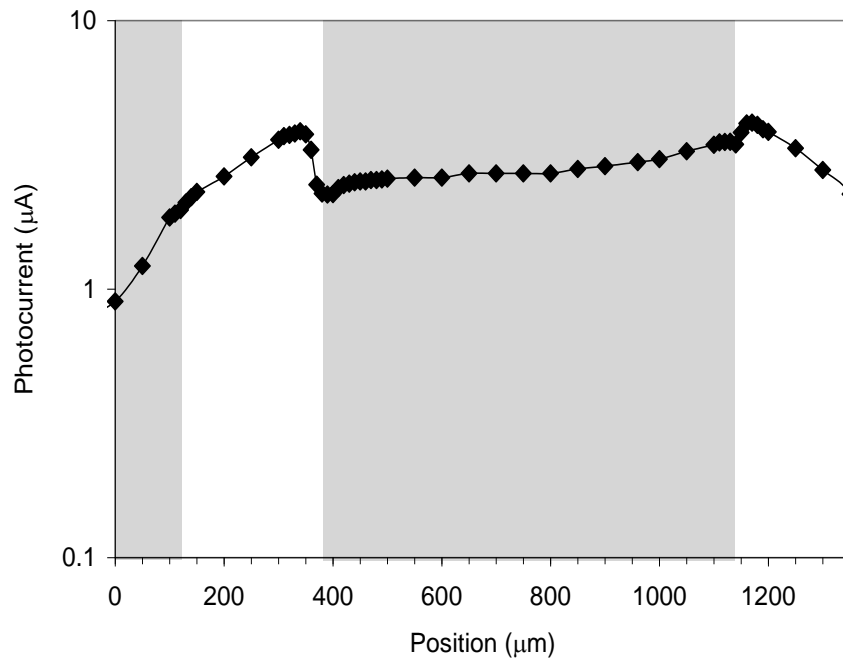
Figure 5.6: Photocurrent measured by HeNe laser scanning on ITO device. Data points indicate positions of photocurrent measurement. The shaded regions indicate the positions of the ITO contact dots. The contact probe was placed near the 1100 μm position.

Although sulfur passivation has been shown as an effective method for improving the optical and electrical performance of III-V semiconductor devices, its long-term stability is known to be problematic. The stability of the sulfur

passivation was determined by measuring the finger electrode cell efficiency over time. The cell was left in ambient air and dark conditions between solar cell measurements. The 2.6 Sun efficiency decreased steadily from 2.14% measured immediately after passivation to a value of 1.80% after 7 days, which was equal to the efficiency prior to passivation. When the passivation was repeated a second time, the improved efficiency was recovered indicating reproducibility in the passivation process.

5.4 Conclusions

Sulfur passivation was shown to improve the PV characteristics of core-shell p-n junction GaAs NW solar cells. Although sulfur passivation is unlikely to be adopted for solar cells due to stability issues, the results demonstrated the potential for cell improvement with sidewall surface passivation. Longer term passivation strategies consist, for example, of AlGaAs shells on the GaAs NWs [59]. Further improvement in the NW solar cell can be expected by implementing an intrinsic layer between the n-doped core and p-doped shell of the NWs to reduce the deleterious effects of tunneling and to provide field-assisted carrier collection. The sheet resistance of the hole conducting p-doped film between NWs was estimated at several hundred ohms/square. This sheet resistance could be reduced by reversing the n- and p-doping; i.e., by employing a p-doped core with an n-doped shell layer. An n-doped surface layer at a doping concentration of 5×10^{18} cm^{-3} should exhibit a sheet resistance of 21 $\Omega/\square$, comparable to the best planar ITO results [77]. With this sheet resistance, the finger contact spacing could be increased to several millimeters with negligible resistive power loss, thereby reducing the contact shadow loss [143]. Overall, the results suggest an alternative strategy to ITO for carrier collection, analogous to that employed in high efficiency III-V or Si cells.

Chapter 6

Conclusions and Future Work

6.1 Thesis Summary

Sulfur passivation of NWs was investigated in this study by measuring changes in optical properties of InP NWs, electrical properties of GaAs NWs, and efficiency of NW solar cells. Sulfur passivation, as an effective passivation method for III-V semiconductors, was optimized for NWs. Ammonium polysulfide $(NH_4)_2S_x$ was used for passivation. The high etching rate of stock solution, which is not appropriate for NWs, was reduced by diluting the solution in different solvents: DI water, methanol, and IPA. IPA was chosen as a proper solvent on the basis of PL measurements on individual InP NWs. Since the concentration of elemental sulfur in the solution helps the formation of the passivation layer, the optimum concentration was found to be 0.5 M again through the PL measurements. After making a 0.5 M solution diluted with IPA, the NWs were soaked in the solution for different times and the appropriate time was obtained by investigating the diameter of NWs before and after passivation using SEM. It was found that 5 min is suitable for both optimum passivation layer formation and the minimum loss of the material due to the solution etch. The optimized solution was applied both on dispersed single p-InP NWs and on a piece of as-grown sample with vertical NWs. While in the first case just the top

surface of the NWs was passivated, in the second case the whole surface was passivated. The PL increase after passivation was in a wide range of 1-20 times for the first group and 1-40 times for the second group. The maximum increase in PL for vertical NWs was twice that for individual NWs. The whole passivation procedure was performed in the glove box at 62°C and under light illumination. The PL from single NWs was also modeled by solving Poisson's equation and the continuity equation numerically and found that 40 times increase in the PL from single NW was caused by a reduction of surface recombination velocity from 10^6 cm/s before passivation to 10^4 cm/s after passivation.

The I-V characteristic of ensemble n-GaAs NWs was measured before sulfur passivation, after contact area passivation, and after the whole NW surface passivation. It was observed that the current flowing through the NWs increased significantly after passivation. The I-V characteristic of ensemble NWs was modeled on the basis of a metal-semiconductor structure, using thermionic theory. It was found that after passivation the Schottky barrier height of top contact was reduced by 0.2 eV and the resistance of NWs decreased by two orders of magnitude.

The effect of sulfur passivation was investigated on core-shell GaAs NW solar cells. Non-contacted NWs were sulfur passivated but the contacted NWs under the opaque metal contact were left unpassivated. The relative efficiency of the solar cell increased around 19% after passivation. Higher photocurrent was also measured from the passivated NWs, while the photocurrent from the

unpassivated NWs didn't change. The effect of 2D growth between the NWs was investigated by covering the areas around the solar cell device using opaque polypropylene material and also by removing the NWs from non-contacted areas by sonication. In both cases, a reduction was observed in the efficiency of the cell which showed the contribution of the thin film between NWs to the solar cell.

The stability of sulfur passivation was also investigated by leaving the passivated NWs in ambient. It was observed that the PL from passivated NWs and also the efficiency of solar cells returned to the unpassivated values after 7 days. Covering the passivated surface by SU8 was presented to increase the stability for more than 7 months.

6.1   Future work

For optimization of NWs for future application in nano-devices, along with extension of surface passivation, further characterization techniques are required. In the current study, it was shown that sulfur passivation can enhance the PL from single p-InP NWs, the current through ensemble n-GaAs NWs, and the efficiency of core-shell n-GaAs NW solar cells. In the following, some of the areas which need to be further investigated are discussed.

➢   The effect of passivation from solution was shown to be effective, while the passivation from gas phase can also be inspected. It needs to be performed in an ultrahigh vacuum environment. Unlike the liquid phase passivation, which

removes the native oxide before sulfur bond formation, in the gas phase passivation, additional surface preparation should be performed before passivation layer formation such as high temperature annealing (T>600 ˚C) [144] or UV radiation in an ultrahigh vacuum [145].

➢   The stability of sulfur passivation is an important subject which needs more research. When the sulfur passivated NW is left in ambient for some days, degradation happens due to the reaction with oxygen. We showed that the stability can increase from a few days to several months by covering the passivated layer with a polymer. The effect of other coatings such as SiO_2 or Si_3N_4 can be examined.

➢ Surface potential is one of the key parameters which need to be measured before and after passivation. By measuring the surface potential the amount by which the band bending is changed after passivation can be determined. The surface potential can be measured using Raman spectroscopy [117], or scanning Auger electron microscopy [146].

➢ X-ray photoelectron spectroscopy (XPS) can help to detect various bonding formations on the surface before and after passivation. This becomes more interesting with sulfur passivation, which highly depends on surface orientation, is applied on NWs with multiple facets and different orientations.

➢ I-V characteristic of single NWs can reveal more information about the electrical properties of NWs compared to the ensemble NWs. The contacts

area can be passivated separate from the bulk of the NW and the effect of both parts on the total current can be determined with higher precision.

➢ Normally the NW-based devices are made by using ensemble NWs on as grown samples. One of the critical parts which greatly affect the device functionality is the back contact. As discussed in Chapter 4, the formation of an n-n+ junction disturbs the ohmicity of the back contact. The carrier transport through these junctions can be analysed by examining samples with different dopant concentrations in substrates and NWs. Optimization of the back contact can improve the functionality of NW-based devices such as solar cells.

➢ A model was developed in Chapter 4, to justify the measured I-V curves. It was shown that the passivation reduces the barrier height of the top Schottky barrier and resistivity of the NWs. This change can be attributed to the reduction of surface states and/or depletion width of the NWs. Using the continuity equation and Poisson's equation, a model can be developed to numerically quantify the predicted change in density of surface states and depletion width after passivation.

➢ In the polarization setup used for the current study, the polarization of the excitation beam was manipulated. To analyze the polarization of the emitted PL, the setup should be upgraded by using an extra Glen-Thompson polarizer and a wave plate. Analyzing the polarization of emitted PL before and after

passivation shows the difference in the effectiveness of passivation for the states emitting parallel or perpendicular to the NW's axis.

➢ Since sulfur passivation is a photo-electrochemical reaction, the passivation reported in this research was performed under unpolarized light emission. The effect of using polarized light can be inspected on the quality of the passivant layer formation. The etching rate can also be changed using light polarized parallel or perpendicular to the NW's axis.

➢ Time-resolved PL determines the carrier lifetimes and can be used to distinguish different recombination mechanisms in the NWs. It can also be used to determine the contribution of surface states and depletion layer in PL intensity reduction [70,147].

➢ Using spatially-resolved photoluminescence imaging, the whole length of the NW can be scanned and the PL emitted from different parts can be investigated. The PL emission can vary along the NW due to localized states, nonuniformity in dopant distribution, and compositional variations. If a part of a NW is depleted, the position can be determined by 2D PL imaging. After passivation the 2D PL map can be compared before and after passivation and the effect of passivation can be further explored. Using PL mapping, it is shown that the passivated GaAs NW has lower defect states than the unpassivated NW [148].

References

[1]   R. Wagner and W. C. Ellis, Appl. Phys. Lett. **4**, 89 (1964)

[2]   H. J. Choi, *Semiconductor Nanostructures for Optoelectronic Devices; Processing Characterization and Applications (Chapter 1).* (Ed.) G. C. Yi, Springer (2012)

[3]   T. Martensson, C. P. T. Svensson, B. A. Wacaser, M. W. Larsson, W. Seifert, K. Deppert, A. Gustafsson, L. R. Wallenberg, and L. Samuelson, Nano Lett. **4**, 1987 (2004)

[4]   M. H. Huang, S. Mao, H. Feick, H. Yan, Y. Wu, H. Kind, E. Weber, R. Russo, and P. Yang, Science **292**, 1897 (2001)

[5]   J. A. Czaban, D. A. Thompson, and R. R. LaPierre, Nano Lett. **9**, 148 (2009)

[6]   G. Cirlin, A. Bouravleuv, I. Soshnikov, Y. Samsonenko, V. Dubrovskii, E. Arakcheeva, E. Tanklevskaya, and P. Werner, Nano. Res. Lett. **5**, 360 (2010)

[7]   S. A. Fortuna and X. Li, IEEE Electron. Device Lett. **30**, 593 (2009)

[8]   S. Vandenbrouck, a. D. K. Madjour, Y. Dong, a. C. M. L. Y. Li, and C. Gaquiere, IEEE Electron. Device Lett. **30**, 322 (2009)

[9]   O. Hayden, R. Agarwal, and C. M. Lieber, Nat. Mater. **5**, 352 (2006)

[10]   H. Pettersson, J. Tragardh, A. L. Persson, L. Landin, D. Hessman, and L. Samuelson, Nano Lett. **6**, 229 (2006)

[11]   F. Patolsky and C. M. Lieber, Mater. Today **8**, 20 (2005)

[12]   E. Lai, W. Kim, and P. Yang, Nano. Res. **1**, 123 (2008)

[13]   W. Braun, V. M. Kaganer, A. Trampert, H. P. Schnherr, Q. Gong, R. Ntzel, L. Dweritz, and K. H. Ploog, J. Cryst. growth **227-228**, 51 (2001)

[14]   U. Krishnamachari, M. Borgstrom, N. P. B. J. Ohlsson, L. Samuelson, W. Seifert, M. W. Larsson, and L. R. Wallenberg, Appl. Phys. Lett. **85**, 2077 (2004)

[15]   D. E. Perea, J. E. Allen, S. J. May, B. W. Wessels, D. N. Seidma, and L. J. Lauhon, Nano Lett. **6**, 181 (2006)

[16]   M. Tchernycheva, L. Travers, G. Patriarche, F. Glas, G. E. C. J. C. Harmand, and V. G. Dubrovskii, J. Appl. Phys. **102**, 094313 (2007)

[17]   Z. H. Wu, X. Y. Mei, M. B. D. Kim, and H. E. Ruda, Appl. Phys. Lett. **81**, 5177 (2002)

[18]   Y. Wang, V. Schmidt, S. Senz, and U. Gsele, Nat. Nanotechnol. **1**, 186 (2006)

[19]   T. I. Kamins, R. S. Williams, D. P. Basile, T. Hesjedal, and J. S. Harris, J. Appl. Phys. **89**, 1008 (2001)

[20]   B. M. Kayes, M. A. Filler, M. C. Putnam, M. D. Kelzenberg, N. S. Lewis, and H. A. Atwater, Appl. Phys. Lett. **91**, 103110 (2007)

[21]   P. Mohan, R. Bag, S. Singh, A. Kumar, and R. Tyagi, Nanotechnology **23**, 025601 (2011)

[22]   R. Q. Zhang, Y. Lifshitz, and S. T. Lee, Adv. Mater. **15**, 635 (2003)

[23]   B. Mandl, J. Stangl, T. Mrtensson, A. Mikkelsen, J. Eriksson, L. S. Karlsson, G. Bauer, L. Samuelson, and W. Seifert, Nano Lett. **6**, 1817 (2006)

[24]   M. Mattila, T. Hakkarainen, H. Lipsanen, H. Jiang, and E. I. Kauppinen, Appl. Phys. Lett. **90**, 033101 (2007)

[25]   C. Colombo, D. Spirkoska, M. Frimmer, G. Abstreiter, and A. F. i Moral, Phys. Rev. B **77**, 155326 (2008)

[26]   D. E. Aspnes, Surf. Sci. **132**, 406 (1983)

[27]   T. H. Gfroerer, *Photoluminescence in Analysis of Surfaces and Interfaces*, Encyclopedia of Analytical Chemistry*,* (Ed.*)* R. A. Meyers John, John Wiley & Sons, 9209 (2000)

[28]   V. N. Bessolov and M. Lebedev, Semiconductors **32**, 1141 (1998)

[29]   A. M. Green and W. E. Spicer, J. Vac. Sci. Technol. A **11**, 1061 (1993)

[30]   W. E. Spicer, I. Lindau, P. Skeath, and C. Y. Su, J. Vac. Sci. Technol. **17**, 1019 (1980)

[31]   J. Sandroff, R. N. Nottenburg, J. C. Bischoff, and R. Bhat, Appl. Phys. Lett. **51**, 33 (1987)

[32]   W. S. Lour and J. L.Hsieh, Semicond. Sci. Technol. **13**, 847 (1998)

[33]   M. S. Carpenter, M. R. Melloch, M. S. Lundstrom, and S. P. Tobin, Appl. Phys. Lett. **52**, 2157 (1988)

[34]   V. N. Bessolov, E. V. Konenkova, and M. V. Lebedev, J. Vac. Sci. Technol. B **14**, 2761 (1996)

[35]   A. S. Weling, K. K. Kamath, and P. R. Vaya, Thin Solid Films **215**, 179 (1992)

[36]   Y. Tao, A. Yelon, E. Sacher, Z. H. Lu, and M. J. Graham, Appl. Phys. Lett. **60**, 2669 (1992)

[37]   V. N. Bessolov, A. F. Ivankov, and M. V. Lebedev, J. Vac. Sci. Technol. B **13**, 1018 (1995)

[38]   V. N. Bessolov, M. V. Lebedev, and B. V. T. Y. M. Shernyakov, Mater. Sci. Eng. B **44**, 380 (1997)

[39]   J. F. Fan, H. Oigawa, and Y. Nannichi, Jpn. J. Appl. Phys. **27**, 761 (1988)

[40]   N. Shibata and H. Ikoma, Jpn. J. Appl. Phys. **31**, 3976 (1992)

[41]   C. W. Wilmsen, K. M. Geib, J. Shin, R. Lyer, and D. L. Lile, J. Vac. Sci. Technol. B **7**, 851 (1989)

[42]   I. K. Han, D. H. Woo, H. J. Kim, E. K. Kim, J. I. Lee, S. H. Kim, K. N. Kang, H. Lim, and H. L. Park, J. Appl. Phys. **80**, 4052 (1996)

[43]   T. Ishikawa and H. Ikoma, Jpn. J. Appl. Phys. **31**, 3981 (1992)

[44]   H. Sugahara, M. Oshima, H. Oigawa, H. Shigekawa, and Y. Nannichi, J. Appl. Phys. **69**, 4349 (1991)

[45]   S. Arabasz, E. Bergignat, G. Hollinger, and J. Szuber, Appl. Surf. Sci. **252**, 7659 (2006)

[46]   M. Oshima, T. Scimeca, Y. Watanabe, H. Oigawa, and Y. Hannichi, Jpn. J. Appl. Phys. **32**, 518 (1993)

[47]   K. Sato and H. Ikoma, Jpn. J. Appl. Phys. **32**, 921 (1993)

[48]   Y. Dan, K. Seo, K. Takei, J. H. Meza, A. Javey, and K. B. Crozier, Nano Lett. **11**, 2527 (2011)

[49]   Z. M. Liao, K. J. Liu, J. M. Zhang, J. Xu, and D. P. Yu, Phys. Lett. A **367**, 207 (2007)

[50]   K. Keem, J. Kang, C. Yoon, D. Y. Jeong, B. M. Moon, and S. Kim, Jpn. J. Appl. Phys. **46**, 6230 (2007)

[51]   X. H. Sun, S. D. Wang, N. B. Wong, D. D. D. Ma, S. T. Lee, and B. K. Teo, Inorg. Chem. **42**, 2398 (2003)

[52]   K. Seo, S. Sharma, A. A. Yasseri, D. R. Stewart, and T. I. Kamins, Electrochem. Solid-State Lett. **9**, G69 (2006)

[53]   P. Chang, Z. Fan, C. J. Chien, D. Stichtenoth, C. Ronning, and J. G. Lu, Appl. Phys. Lett. **89**, 133113 (2006)

[54]   Y. Cui, Z. Zhong, D. Wang, W. U. Wang, and C. M. Lieber, Nano Lett. **3**, 149 (2003)

[55]   M. H. Yoon, A. Franceschetti, and T. Marks, J. Proc. Natl. Acad. Sci. U.S.A. **102**, 4678 (2005).

[56]   S. Ju, K. Lee, D. B. Janes, M. H. Yoon, A. Facchetti, and T. J. Marks, Nano Lett. **5**, 2281 (2005)

[57]   X. Duan, Y. Huang, and C. M. Lieber, Nano Lett. **2**, 487 (2002)

[58]   A. C. E. Chia, Y. L. M. Tirado, S. Zhao, D. C. Z. Mi, and, and R. R. LaPierre, J. Appl. Phys. **111**, 094319 (2012)

[59]   O. Demichel, M. Heiss, J. Bleuse, H. Mariete, and A. F. i Moral, Appl. Phys. Lett. **97**, 201907 (2010)

[60]   P. Parkinson, H. J. Joyce, Q. Gao, H. H. Tan, X. Zhang, J. Zou, C. Jagadish, L. M. Herz, and M. B. Johnston, Nano Lett. **9**, 3349 (2009)

[61]   D. B. Suyatin, C. Thelander, I. M. M. T. Bjork, and L. Samuelson, Nanotechnology **18**, 105307 (2007)

[62]   Q. Hang, F. Wang, P. D. Carpenter, D. Zemlyanov, D. Zakharov, E. A. Stach, W. E. Buhro, and D. B. Janes, Nano Lett. **8**, 49 (2008)

[63]   L. K. van Vugt, S. J. Veen, E. P. A. M. Bakkers, A. L. Roest, and D. Vanmaekelbergh, J. Am. Chem. Soc. **127**, 12357 (2005)

[64]   J. F. Fan, H. Oigawa, and Y. Nannichi, Jpn. J. Appl. Phys. **27**, L2125 (1988)

[65]   M. S. Carpenter, M. R. Melloch, and T. E. Dungan, Appl. Phys. Lett. **53**, 66 (1988)

[66]   W. S. Hobson, F. Ren, U. Mohideen, R. E. Slusher, M. L. Schnoes, and S. J. Pearton, J. Vac. Sci. Technol. A **13**, 642 (1995)

[67]   N. Tajik, A. C. E. Chia, and R. R. LaPierre, Appl. Phys. Lett. **100**, 203122 (2012)

[68]   S. Perkowitz, *Optical Charactetization of Semiconductors: Infrared, Raman, and Photoluminescence Spectroscopy*. Academic Press (1993)

[69]   H. V. Ryswyk and A. B. Ellis, J. Am. Chem. Soc. **108**, 2454 (1986)

[70]   S. R. Lunt, G. N. Ryba, P. G. Santangelo, and N. S. Lewis, J. Appl. Phys. **70**, 7449 (1991)

[71]   S. Krawczyk, B. Bailly, B. Sautreuil, R. Blanchet, and P. Viktorovitch, Electron. Lett. **20**, 255 (1984)

[72]   R. R. Chang, R. Iyer, and D. L. Lile, J. Appl. Phys. **61**, 1995 (1987)

[73]   J. Bardeen, Phys. Rev. **71**, 717 (1947)

[74]   A. M. Cowley and S. M. Sze, J. Appl. Phys. **36**, 3212 (1965)

[75]   H. Norde, J. Appl. Phys. **50**, 5052 (1979)

[76]   http://www.ecse.rpi.edu/ schubert/Course-ECSE-2210

[77]   S. M. Sze and K. K. Ng, *Physics of Semiconductor Devices,* John Wiley & Sons, 3rd Edition (2007)

[78]   Z. Zhang, K. Yao, Y. Liu, C. Jin, X. Liang, Q. Chen, and L. M. Peng, Adv. Funct. Mater. **17**, 2478 (2007)

[79]   N. Tajik, C. M. Haapamaki, and R. R. LaPierre, Nanotechnology **23**, 315703 (2012)

[80]   N. Tajik, Z. Peng, P. Kuyanov, and R. R. LaPierre, Nanotechnology **22**, 225402 (2011)

[81]   G. Biasiol and L. Sorba, *Crystal Growth of Materials for Energy Production and Energy-saving Applications; Molecular Beam Epitaxy: Principles and Applications,* (Eds.) R. Fornari and L. Sorba, (Edizioni ETS, Pisa), 66 (2001)

[82]   http://www.thorlabs.com

[83]   http://www.janis.com/products/productsoverview/SuperTranContinuous
         FlowCryostatSystems.aspx

[84]   Imaging Spectrometers, HORIBA JOBIN YVON manual.

[85]   http://www.laserfocusworld.com/articles/2012/01/optical surfaces-
         toroidal-mirrors.html

[86]   Symphony II 1024 by 128 Cryogenic Back-Illuminated CCD Detector,
         HORIBA scientific manual.

[87]   http://www.specinst.com/

[88]   http://www.science20.com/mei/blog/chargecoupleddeviceccd

[89]   J. Liu, *Handbook of Microscopy in Nanotechnology*, (Eds.) N. Yao and
         Z. L.Wang, Kluwer Academic Publishers, 19 (2005)

[90]   Z.Weilie, *Scanning Microscopy for Nanotechnology Techniques and
         Applications,* Springer (2007)

[91]   V. G. Dubrovskii, G. E. Cirlin and V. M. Ustinov, Semiconductors **43**,
         1539 (2009)

[92]   J. Lloyd-Hughes, S. Merchant, L. Fu, H. Tan, C. Jagadish, E. Castro-
         Camus, and M. Johnston, Appl. Phys. Lett. **89**, 232102 (2006)

[93]   C. Gutsche, Christoph; R. Niepelt, M. Gnauck, A. Lysov, W. Prost, C.
         Ronning and F. J. Tegude, Nano Lett. **12**, 1453 (2012)

[94]   H. Ishimura, K. Sasaki, and H. Tokuda, Inst. Phys. Conf. Ser. **106**, 405
         (1990)

[95]   W. D. Chen, X. Q. Li, L. H. Duan, X. L. Xie, and Y. D. Cai, Appl. Surf.
         Sci. **100–101**, 592 (1996)

[96]   J. F. Wang, M.S. Gudiksen, X.F. Duan, Y. Cui and C.M. Lieber,
         Science **293**, 1455 (2001)

[97]   F. Glas, J. C. Harmand and G. Patriarche, Phys. Rev. Lett. **99**, 146101
         (2007)

[98]   S. Paiman, Q. Gao, H.H. Tan, C. Jagadish, K. Pemasiri, M. Montazeri, H.E. Jackson, L.M. Smith, J.M. Yarrison-Rice, X. Zhang and J. Zou, Nanotechnology **20**, 225606 (2009)

[99]   A. J. Lohn, T. Onishi and N. Kobayashi, Nanotechnology **21**, 355702 (2010)

[100]   J. Bao, D.C. Bell, F. Capasso, J.B. Wagner, T. Martensson, J. Tragardh and L. Samuelson, Nano Lett. **8**, 836 (2008)

[101]   A. Mishra, L.V. Titova, T.B. Hoang, H.E. Jackson, L.M. Smith, J.M. Yarrisson-Rice, Y. Kim, H.J. Joyce, Q. Gao, H.H. Tan and C. Jagadish, Appl. Phys. Lett. **91**, 263104 (2007)

[102]   P. J. Reece, S. Paiman, O. Abdul-Nabi, Q. Gao, M. Gal, H.H. Tan and C. Jagadish, Appl. Phys. Lett. **95**, 101109 (2009)

[103]   M. Mattila, T. Hakkarainen, M. Mulot and H. Lipsanen, Nanotech. **17**, 1580 (2006)

[104]   K. Pemasiri, M. Montazeri, R. Gass, L.M. Smith, H.E. Jackson, J. Yarrison-Rice, S. Paiman, Q. Gao, H.H. Tan, C. Jagadish, X. Zhang and J. Zou, Nano Lett. **9**, 648 (2009)

[105]   K. Ikejiri, Y. Kitauchi, K. Tomioka, J. Motohisa and T. Fukui, Nano Lett. **11**, 4314 (2011)

[106]   J. Wallentin, K. Mergenthaler, M. Ek, L.R. Wallenberg, L. Samuelson, K. Deppert, M. E. Pistol and M.T. Borgstrom, Nano Lett. **11**, 2286 (2011)

[107]   W. Franz, Z. Naturforsch. A **13a**, 484 (1958)

[108]   L. V. Keldysh, J. Exp. Theor. Phys. **33**, 994 (1957)

[109]   M. H. M. van Weert, O. Wunnicke, A. L. Roest, T. J. Eijkemans, A. Yu Silov, J. E. M. Haverkort, G. W. Hooft, and E. P. A. M. Bakkers, Appl. Phys. Lett. **88**, 043109 (2006)

[110]   G. Mariani, P. S. Wong, A.M. Katzenmeyer, F. Leonard, J. Shapiro and D. L. Huffaker, Nano Lett. **11**, 2490 (2011)

[111]   Z. Jin, W. Prost, S. Neumann and F. J. Tegude, J. Vac. Sci. Technol. B **22**, 1060 (2004)

[112]   C. R. McIntyre and L. J. Sham, Phys. Rev. B **45**, 9443 (1992)

[113]   H. E. Ruda and A. Shik, Appl. Phys. Lett. **85**, 1030 (2004)

[114]   K. Mettler, Appl. Phys. **12**, 75 (1977)

[115]   E. B. X. Correig, J. Calderer, and R. Acubilla, Solid-State Electron. **33**, 477 (1990)

[116]   Q. H. Li, Q. Wan, Y. X. Liang, and T. H. Wang, Appl. Phys. Lett. **84**, 4556 (2004)

[117]   X. Chen, and X. Si, and V. Malhotra, J. Electrochem. Soc.**140**, 2085 (1993)

[118]   B. S. Simpkins, and M. A. Mastro, and C. R. Eddy, and P. E. Pehrsson, J. Appl. Phys. **103**, 104313 (2008)

[119]   R. W. Lade, and A. G. Jordan, J. Electron. and Control **13**, 23 (1962)

[120]   G. G. E. Low, Proc. Phys. Soc. B **68**, 310 (1955)

[121]   J. B. Gun, J. Electron. and Control **4** , 17 (1957)

[122]   A. G. Sabnis, Solid-State Electron. **22**, 667 (1979)

[123]   T. Daud, and F. A. Lindholm, J. Appl. Phys. **59**, 285 (1986)

[124]   L. Hu and G. Chen, Nano Lett. **7**, 3249 (2007)

[125]   L. Cao, P. Fan, A. P. Vasudev, J. S. White, Z. Yu, W. Cai, J. A. Schuller, S. Fan, and M. L. Brongersma, Nano Lett. **10**, 439 (2010)

[126]   E. Garnett and P. Yang, Nano Lett. **10**, 1082 (2010)

[127]   B. M. Kayes, H.A. Atwater and N.S. Lewis, J. Appl. Phys. **97**, 114302
         (2005)

[128]   P. K. Mohseni, C. Maunders, G. A. Botton and R. R. LaPierre,
         Nanotechnology **18**, 445304 (2007)

[129]   R. R. LaPierre, J. Appl. Phys. **110**, 014310 (2011)

[130]   B. Tian, T. J. Kempa, and C. M. Lieber, Chem. Soc. Rev. **38**, 16 (2009)

[131]   O. Gunawan and S. Guha, Sol. Energy Mater. Sol. Cells **93**, 1388 (2009)

[132]   T. Stelzner, M. Pietsch, G. Andra, F. Falk, E. Ose, and S. Christiansen,
         Nanotechnology **19**, 295203 (2008)

[133]   L. Tsakalakos, Mater. Sci. Eng. R. **62**, 175 (2008)

[134]   M. D. Kelzenberg, D. B. Turner-Evans, B. M . Kayes, M. A. Filler, M.
         C. Putnam, N. S. Lewis, and H. A. Atwater, Nano Lett. **8**, 710 (2008)

[135]   C. Colombo, M. Heiss, M. Gratzel, and A. Fontcuberta i Morral,
         Appl. Phys. Lett. **94**, 173108 (2009)

[136]   B. Tian, X. Zheng, T. J. Kempa, Y. Fang, N. Yu, G. Yu, J. Huang and
         C.M. Lieber, Nat. **449**, 885 (2007)

[137]   E. C. Garnett and P. Yang, J. Am. Chem. Soc. **130**, 9224 (2008)

[138]   Y. B. Tang, Z. H. Chen, H. S. Song, C. S. Lee, H. T. Cong, H. M.
         Cheng, W. J. Zhang, I. Bello and S.T. Lee, Nano Lett. **8**, 4191 (2008)

[139]   H. Goto, K. Nosaki, K. Tomioka, S. Hara, K. Hiruma, J. Motohisa and T.
         Fukui, Appl. Phys. Express **2**, 035004 (2009)

[140]   J. W. W van Tilburg, R. E. Algra, W. G. G. Immink, M. Verheijen, E. P.
         A. M. Bakkers and L. P. Kouwenhoven, Semicond. Sci. Tech. **25**,
         024011 (2010)

[141]   G. Eftekhari, Vacuum **67**, 81 (2002)

[142]   S. M. Zervos, Semicond. Sci. Technol. **23,** 075016 (2008)

[143]   S. R. Wenham, M.A. Green, M.E. Watt and R. Corkish, *Applied Photovoltaics*, 2nd Ed. (Earthscan, London, UK, 2007).

[144]   J. R. Waldrop, J. Vac. Sci. Technol. B **3**, 1197 (1985)

[145]   N. Yoshida, S. Chichibu, T. Akane, M. Totsuka, H. Uji, S. Matsumoto, and H. Higuchi, Appl. Phys. Lett. **63**, 3035 (1993)

[146]   Y. Sakai and M. Kudo, C. Nielsen, J. Vac. Sci. Technol. A **19**, 1139 (2001)

[147]   S. S. Kocha, M.W. Peterson, A. J. Nelson, Y. Rosenwaks, D. J. Arent, J. A. Turner, J. Phys. Chem. **99**, 744 (1995)

[148]   L. M. Smith, Thang B. Hoang, L.V. Titova, H. E. Jackson, J. M. Yarrison-Rice, J. L. Lensch, L. J. Lauhon, Y. Kim, H. J. Joyce and C. Jagadish., *Spatially-resolved Photoluminescence Imaging of CdS and GaAs/AlGaAs Nanowires*., 28th International Conference on the Physics of Semiconductors, ICPS 2006 - AIP Conf. Proc. **893,** 869 (2007).